ABSTRACT

INELASTIC PROTON SCATTERING
FROM ^{16}O AT BOMBARDING ENERGIES
FROM 24.6 TO 40.1 MeV

by Douglas Bayer

Proton inelastic scattering from ^{16}O has been measured at bombarding energies 24.6, 29.8, 33.5, 36.6, and 40.1 MeV. Angular distributions have been obtained from 10° to 100° for the doublet of states at 6.05 MeV (0^+) and 6.13 MeV (3^-) and the doublet of states at 6.92 MeV (2^+) and 7.12 MeV (1^-). The cross sections for exciting these four states have been analyzed using realistic nucleon-nucleon forces. The nuclear structure information necessary to construct form factors suitable for DWM calculations was obtained by fitting the available inelastic electron scattering data. The long range part of the Kallio-Kolltveit interaction provided an adequate description of the magnitude of the cross sections. The shapes of the calculated differential were insensitive to the interaction used, with all interactions adequate to describe observed shapes. A macroscopic collective model analysis of the data was also undertaken. The deformations were found to exhibit little

energy dependence from 29.8 to 40.1 MeV and were in good agreement with electromagnetic transition data.

INELASTIC PROTON SCATTERING FROM ^{16}O AT BOMBARDING ENERGIES FROM 24.6 TO 40.1 MeV

by

Douglas Leslie Bayer

A THESIS

Submitted to

Michigan State University

in partial fulfillment of the requirements

for the degree of

DOCTOR OF PHILOSOPHY

Department of Physics

1970

ACKNOWLEDGMENTS

I would like to thank Dr. W. Benenson for suggesting this experiment as a thesis topic and Dr. Edwin Kashy for his advise and assistance in developing the experimental techniques used in aquiring the data.

Ivan Proctor provided invaluable assistance both as a cyclotron operator and a consultant in solving the electronic and mechanical problems which arose during the long hours of the individual runs.

I would also like to express my appreciation to Dr. W. Kelly for his suggestions and guidance during the writing of this thesis.

I wish to express my appreciation to Harold Hilbert and N. Mercer for responding so gallantly to my repeated calls for assistance.

I acknowledge the financial support of the National Science Foundation and Michigan State University throughout my graduate work.

Finally, I wish to express my deepest appreciation to my wife, Maria. She has courageously endured my explanations of problems related to computer programming, data acquisition, and theoretical analysis, none of which she understood.

LIST

LIST

1.

2.

3.

4.

TABLE OF CONTENTS

	Page
LIST OF TABLES	v
LIST OF FIGURES	vi
1. INTRODUCTION	1
2. EXPERIMENTAL PROCEDURE	4
2.1 Cyclotron and Beam Transport	4
2.2 Spectrograph	6
2.3 Detectors	7
2.4 Monitor	12
2.5 Targets	12
2.6 Setup Procedure	15
2.7 Electronics and Particle Identification	17
2.8 Data Reduction	24
2.9 Error Analysis	25
3. EXPERIMENTAL RESULTS	28
3.1 The 6.05 MeV State	28
3.2 The 6.13 MeV State	31
3.3 The 6.92 MeV State	34
3.4 The 7.12 MeV State	37
4. NUCLEAR THEORY	40
4.1 DWBA Formalism	41
4.2 Form Factors	41
4.3 Collective Model Form Factors	43
4.4 Microscopic Form Factors	45
4.5 Optical Parameters	47

Page

5. COMPARISON OF DATA TO THEORY 52

5.1 Collective Model 52

5.2 Microscopic Model 52

5.3 Comparison of Microscopic Fits to the Data 59

5.4 The 6.13 MeV State 64

5.5 The 6.92 MeV State 68

5.6 The 7.12 MeV State 68

6. SUMMARY OF RESULTS AND CONCLUSIONS 78

6.1 Results 78

6.2 Conclusions 79

APPENDIX A 80

APPENDIX B 91

LIST OF REFERENCES 97

2.1

4.1

5.1

5.2

LIST OF TABLES

		Page
2.1	Summary of Errors	27
4.1	Optical Parameters	50
5.1	Deformation Parameters β_L Extracted from Collective Model Fits at Five Bombarding Energies	56
5.2	Values of V_{00} in MeV Obtained from the Microscopic Calculations using the Yukawa Interaction	72

2.1

2.2

2.3

2.4

2.5

2.6

2.7

2.8

2.9

2.10

3.1

3.2

3.3

3.4

3.5

3.6

LIST OF FIGURES

		Page
2.1	Experimental Area of the M.S.U. Cyclotron Laboratory	5
2.2	The Wedge Increases the Separation of Particles from D_1 at the Plate Holder to D_2 at Detector	9
2.3	A Typical Position Spectrum for the .3 mm Thick Detector with a 15° Wedge	10
2.4	A Typical Position Spectrum from the .12 mm Thick Detector Without a Wedge	11
2.5	A Typical Monitor Spectrum from the 5 mm Silicon Surface Barrier Detector	13
2.6	A Cross Section Drawing of Rotating Target Holder (Ma 68)	14
2.7	Counter Efficiency Versus Plate Height	16
2.8	Block Diagram of Electronics When Routing Was Used	19
2.9	Flow Chart of SETUP Mode Interrupt Routing	22
2.10	Flow Chart of RUN Mode Interrupt Routing	23
3.1	Center of Mass Cross Section Plotted as a Function of Scattering Angle for the 6.05 MeV State	29
3.2	Center of Mass Cross Section Plotted as a Function of $Q = \lvert\vec{k}_i - \vec{k}_f\rvert$ for the 6.05 MeV State	30
3.3	Center of Mass Cross Section Plotted as a Function of Scattering Angle for the 6.13 MeV State	32
3.4	Center of Mass Cross Section Plotted as a Function of $Q = \lvert\vec{k}_i - \vec{k}_f\rvert$ for the 6.13 MeV State	33
3.5	Center of Mass Cross Section Plotted as a Function of Scattering Angle for the 6.92 MeV State	35
3.6	Center of Mass Cross Section Plotted as a Function of $Q = \lvert\vec{k}_i - \vec{k}_f\rvert$ for the 6.92 MeV State	36

		Page
3.7	Center of Mass Cross Section Plotted as a Function of Scattering Angle for the 7.12 MeV State	38
3.8	Center of Mass Cross Section Plotted as a Function of $Q = \|\vec{k}_i - \vec{k}_f\|$ for the 7.12 MeV State	39
5.1	DWM Calculations for the 6.13 MeV State	53
5.2	DWM Calculations for the 6.12 MeV State	54
5.3	DWM Calculations for the 7.12 MeV State	55
5.4	Electron Scattering Form Factor Using the Transition Density Extracted from the Least Squares Fit	58
5.5	Electron Scattering Form Factor Using the Transition Density Extracted from the Least Squares Fit	60
5.6	DWM Microscopic Calculations for the 6.05 MeV State Using a 1f Range Yukawa Interaction	61
5.7	DWM Microscopic Calculations for the 6.05 MeV State Using the Long Range Part of the K-K Interaction	62
5.8	The Form Factor for the 6.05 MeV State Without Including Exchange	63
5.9	DWM Calculations for the 6.13 MeV State Using a 1f Yukawa Interaction	65
5.10	DWM Calculations for the 6.13 MeV State Using the Long Range Part of the K-K Interaction	66
5.11	DWM Calculations for the 6.13 MeV State Using the K-B Interaction	67
5.12	Electron Scattering Form Factor Using the Transition Density Extracted from the Least Squares Fit	69
5.13	DWM Calculations for the 6.92 MeV State Using a 1f Range Yukawa Interaction	70
5.14	DWM Calculations for the 6.92 MeV State Using the Long Range Part of the K-K Interaction	71

5.15

5.16

5.17

5.18

		Page
5.15	Electron Scattering Form Factor Calculated from the Transition Density Extracted from the Least Squares Fit	74
5.16	DWM Calculations for the 7.12 MeV State Using a 1f Range Yukawa Interaction	75
5.17	DWM Calculations for the 7.12 MeV State Using the Long Range Part of the K-K Interaction	76
5.18	DWM Calculations for the 7.12 MeV State Using the Long Range Part of the K-K Interaction	77

1. INTRODUCTION

This experiment investigates the first four excited states in ^{16}O via the $^{16}O(p,p')^{16}O^*$ reaction. Differential cross sections for $J^\pi = 0^+$ state at 6.05 MeV, $J^\pi = 3^-$ state at 6.13 MeV, $J^\pi = 2^+$ state at 6.92 MeV, and $J^\pi = 1^-$ state at 7.12 MeV, were measured at five bombarding energies from 24.6 to 40.1 MeV.

The measurements were made using the M.S.U. double focusing split-pole magnetic spectrograph. The spectrograph has the facility to compensate for the effects of kinematic broadening. This permits measurements subtending angles as large as 2° in the reaction plane without sacrificing energy resolution. Recent developments in the fabrication of silicon surface barrier position sensitive detectors, which provide position resolution of up to 0.5 mm and permit count rates in excess of 50,000 counts per second, enabled the strongly excited 3^- state and the weakly excited 0^+ state to be taken simultaneously using an on line computer.

Theoretical interest, particularly in the 0^+ state at 6.05 MeV, provided the motivation for this experiment. In order to construct an even parity state using a harmonic oscillator potential, one has to excite at least two quanta of energy. Calculations using such excitations produce levels which overestimate the position of the 0^+ by more than 20 MeV.

In

Carter

at 10.3

system.

band st

at 6.92

using t

to repr

not low

Br

energy

state f

to cons

electro

Re

provide

0^+, 3^-,

along w

nucleus

form fa

in an

Th

Gillet

by pro

shell.

wave f

electr

Inelastic alpha scattering from ^{12}C performed by Carter et al (Ca 64) at 10 to 19 MeV identified the 4^+ at 10.36 MeV and the 6^+ at 16.2 MeV in the compound ^{16}O system. He identified these states as part of a rotational band starting with the 0^+ at 6.05 MeV and including the 2^+ at 6.92 MeV. Brink and Nash (Na 63) and Borysowicz (Bo 64), using the SU_3 symmetry scheme of Elliott (El 58), were able to reproduce the level separation within the band, but could not lower the 0^+ state relative to the ground state.

Brown and Green (Br 66), noting that the configuration energy of a 4p - 4h state was lower than that of a 2p - 2h state for a deformed nucleus, used the SU_3 symmetry group to construct wave functions which were in agreement with electromagnetic transition rate data.

Recent $^{16}O(e,e')^{16}O^*$ data by Bergstrom et al (Be 70) provide a direct measure of the nuclear structure of the 0^+, 3^-, 2^+ and 1^- states. This structure information, along with the appropriate multipole of the nucleon-nucleus interaction, define the distorted wave method (DWM) form factor. This provides a test of the nuclear structure in an independent experiment.

The negative parity states have been investigated by Gillet and Vinh Mau (Gi 64) who constructed wave functions by promoting one particle from the $1p_{1/2}$ orbit to the sd shell. In this work the cross sections predicted by these wave functions were compared with those derived from the electron scattering data.

T

nuclea

this w

invest

of the

ticula

A

The de

troma

sectio

The d

contr

the d

The nucleon-nucleus force, being independent of the nuclear structure, can be varied in the calculations. In this work a variety of effective interactions have been investigated. These investigations indicate that the shape of the calculated differential cross section is not particularly sensitive to the details of the interaction.

A collective model analysis was also undertaken. The deformations were found to be in agreement with electromagnetic transition rate data.

The energy dependence of the differential cross sections was found to be monotonic from 29.8 to 40.1 MeV. The data at 24.6 showed indications of strong compound contributions. The agreement between the calculations and the data, in general, improved with energy.

In

inelast

of well

unambig

and an

sources

In

in meas

error a

2.1 Cy

Th

Univers

with 1

Magneti

schemat

slits S

beam 45

energy

probes

magnet

graph p

2. EXPERIMENTAL PROCEDURES

In order to measure differential cross sections for inelastic proton scattering, one must have a proton beam of well defined energy, a detection system which permits unambiguous identification of the quantities being measured and an analysis procedure which accounts for all known sources of systematic and random error.

In this chapter the apparatus and procedures involved in measuring the cross sections are discussed and the error analysis is presented.

2.1 Cyclotron and Beam Transport

The proton beam was accelerated in the Michigan State University sector focused cyclotron (Bl 66) and extracted with 100% efficiency via an electrostatic deflector and magnetic channel. The transport system (Ma 67), illustrated schematically in Figure 2.1, focused the extracted beam on slits S1 and S3. Bending magnets M3 and M4 each bend the beam 45° providing energy dispersion of .03% mm. The beam energy was determined from nuclear magnetic resonance probes placed in the central fields of M3 and M4. Bending magnet M5 was used to deflect the beam 45° into the spectrograph beam line.

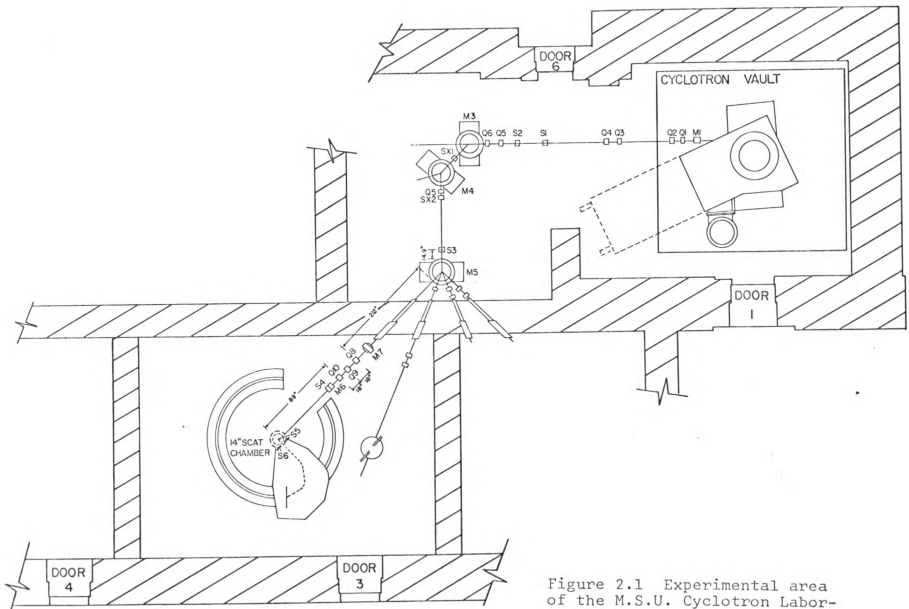

Figure 2.1 Experimental area of the M.S.U. Cyclotron Laboratory

2.2 Spectrograph

All data were taken using the M.S.U. split pole, double focusing magnetic spectrograph. A .368" x .372" slit, subtending 1.202 millisterradians, was used to define the solid angle. The spectrograph was chosen because it provided a way to eliminate the effects of kinematic broadening, allowing a large solid angle without loss of resolution. Furthermore, the problems of pile-up and dead time due to the large forward angle cross section of the elastic peak were circumvented by keeping the elastic peak off the detector.

The kinematic variation of particle energy with angle moves the position of the focal plane in closer to the target. Particles scattered into the high angle side of the entrance slit are less energetic, and thus less rigid, than the axial ray, while particles scattered into the low angle side of the slit are more energetic and thus more rigid. These rays will cross somewhat more quickly after deflection in the spectrograph than will particles of the same energy following the same three defined trajectories. A linear approximation to the displacement of the focal plane presented by Enge (En 67), was computed by the program "SPECTKINE" (Tr 70) which computed the NMR frequency required to place the axial ray at a specified effective radius of curvature ρ as well as the displacement of the plate holder from the first order focal plane.

2.3 De

At

Nuclear

detecto

appropr

6.05 -

MeV do

dimensi

spectiv

tor was

separat

Th

the E s

particl

proport

positio

the XE

the eff

measure

mass re

tinguis

rigidit

Th

the lin

protons

resista

2.3 Detectors

At bombarding energies of 29.8 and 33.48 MeV, two Nuclear Triode Silicon surface barrier position sensitive detectors were placed on the spectrograph plate holder with appropriate separation to simultaneously observe the 6.05 - 6.13 MeV doublet on one counter and the 6.92 - 7.115 MeV doublet on the other. The two detectors were of dimensions 30 x 10 x .3 and 30 x 11 x .12 millimeters respectively. At 24.6, 36.6 and 40.07 MeV the second detector was unavailable requiring the states to be measured separately.

The position sensitive detectors provide two signals, the E signal, proportional to the energy deposited by the particles in passing through the counter and the XE signal, proportional to the product of the energy loss and the position. In order to get optimum position resolution, the XE signal is divided by the E signal, which eliminates the effects of straggling. The E signal also provides a measure of Z^2/M, where Z and M are the particles charge and mass respectively. This information can be used to distinguish between reaction products of the same magnetic rigidity.

The noise associated with the XE signal proved to be the limiting factor in position resolution of high energy protons. This noise is produced by a relatively small resistance of 16KΩ in parallel with the large capacitance of

the det

leads t

of a la

detecti

ciently

doublet

detecti

To incr

well as

wedge o

counter

increas

clinati

15° wed

is incr

or abo

MeV do

full w

40 Mev

The ef

Typic

in Fi

the detector. Attempts to decrease one of these components leads to an increase in the other, implying the necessity of a large XE signal. The amount of energy lost in the detector by 23 to 34 MeV protons did not provide a sufficiently large signal to enable us to resolve the 80 KeV doublet, even though the particles pass through the detector at 45°, making its effective thickness 425 microns. To increase the effective thickness of the detector as well as the effective dispersion of the spectrograph, a wedge of 15° was inserted between the plate holder and the counter. The effective detector thickness is thereby increased by $1/\cos(\phi + 45)$, where ϕ is the angle of inclination, which increases the energy loss by 50% for a 15° wedge. The effective dispersion of the spectrograph is increased by a factor of

$$\frac{1}{1 - \tan\phi}$$

or about 34% for a 15° wedge. With the wedge, the 6.05 -6.13 MeV doublet was separated at all energies to better than full width at half maximum (FWHM) of the 6.05 MeV peak at 40 MeV and was completely separated at all lower energies. The effects of the wedge are illustrated in Figure 2.2. Typical position spectra for the two counters are illustrated in Figures 2.3 and 2.4.

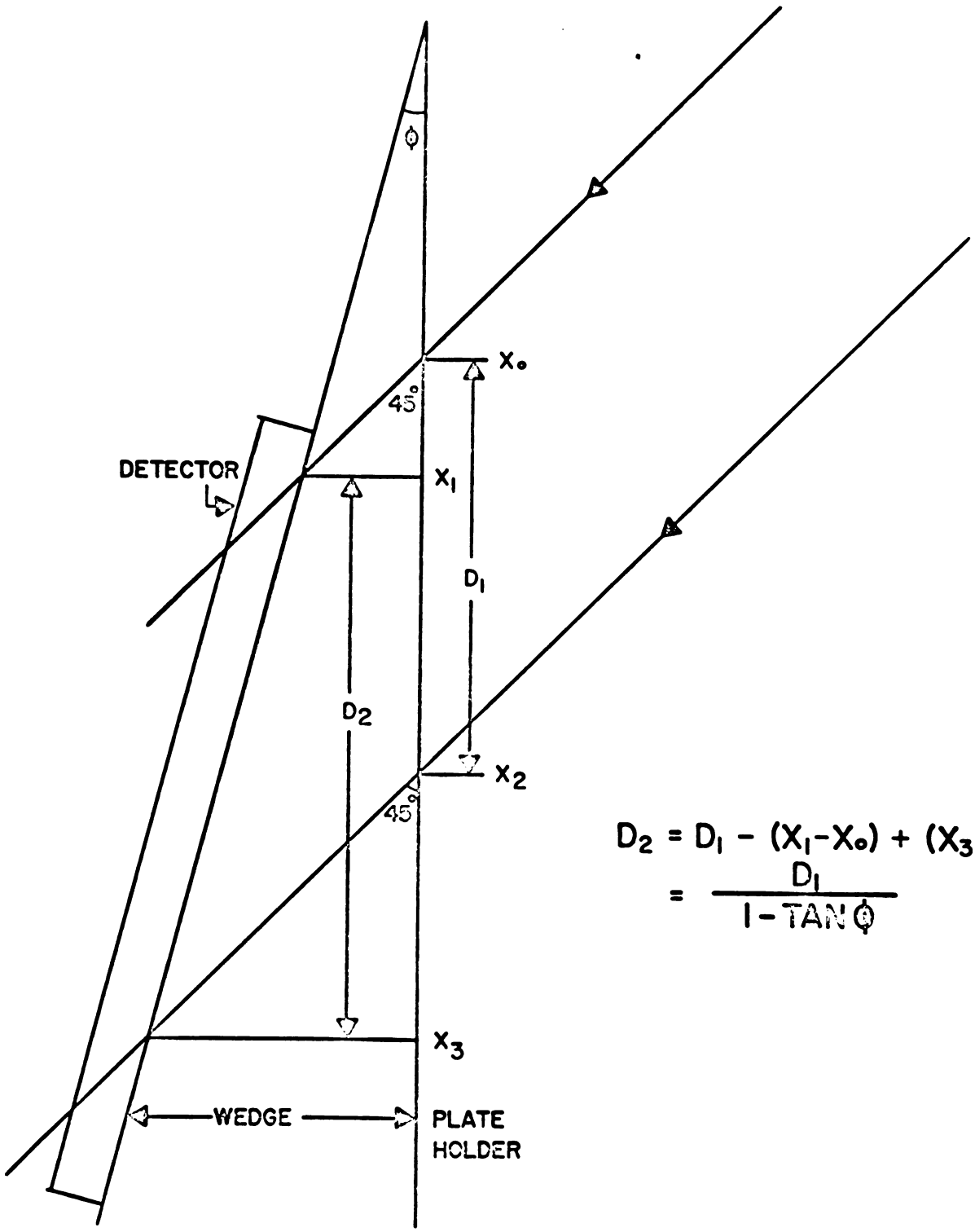

$$D_2 = D_1 - (X_1 - X_0) + (X_3 - X_2)$$
$$= \frac{D_1}{1 - \tan\Phi}$$

Figure 2.2 The wedge increases the separation of particles from D_1 at the plate holder to D_2 at detector.

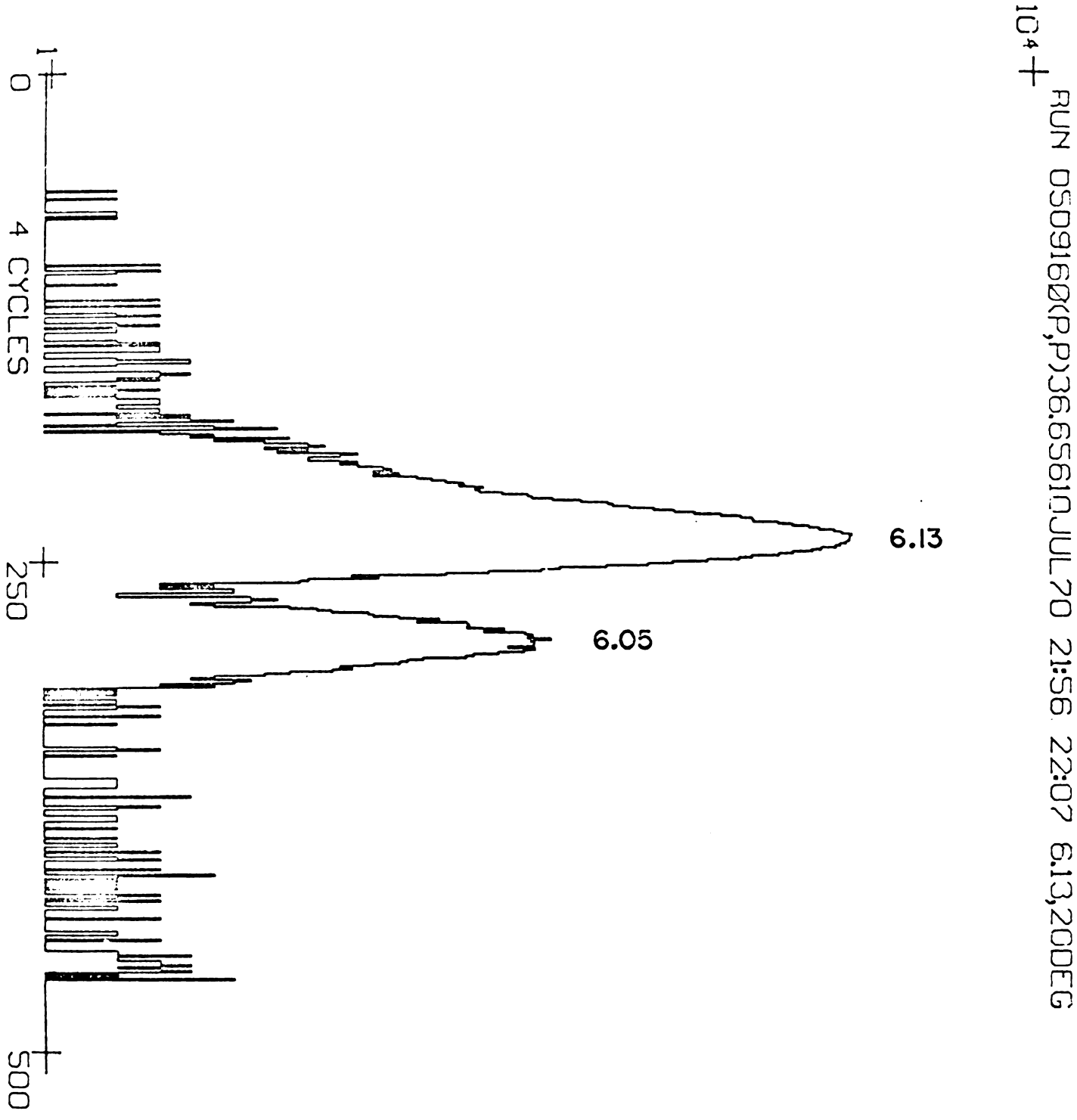

Figure 2.3 A typical position spectrum for the .3 mm thick detector with a 15° wedge.

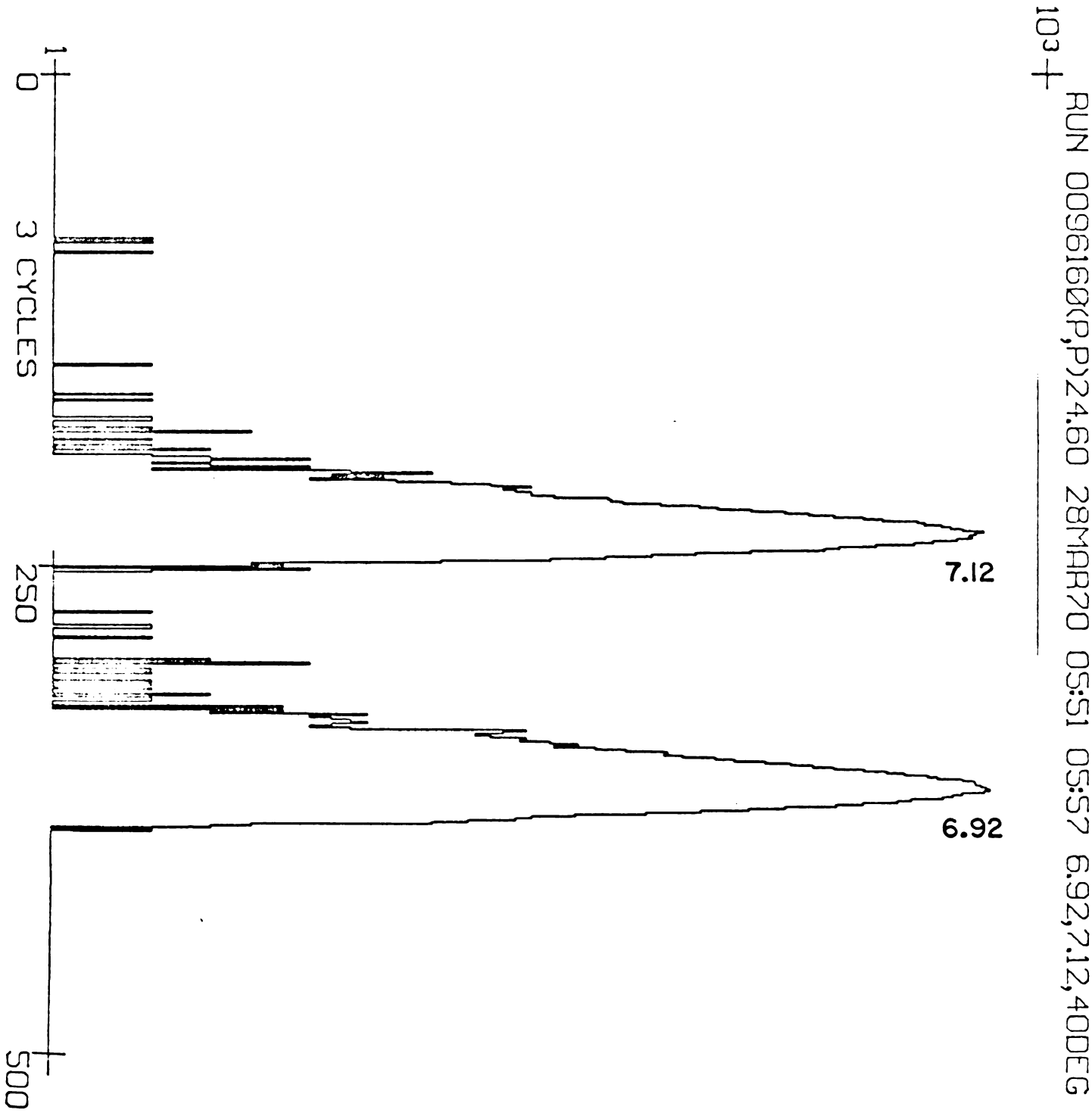

Figure 2.4 A typical position spectrum from the .12 mm thick detector without a wedge.

2.4 Mo

A
monitor
at 90°
less th
detecto
copper
proton
states
scintil
multipl
ground
monitor

2.5 Ta

C
approx
whose
target
relati
heavy
spectr
calibr
proble
beam
posit

2.4 Monitor

A 5 mm silicon surface barrier detector was used to monitor the oxygen elastic peak. The detector was placed at 90° at 29.8 and 33.48 MeV where the proton range was less than the detector thickness. At 36.6 and 40 MeV the detector was placed at 150° and an absorber of 10 mil copper was placed in front of the collimator to lower the proton energy. In all cases the oxygen and carbon ground states were completely resolved. At 24.6 MeV a Na I(Tl) scintillation crystal mounted on the face of a photomultiplier was used. In this case the carbon and oxygen ground states were unresolved. In Figure 2.5 a typical monitor spectrum is shown.

2.5 Targets

Commercially available .25 mil Mylar containing approximately 300 $\mu g/cm^2$ of oxygen was used. Mylar, whose composition is $C_{10}(H_2O)_4$ provides an excellent target to investigate the low lying states in ^{16}O. The relatively high oxygen content along with the absence of heavy elements provided an almost background-free energy spectrum at all angles. The hydrogen peak serves as calibration point for measuring the angle. The only problem encountered with Mylar was that the heat of the beam melted the target. This effect was minimized by positioning the center of the target 3/8" above the beam

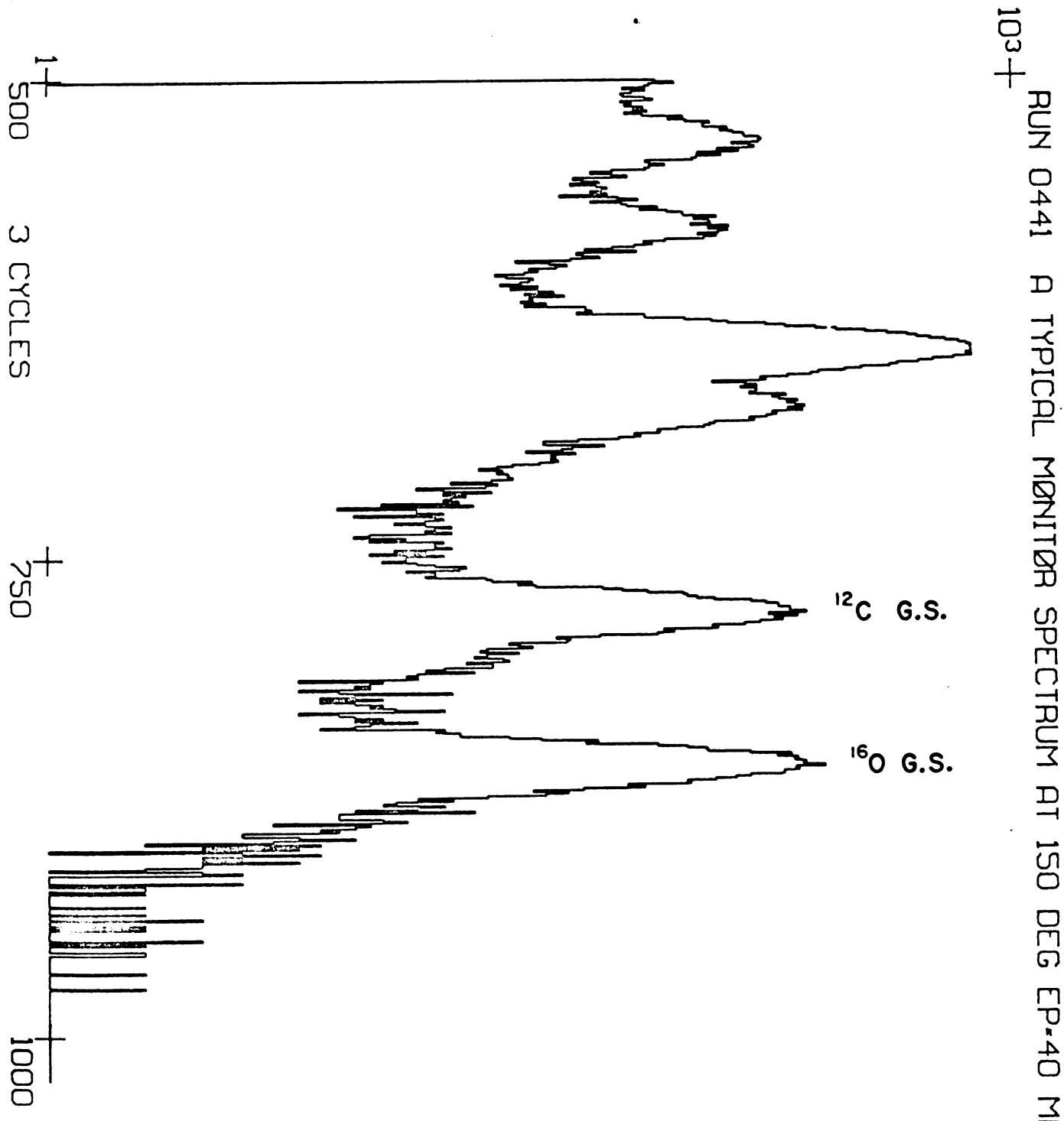

Figure 2.5 A typical monitor spectrum from the 5 mm silicon surface barrier detector

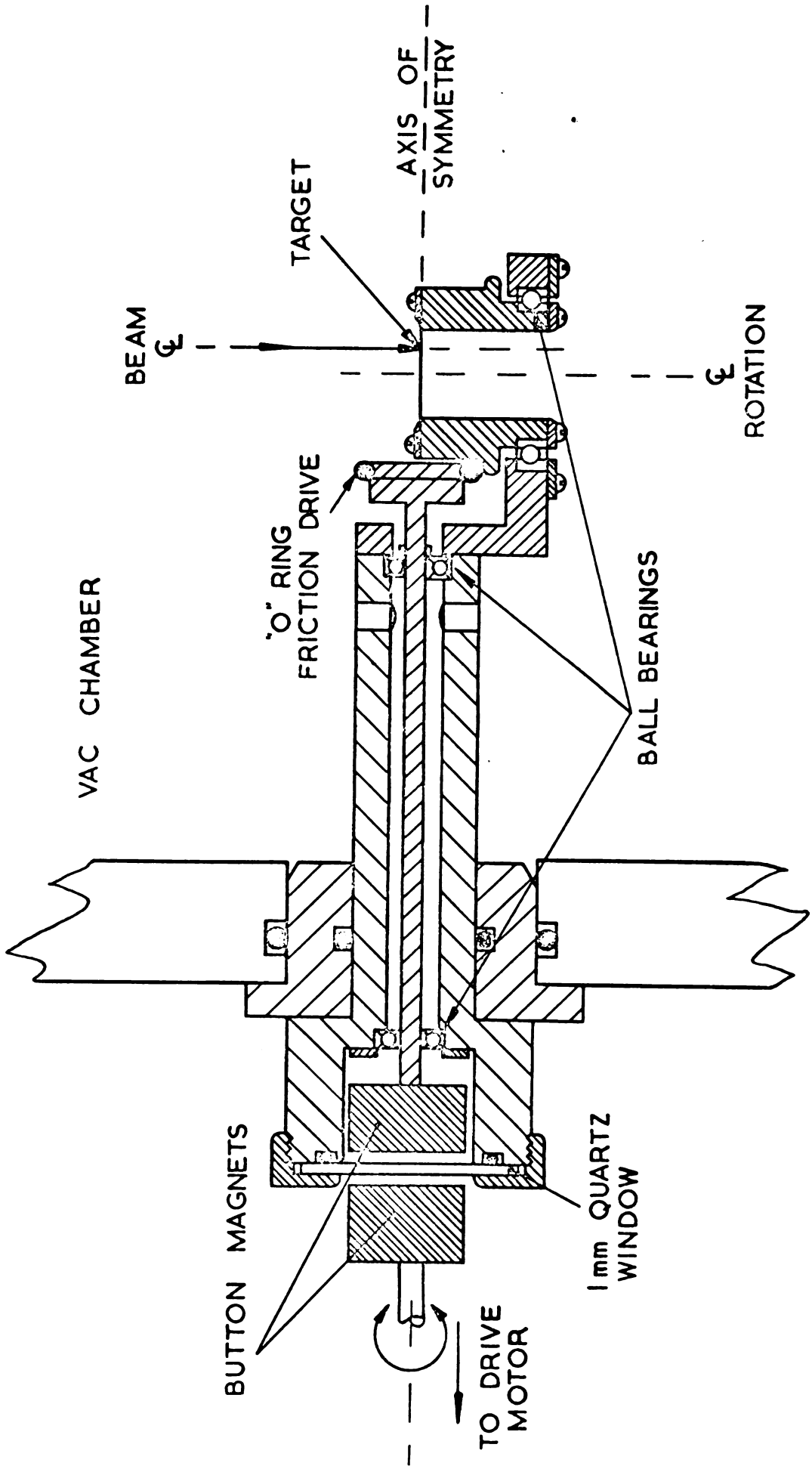

Figure 2.6 A cross section drawing of rotating target holder (Ma 68).

and rotating it about its center at about 600 rpm. An electric motor magnetically coupled, through a vacuum seal, to a shaft which extended down to the target kept the target rotating at a constant speed. The frequency of rotation could be varied from about 50 to 1600 rpm with a Variac. This method allowed the target to withstand a constant beam current of 120 nanoamps for twelve hours with only 10 to 20 percent decrease in the target thickness.

2.6 Setup Procedure

The cyclotron beam was threaded through the beam transport system, energy analyzed and deflected into the spectrograph beam line. The beam was focused to a small point and positioned over the center of the scattering chamber. A television camera focused on a quartz scintillator allowed direct observation of the position and size of the beam spot. A piece of wire, mounted vertically on the scintillator defined the center of the scattering chamber.

The target holder was removed, the monitor counter and target rotator mounted, and the spectrograph set to 20°. The amplifier gain on the monitor counter was adjusted and the single channel analyzer window set. Inelastic protons from the 6.13 MeV state of ^{16}O were swept across the position sensitive counter to determine the counter efficiency and resolution as a function of position

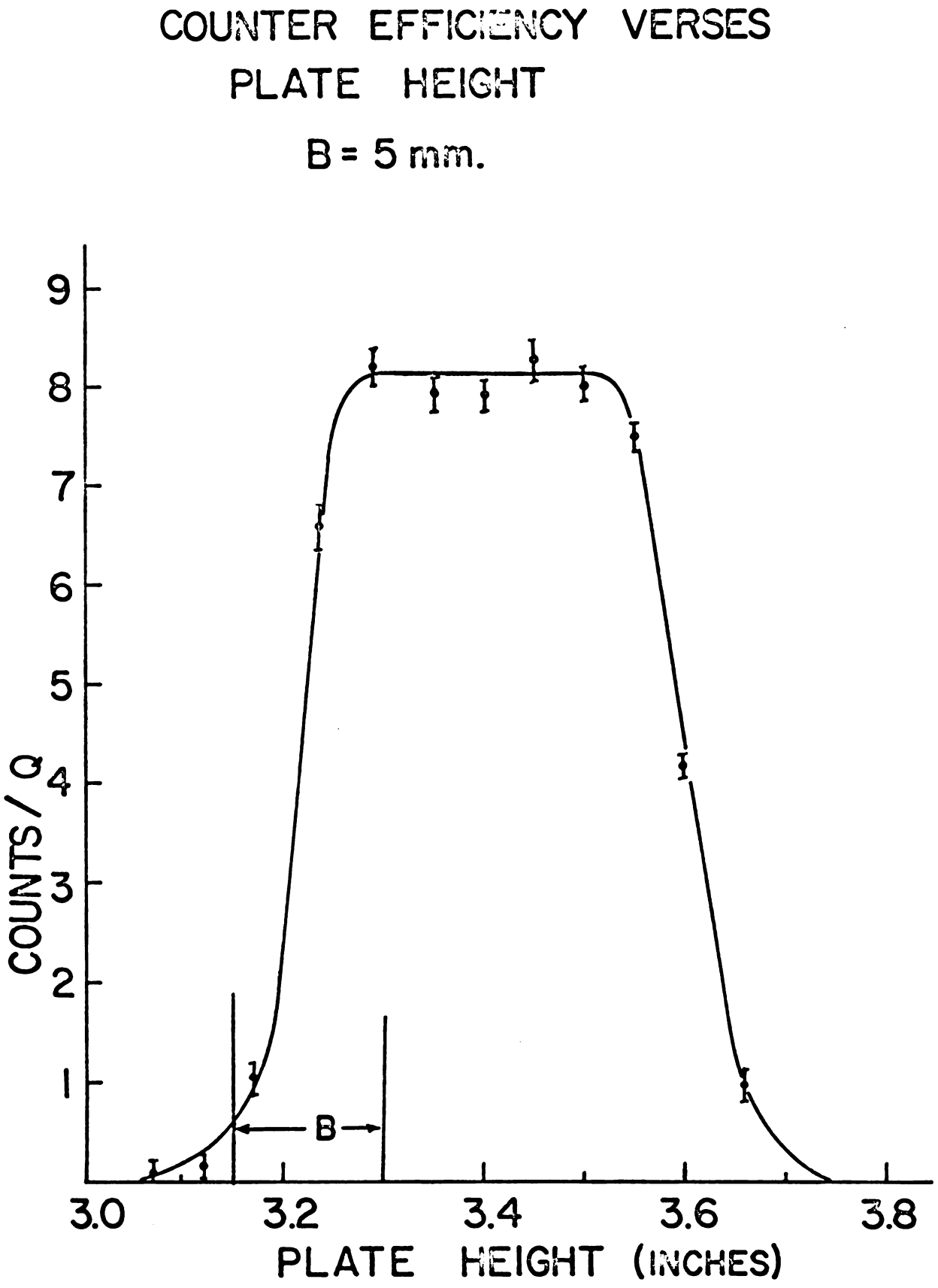

Figure 2.7 B is height of beam spot at the detector.

on the counter. The magnetic field at which the best resolution was obtained was used to find the effective radius of curvature ρ. The plate height was then varied to determine the vertical detector efficiency and the image size of the beam spot at the detector. The beam spot was typically four millimeters high at the counter. Figure 2.7 shows a typical vertical efficiency curve.

2.7 Electronics and Particle Identification

The XE and E signals were amplified by separate ORTEC 109A preamplifiers which were placed on top of the spectrograph. The amplified signals were transmitted out to the data room where the XE signal was input to a Tennelec TC 200 amplifier which had 0.8 μsec differentiation and integration time constants. The E signal was fed into an ORTEC model 451 spectroscopy amplifier with all shaping times set at 0.5 μsec. The resulting prompt bipolar E pulse was then input to a single channel analyzer which was used strictly as a lower level discriminator while the delayed monopolar pulse was input to an ORTEC 442 linear gate stretcher. The bipolar output of the TC 200 was delayed and fed into a second ORTEC 442 linear gate stretcher. Both signals were enabled by the logic pulse from the single channel analyzer. The output signals of the linear gates were rectangular in shape, one μsec wide and were adjusted so that their leading edges were within 100 nanoseconds of

each other. These pulses were then input to two Northern Scientific 13-bit, 50 megacycle analog to digital converters run in coincidence mode. When two detectors were used, separate amplifier systems were used for each detector. The signals from the linear gates were multiplexed together with two summing amplifiers. The logic pulses from the two single channel analyzers were fed into two of the seven inputs on the routine box associated with the ADC's. The routing bits were ORed into the upper three bits of the sixteen bit general purpose interface register. The thirteen bits from the ADC conversion were put into the lower bit positions. Block diagrams of the electronic configuration are shown in Figure 2.8.

The monitor signals were amplified by an ORTEC 109A preamplifier and an ORTEC 451 spectroscopy amplifier. The bipolar pulse was fed into a single channel analyzer which was set to output a pulse only for the oxygen elastic peak. The output of the single channel analyzer was fed into a scalar and a live-time clock input on the ADC's. The ungated monopolar pulses were fed into one of the four 1024 channel subgroups of the Nuclear Data ND-160 4096 multi-channel analyzer.

The data acquisition task TOOTSIE, operating under the JANUS (Ko 68) time sharing supervisor, was used to process the data as it was presented to the Sigma 7 computer. TOOTSIE was designed to process all types of two and three

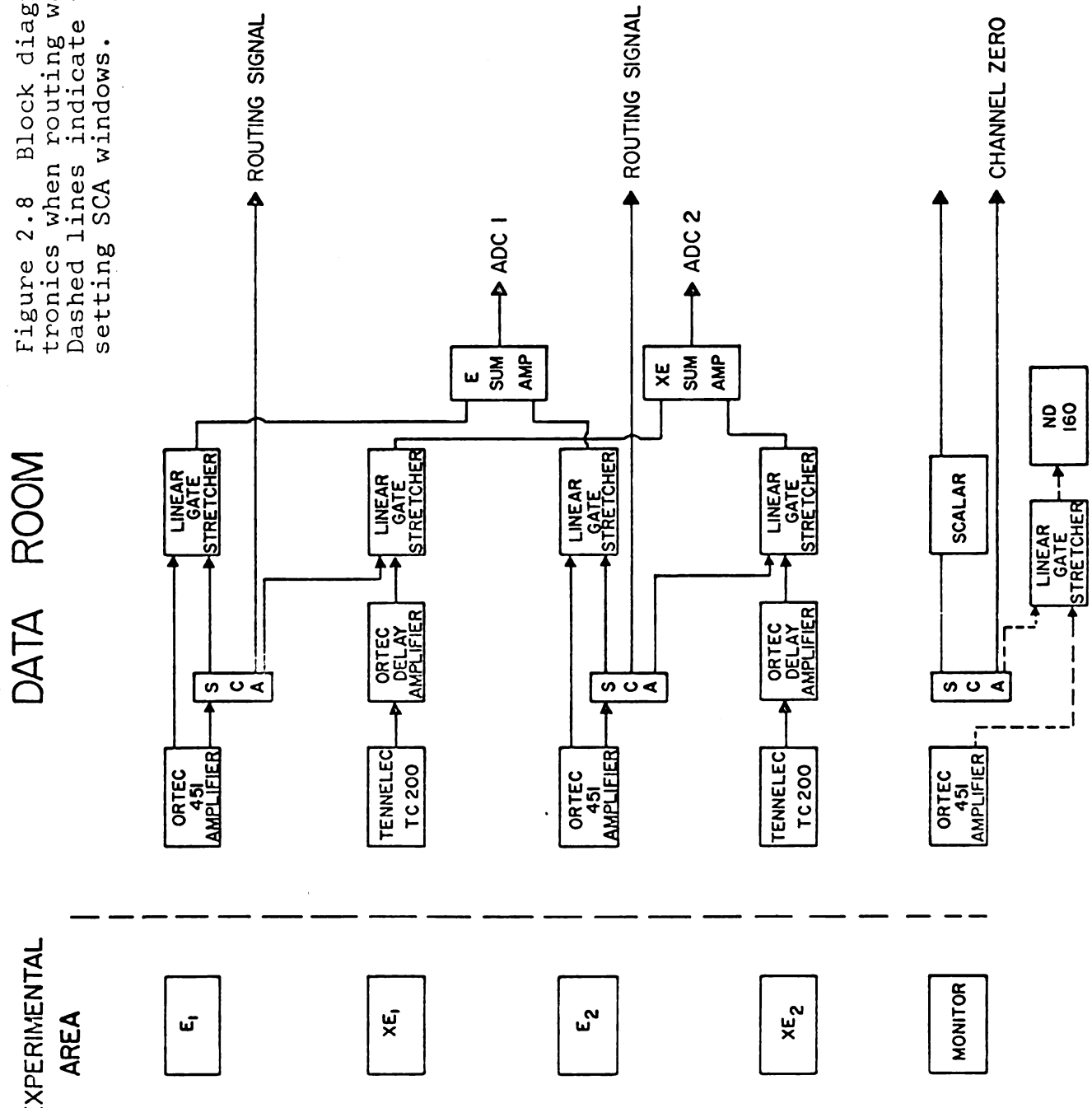

Figure 2.8 Block diagram of electronics when routing was used. Dashed lines indicate use in setting SCA windows.

parameter data requiring some form of event identification taken by the users of the Michigan State University cyclotron. A variety of options provide for various calculations to be performed on the data before being stored. Only the XE/E routine, which was used in this project, will be described here. A complete list of the available data acquisition routines is given in Appendix B.

The program operates in two modes, SETUP and RUN. In SETUP mode the E signal is stored as a function of the quotient XE/E in a 64 x 64, 64 x 256, or 128 x 128 two dimensional array. The data are displayed on a TEKTRONIX 611 storage scope, appearing as a series of bands across the screen. Polynomial fits, generated by accepting a series of points with a movable cross, define the lower and upper bound for each band.

When routing is used, bands for each detector are set independently. A total of fourteen bands can be generated.

Service routines provide the facility to punch, print or store the contents of the 2D analyzer on a permanent disk file. Analysis routines provide a display of the mass spectrum by summing channels horizontally, as well as low resolution position spectra by summing channels vertically between the bands. A three dimensional isometric display provides an overview of the data.

When all bands have been set, the program is switched into RUN mode via a teletype command. Tables of 256 points per fit are generated and stored for each detector. Events are then checked against the tables corresponding to the detector indicated by the routing bits and the appropriate channel of the spectrum in which the match was found is incremented. The spectra ranged from 512 to 8192 channels. Figure 2.9 is a flow chart of the SETUP mode routine and Figure 2.10 is a flow chart of the RUN mode routine.

In order to assess the overall quality of the data, a routine computes the centroid, area, full width at half maximum and ratio of peak area to monitor counter for up to fifty peaks in two spectra which can be displayed simultaneously on the storage scope.

With the resolution of a 128 x 128 multichannel analyzer, irregularities in the charge collection efficiency of the counter could be seen as dips in the energy bands. Particles falling on these dips would produce distorted peak shapes.

The use of digital gates provides a great deal of flexibility in identification logic. A procedure often used to increase the peak to valley ratio is to embed one band within another. The inner band is very close to the data while the outer band is set to assure that no counts are lost due to electronic gain shifts or changes in pulse height as a function of scattering angle.

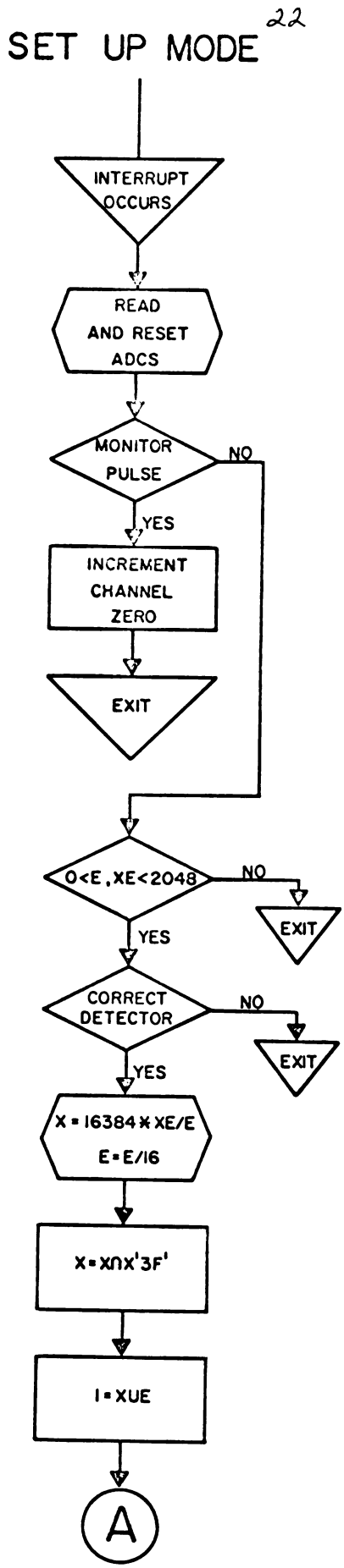

Figure 2.9 Flow chart of SETUP mode interrupt routine.

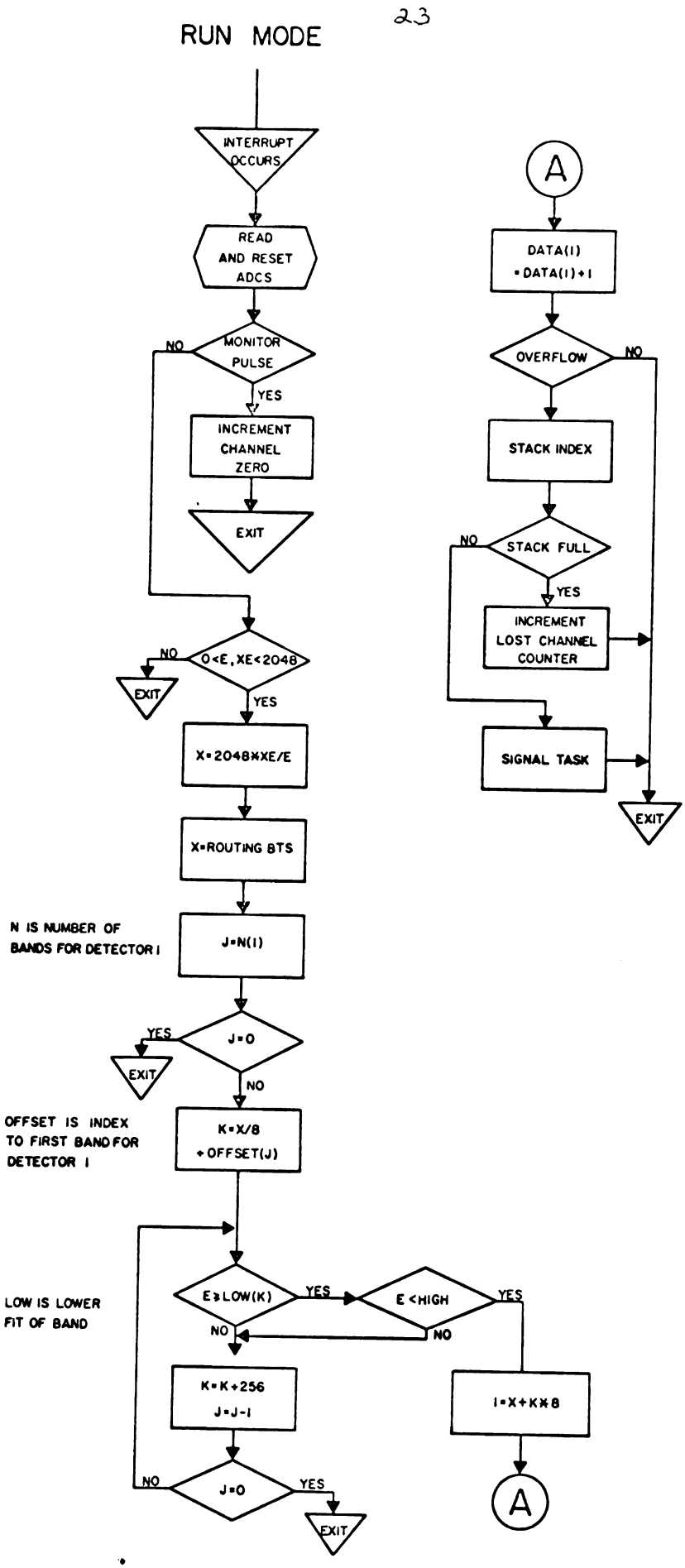

Figure 2.10 Flow chart of RUN mode interrupt routine.

The computer, when used as a particle identifier, permits simultaneous acquisition of more than one reaction fragment from more than one detector with a minimum of electronics.

2.8 Data Reduction

At all beam energies except 40 MeV, the 6.05 and 6.13 MeV states were completely resolved. The peak areas and centroids were extracted with the data reduction task MOD7 (Ba 70), operating under the JANUS time-sharing supervisor. The data are displayed on a TEKTRONIX 611 storage scope. The user communicates with the code through 32 sense switches.

To ascertain the background under a peak, regions on both sides of the peak are selected with a movable cross and fit with a polynomial of up to ninth order. The left and right peak limits are selected with the cross and the area is computed by subtracting the sum of the background from the sum of the data points.

At 40 MeV, the peaks were resolved to FWHM of the comparatively weak 6.05 MeV state, leaving approximately 12% of its area unresolved from the 6.13 MeV peak. To extract this area two Gaussian peaks with exponential tails were fit to the data determining the relative strength of the two peaks in the overlapping region. Typical X^2/N values were between 1.1 and 1.4.

The cross sections were calculated relative to the monitor with the formula:

$$\sigma_{exp} = N\ (C_p - B_p)\ /\ (C_m - B_m)$$

C_p is the total counts in the inelastic peak, C_m is the total counts in the oxygen elastic peak of the monitor counter spectrum, B_p and B_m are the respective backgrounds and N is a normalization obtained by requiring the oxygen elastic cross section measured in the spectrograph agree with those of Snelgrove (Sn 68) and Cameron (Ca 67).

2.9 Error Analysis

Two main factors contribute to errors in the measured cross sections:

1) Statistical fluctuations
2) Normalization errors

To estimate the error due to statistical fluctuations, a Gaussian distribution was used to approximate the Poisson distribution. The standard deviation in the counts in a peak for which a Gaussian distribution is valid is given by $\sqrt{c}$, where c is the total number of counts in the peak including background. The monitor counter and inelastic scattering statistical errors were added in quadrature since they are independent errors.

As a result of the normalization procedure, three errors have to be considered. Since the normalization was determined by forcing the elastic cross section to agree with that measured by Snelgrove and Cameron at 60°, any error assignment must include the experimental errors which they assigned. This error was of the order of one to three percent. The error in the scattering angle at which the normalization was extracted was estimated to be 0.1°. To estimate the resulting normalization error, the derivative of the cross section at this angle was evaluated indicating an error of 0.5%. The large solid angle subtended by the spectrograph weights the scattering angle by the cross section. This displacement was of the order of 0.01°. These three errors were added in quadrature.

An additional error was introduced at several energies due to a bombarding energy mismatch. Linear interpolation of the cross section was used to correct for this. The energy never deviated by more than 600 KeV from that of Cameron (Ca 67) requiring a correction of 8% to the cross section. The error in this procedure was estimated to be 0.5%. This error was added linearly to the other errors. Table 2.1 summarizes the error contributions for a typical point on the angular distribution of the 6.13 MeV state at 36.65 MeV.

Table 2.1

A)	Statistical Error		
	1) Inelastic peak	0.5%	
	2) Monitor peak	1.1%	
B)	Normalization Error		
	1) Cameron Experimental	0.6%	
	2) Angle error at 60°	0.5%	
C)	Added in Quadrature		1.7%
D)	Interpolation Error		0.5%
E)	Total Error Added Linearly		2.2%

3. EXPERIMENTAL RESULTS

The angular distributions for the first four excited states in ^{16}O were measured at five energies from 24.6 to 40.06 MeV. Experimental errors were estimated to be less than 5% at bombarding energies less than 40 MeV. At 40 MeV, the errors were somewhat larger due to the previously discussed resolution problems and somewhat larger normalization errors. Figures 3.1 - 3.8 show these angular distributions.

3.1 The 6.05 MeV State

The angular distribution for the $J^{\pi} = 0^{+}$ state at 6.052 MeV of excitation shown in Figure 3.1 is strongly forward peaked at energies above 24.6 MeV. A second maximum at 35° grows monotonically with energy. The minimum at 60° becomes less distinct as does the third maximum at 80°.

The most striking feature of the angular distributions is the rather drastic change in shape between 24.6 and 29.8 MeV. The shape measured at 24.6 MeV is essentially the same as that of Crawley (Cr 65) at 17.5 MeV, indicating that the shape does not change appreciably at lower energies.

In order to view the data from a different perspective, the center of mass cross sections are plotted as functions of momentum transferred to the nucleus in Figure 3.2. By displaying the data in this way, the dependence of the shape of the differential cross section on the energy of the incident

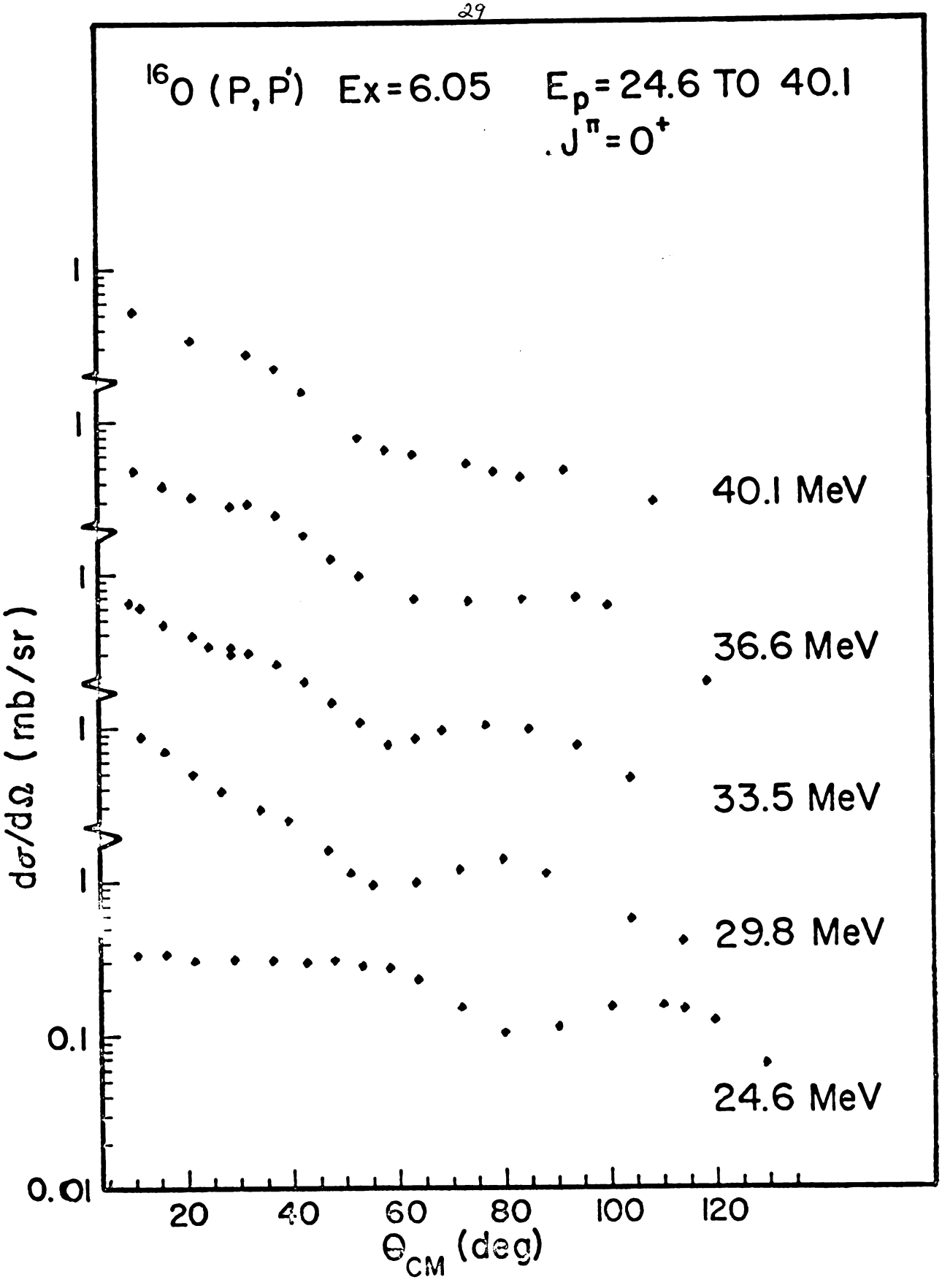

Figure 3.1 Center of mass cross section plotted as a function of scattering angle.

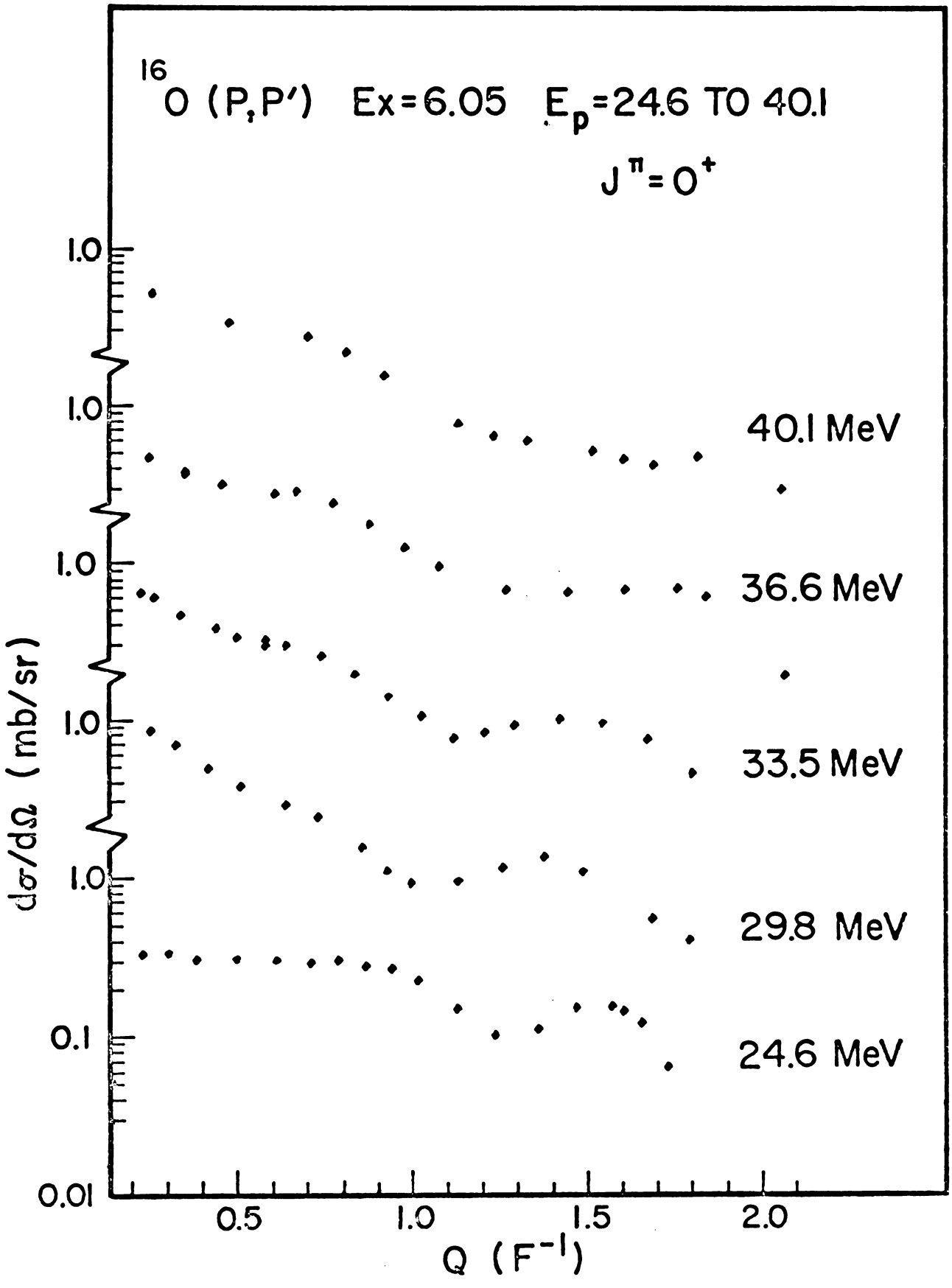

Figure 3.2 Center of mass cross section plotted as a function of $Q = |\vec{k}_i - \vec{k}_f|$

particle is removed. This allows one to qualitatively investigate the "directness" of the interaction. On the basis of a simple plane wave theory of direct reactions (Bu 57), the cross sections are functions of q. If this picture is valid, one would expect the shape to be nearly the same at all bombarding energies. Since this is the case for the bombarding energies above 24.6 MeV, one is confident that the theory applied there is valid. However, the differential cross section measured at 24.6 MeV is in serious disagreement with the others. One possible explanation put forward by Cameron (Ca 67) is that the reaction at this energy proceeds through states in ^{17}F, and thus is a compound nuclear phenomenon. A second explanation (Au 70) is that the 0^+ state is being excited through an intermediate state which is strongly excited by inelastic scattering (presumably the 6.13 MeV state). If either of these processes have strong contributions to the cross section, the analysis within the framework of a direct reaction theory is subject to question.

3.2 The 6.13 MeV State

The angular distribution for the $J^\pi = 3^-$ state is plotted as a function of center of mass scattering angle in Figure 3.3 and as a function of momentum transfer in Figure 3.4. These angular distributions vary smoothly with angle and show little structure. The maximum of the angular distribution occurs at approximately 45° in the center of mass. The magnitude of the angular distribution decreases monotonically

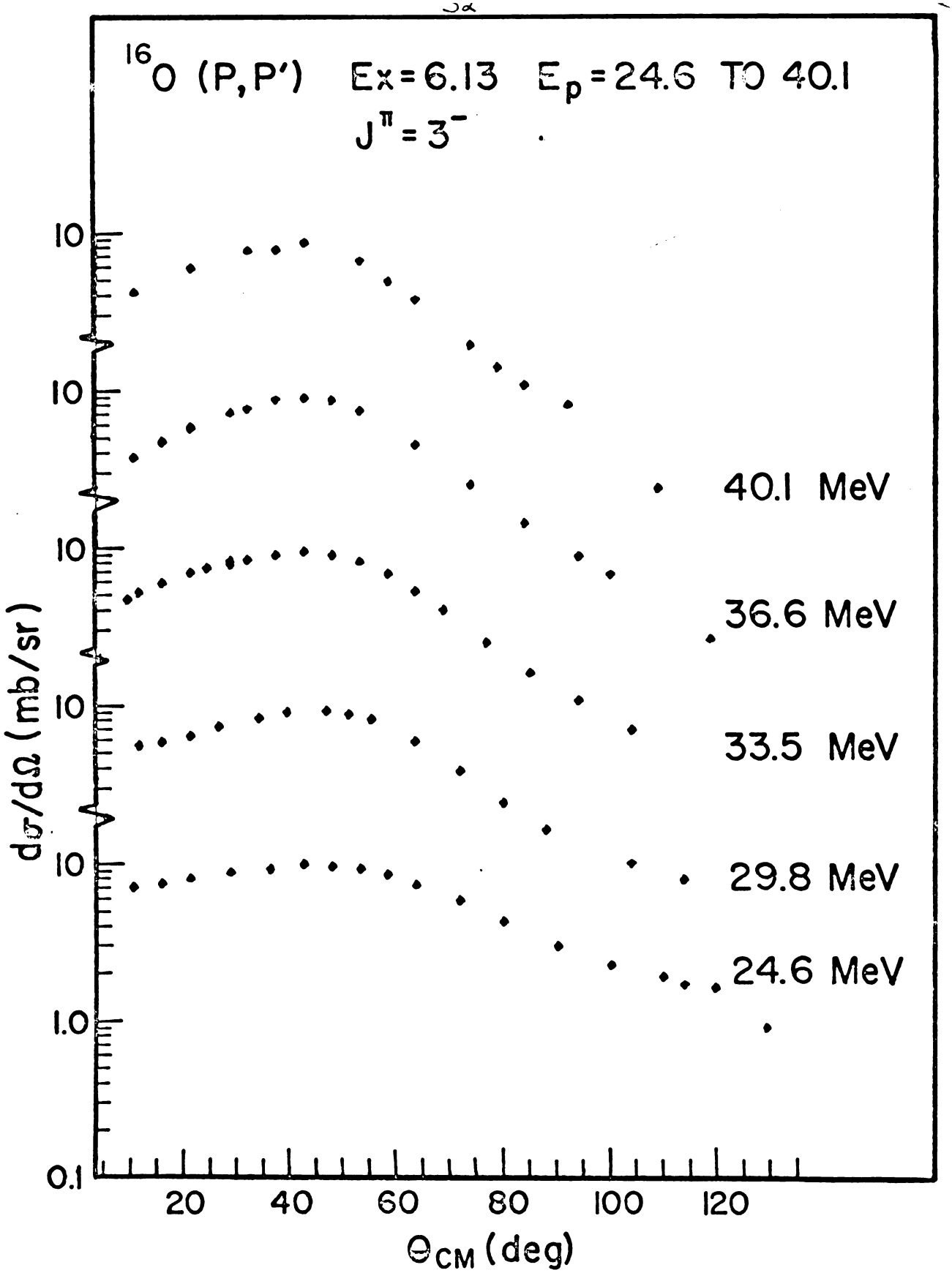

Figure 3.3 Center of mass cross section plotted as a function of scattering angle.

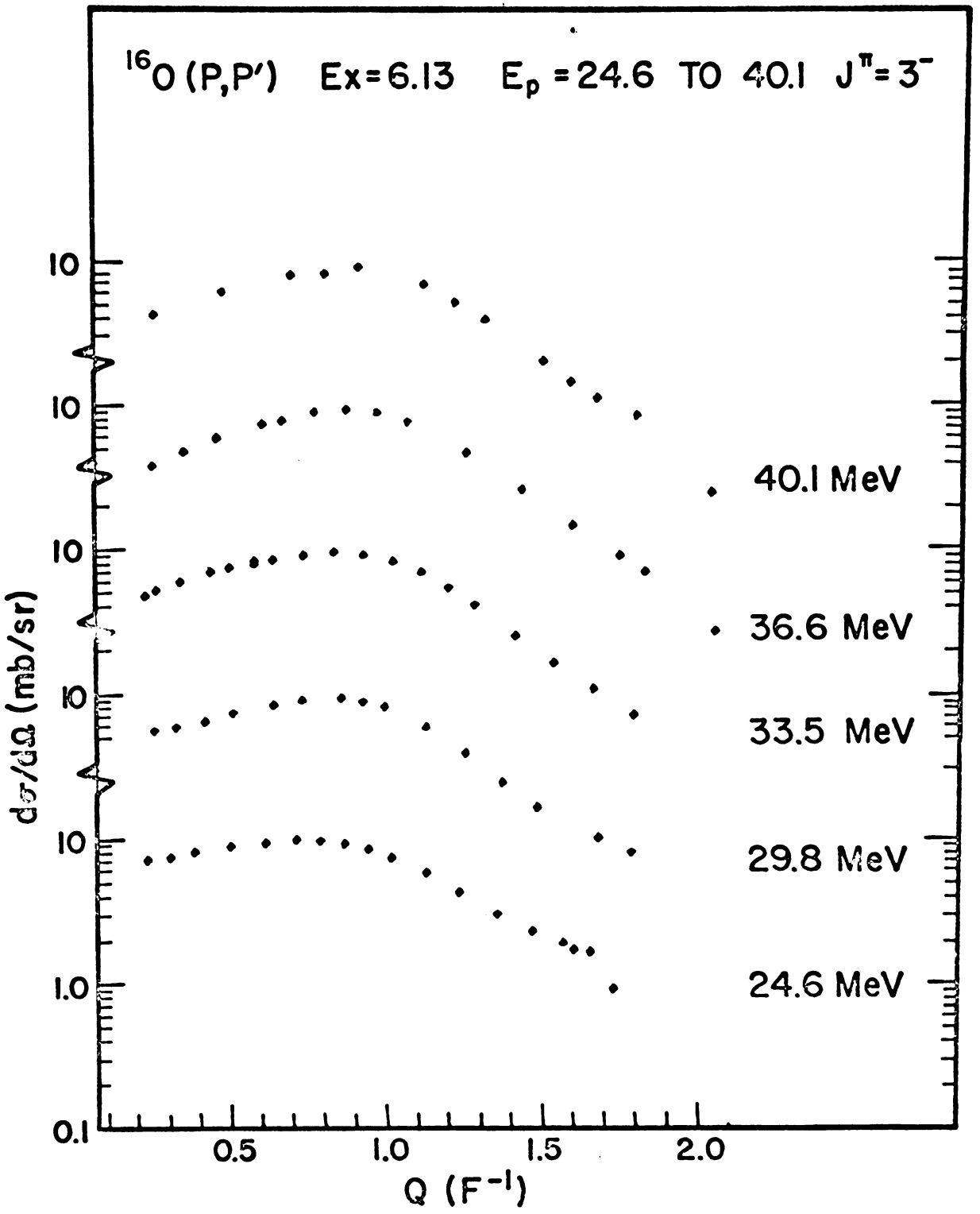

Figure 3.4 Center of mass cross section plotted as a function of $Q = |\vec{k}_i - \vec{k}_f|$

with energy, and the shape as illustrated in the momentum transfer plots, does not change.

The relative strength of the 6.13 to 6.05 MeV state ranges from a minimum of 7:1 at 11° where the 6.05 MeV state is at its maximum, to 60:1 at the maximum of the 6.13 MeV state. These ratios confirm the assumption of Austin et al (Au 70), that the contribution of the 6.05 MeV state could be neglected in evaluation of the angular distribution of the 6.13 MeV state.

The sum of the 6.05 and 6.13 MeV angular distributions in the present work were compared with the cross sections for the unresolved doublet measured by Austin. The agreement was found to be very good at 24.6, 36.6 and 40 MeV. At 29.8 and 33.5 the agreement was good from 30° to 110°, however the Austin cross sections fall off much more rapidly between 30° and 20° than the present measurements, being 30% lower at 22°.

3.3 The 6.92 MeV State

The differential cross section of this state at the lower energies decreases rapidly from 10° to 20°, level off, then drop an order of magnitude between 40° and 65°. The second maximum is considerable weaker than was observed by Crawley (Cr 65) at 17.5 MeV. The energy dependence of the cross section of this state exhibits a monotonic decrease in the forward angles with no apparent change in the shape beyond $0.6f^{-1}$.

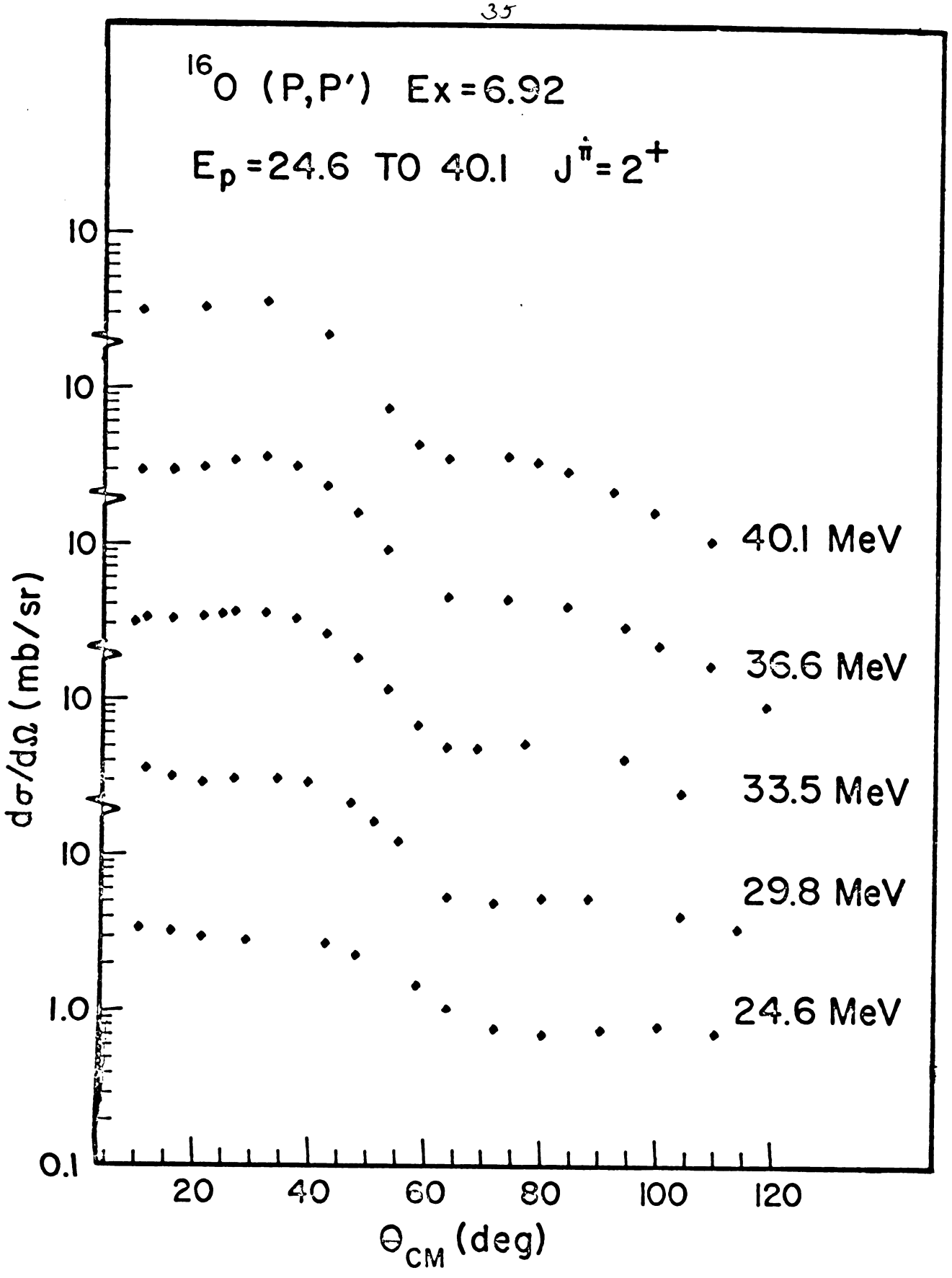

Figure 3.5 Center of mass cross section plotted as a function of scattering angle.

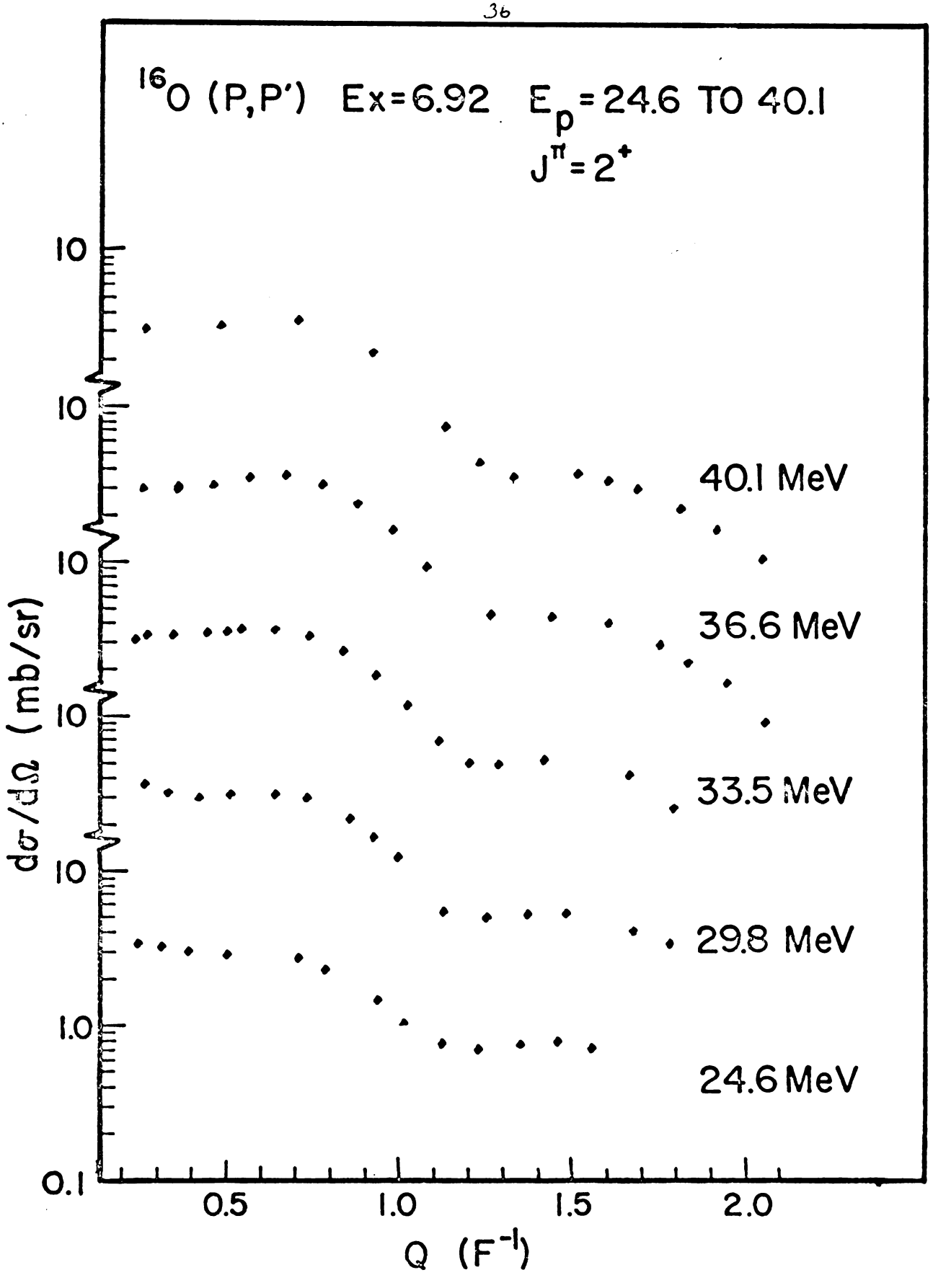

Figure 3.6 Center of mass cross section plotted as a function of $Q = |\vec{k}_i - \vec{k}_f|$

3.4 The 7.12 MeV State

The differential cross section of the $J^{\pi} = 1^{-}$ state at 7.12 MeV rises rapidly from 10° to 20°, levels off, then exhibits a weak, broad second maximum between 45° and 65°. The energy dependence appears to be smooth, with the second maximum growing slightly stronger with energy. Beyond 65° the angular distributions drop off slowly. The shape observed agrees with that of Crawley (Cr 65) at 17.5 MeV. In the E_p = 29.8 MeV measurement electronic difficulties resulted in the loss of the angular distribution for this state. The analysis is not seriously affected due to the slow, smooth variation with energy of this state.

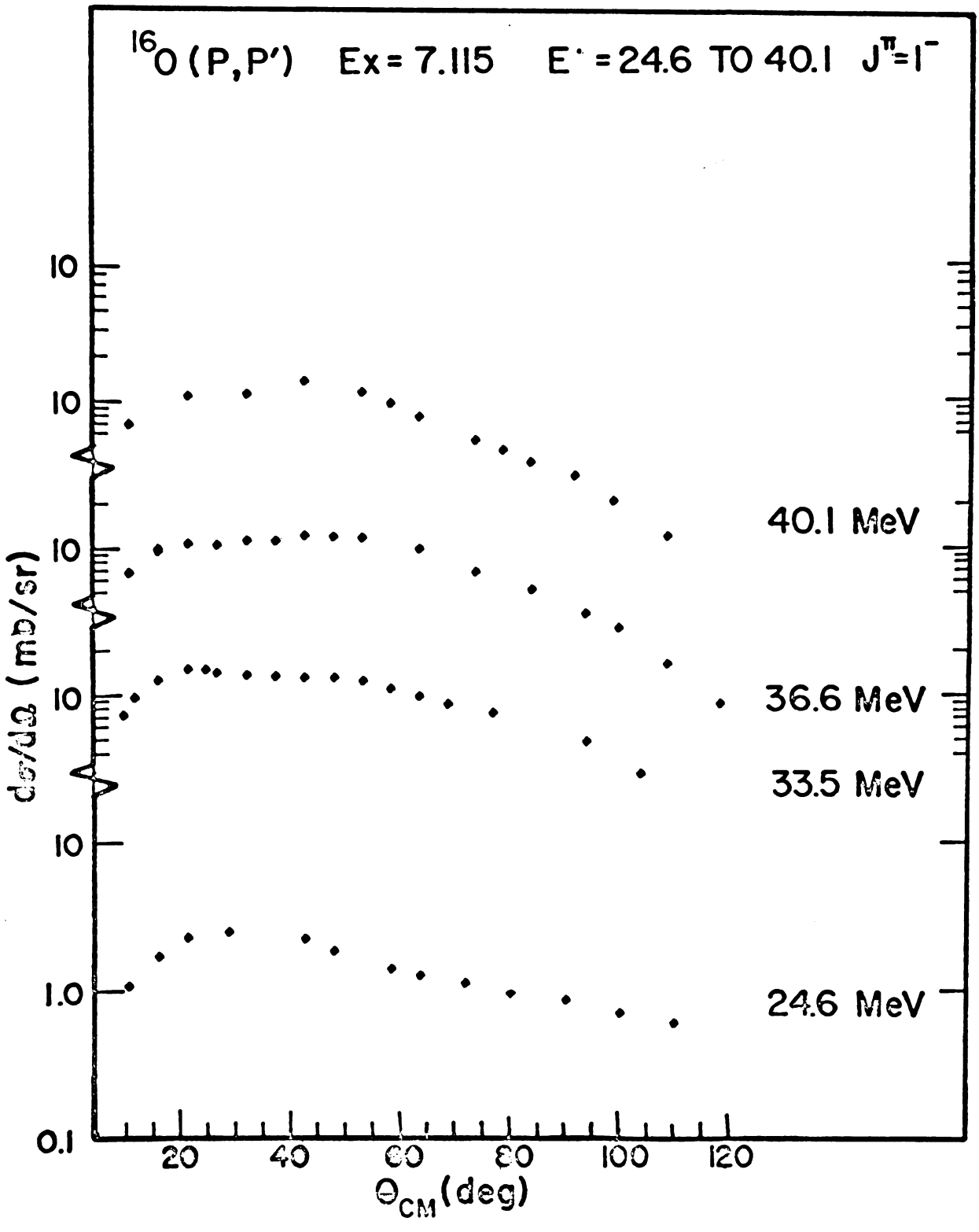

Figure 3.7 Center of mass cross section plotted as a function of scattering angle.

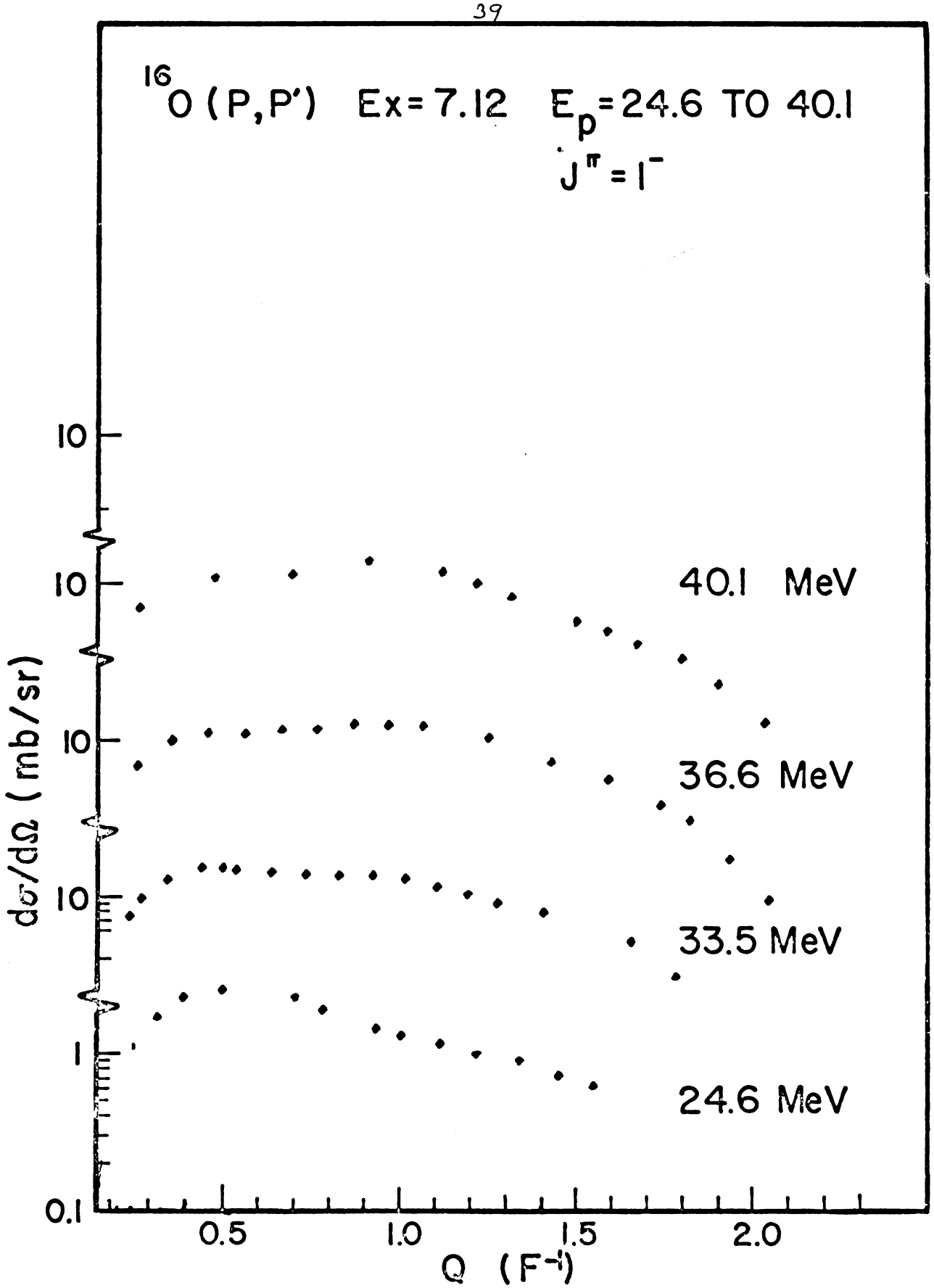

Figure 3.8 Center of mass cross section plotted as a function of $Q = |\vec{k}_i - \vec{k}_f|$

4. NUCLEAR THEORY

A direct reaction is defined as one which excites only one degree of freedom in the target nucleus (Au 61). Proton inelastic scattering at the energies considered is assumed to be a one step process. The interaction involves only the projectile and one nucleon, providing a direct measure of various components of the nuclear force. Since only one nucleon is affected by the interaction, the cross section will be dominated by a direct overlap between the initial and final states. Provided that the correct form of the operator which causes the transition is available, the (p,p') results can be a powerful tool for investigating the structure of the initial and final wave functions.

The calculations were all carried out within the framework of the distorted wave method (D.W.M.). In this approximation the scattering process is pictured as a transition between elastic scattering states. The distorted waves used for the entrance and exit channel, derived in the optical model approximation, cannot be expressed in simple analytical forms, hence the computer code "TAMURA" was used in all calculations except a few test cases which were run with "JULIE" for comparison. Extensive discussions of DWM have been presented by Tobocman (To 61) and Satchler (Sa 64). The most important features of the theory and the approximations employed are discussed in the following sections.

4.1 DWBA Formalism

It can be shown (Sa 64) that the cross section for the inelastic scattering process A(a,b)B is given by

$$\frac{d\sigma}{d\Omega} = \left(\frac{\mu_a}{2\pi\hbar^2}\right)^2 \frac{1}{2(2J_A+1)} \frac{k_b}{k_a} \sum_{\substack{M_A M_B \\ m_a m_b}} |T_{DW}|^2 \quad (1)$$

where μ_a is the reduced mass of the projectile, J_A is the spin of the target, and T_{DW} is the transition amplitude given by

$$T_{DW} = \int\int \chi_b^{(-)*}(\vec{k}_b,\vec{r}_b) \langle bB|V|aA\rangle \chi_a^{(+)}(\vec{k}_a,\vec{r}) d\vec{r}_a d\vec{r}_b \quad (2)$$

The $\chi(k,r)$ are the distorted waves describing motion in the entrance and exit channels. The remaining factor, $\langle bB|V|aA\rangle$, refered to as the nuclear form factor, is the matrix element of the interaction V taken over internal states of the colliding pair. It is a function of r_a and r_b and plays the role of the effective interaction which induces the transition between the initial and final elastic scattering states.

4.2 Form Factors

In order to isolate the radial dependence, the interaction V is expanded in a multipole series

$$V(\vec{r},\vec{x}_a,\vec{x}_A) = \sum_{LSJ\mu} (-)^{J-\mu} V^T_{LSJ,\mu}(r,\vec{x}_A) T_{LSJ,-\mu}(\hat{r},\vec{x}_a) \quad (3)$$

where x_a, x_A represent the internal coordinates of a and A respectively. In this expansion we have assumed that $\vec{r}_a = \vec{r}_b$ in (2). The spin angle tensor $T_{LSJ,\mu}$ is defined by

$$T_{LSJ,\mu} = \sum_m \langle LSm, \mu - m | J\mu \rangle i^L Y_{Lm}(\hat{r}) S_{s,\mu-m}(\hat{x}_a) \quad (4)$$

By construction, $V_{LSJ,\mu}$ is a spherical tensor of rank J. Inserting the expansion for V into the nuclear form factor we have (Sa 66)

$$\langle bB|V|aA\rangle = \sum_{TLSJ} i^{-L} G^T_{LSJ}(r) Y^*_{Lm}(\hat{r})(-)^{S_a - m_a'}$$

$$\times \langle S_a S_b\, m_a, -m_b | S\, m_a - m_b \rangle$$

$$\times \langle J_A\, J\, M_A, M_B - M_A | J_B\, M_B \rangle \langle LSm, m_a - m_b | JM_B - M_A \rangle$$

$$\times \langle T_A\, T\, \tau_A, \tau_B - \tau_A | T_B\, \tau_B \rangle \langle t_a\, T\, \tau_b, \tau_B - \tau_A | t_a\, \tau_A \rangle \quad (5)$$

where the nuclear quantum numbers have been specified in detail in an obvious notation. The transfered angular momentum $\vec{L}$, $\vec{S}$, and $\vec{J}$ are defined by the vector relations

$$\vec{J} = \vec{J}_A - \vec{J}_B, \quad \vec{S} = \vec{S}_a - \vec{S}_b, \quad \vec{L} = \vec{J} - \vec{S}.$$

The radial form factors G(r) are expressed in terms of reduced matrix elements of the various multipoles of the interaction (3),

$$G^{0}_{LOL}(r) = \sqrt{2S_a+1}\ \langle J_B T_B || V^{0}_{LOL}(r,\vec{x}_A) || J_A T_A \rangle \quad (6)$$

where S = T = 0.

Since different values of T contribute coherently to the cross section, it is convenient to take all contributing values together by defining (Sa 66)

$$G_{LSJ}(r) = \sum_T G^{T}_{LSJ}(r) \langle T_A T T_A, T_B - T_A | T_B T_B \rangle \times \langle t_a T T_b, T_B - T_A | t_a T_a \rangle \quad (7)$$

The radial form factors contain all the physics of the inelastic scattering problem. The remainder of this discussion will be concerned with these quantities for the specific models used in the theoretical calculations.

4.3 Collective Model Form Factor

In the collective model the interaction V is derived from a non-spherical potential well which depends only on the distance from the nuclear surface. The derivation of the form factor is given elsewhere (Ba 62). The explicit form used in the present calculations is (Sa 66)

$$G^{0}_{LOL} = \beta_L \left(\frac{2S_a+1}{2L+1}\right)^{1/2} \left\{ \frac{V_R r_R A^{1/3}}{a_R} f(x_R) - \frac{b_L}{r^{L+1}} + i r_I A^{1/3} \left(\frac{W}{a_I} f(x_I) - 4 \frac{W_D}{a_D} \frac{d}{dx_D} f(x_D) \right) \right\} \quad (8)$$

where

$$f(x_i) = \frac{e^{x_i}}{1+e^{x_i}} \quad , \; i = R, \; I, \; D$$

$$x_i = (r - r_i A^{1/3}) \; / \; a_i, \; i = R, \; I, \; D$$

$$b_L = -4.32 \; \frac{Z_a \; Z_A \; a_R \; R_C^L}{V_R \; r_R \; A^{1/3}}$$

$$R_C = 1.25 \; A^{1/3} \text{ fermi}$$

The parameters V_R, W, W_D, r_R, r_I, a_R, and a_I were obtained from the optical potentials of Cameron (Ca 67) and Snelgrove (Sn 68). The deformation parameter β_L was determined by normalizing the theoretical cross sections to the data.

The reduced electromagnetic transition probability B(EL) can be related to the deformation parameter by (Pe 70)

$$B(EL; \; 0 \rightarrow L) = \left(\frac{3Z}{4\pi} \; R_0^L \; \beta_L \right)^2 \qquad (9)$$

where a uniform charge distribution has been assumed.

The B(EL) are then related to the partial transition widths for gamma transitions by (Pr 62)

$$\Gamma_L = \frac{8\pi}{L\left((2L+1)!!\right)^2} \left(\frac{E_\gamma}{\hbar c} \right)^{2L+1} B(EL) \qquad (10)$$

where E_γ is the energy of the emitted gamma ray. Care must be taken in comparison of the deformation extracted from the

inelastic scattering to that extracted from gamma transition rates. The radius R_0 is dependent on the model chosen for the nuclear charge distribution. Gruhn (Gr 69) has shown that the deformations are extremely model dependent. B(EL)'s differing by as much as factors of four were found for different models.

4.4 Microscopic Form Factors

The radial form factor can be separated into two parts by introducing the transition density (Pe 70)

$$F^{LSJ,T}(r_1) = \sqrt{2(2T+1)}\ \langle T_A\ T\ M_A,\ M_{T_B}-M_{T_A} | T_B\ M_{T_B}\rangle$$

$$\times\ \langle 1/2\ T\ T_b,\ T_a - T_b | 1/2\ T_a\rangle$$

$$\times\ \langle J_B T_B\ ||\sum_{i=1}^{N} \frac{\delta(\vec{r}_1-\vec{r}_i)}{r_1^2}\ T_{LSJ}(i)\,T^T(i)\,||J_A T_A\rangle \qquad (11)$$

The radial form factor G now becomes (Pe 70)

$$G_{LSJ}(r) = \sum_T \mathcal{U}_{STL}(r,r_1)\ F^{LSJ,T}(\hat{r}_1)\,r_1^2\,dr_1 \qquad (12)$$

where the multipole coefficient $\mathcal{U}_{STL}(r,r_1)$ is related to $V^T_{LSJ,\mu}(r,x_A)$ of equation (3) by

$$V^T_{LSJ,\mu}(r,\vec{x}_A) = \sum_i \mathcal{U}_{STL}(r,r_i)\ T_{LSJ,\mu}(\hat{x}_A)\ \sigma_i\ .$$

This form of the form factor provides an important separation of the nuclear structure part contained in $F^{LSJ,T}$ from the interaction contained in $\tilde{v}_{STL}(r,r_1)$.

Within the framework of the Born approximation, the electron scattering form factor can be written in terms of the same transition density as the proton scattering (Pe 70)

$$|F(q)|^2 = \frac{\pi}{Z^2} \frac{2J_B+1}{2(2J_A+1)} \sum_L \left| \int_0^\infty j_L(qr) \sum_T F^{LOL,T}(r) r^2 dr \right|^2 e^{\frac{-(qa_p)^2}{2}} \tag{13}$$

where $j_L(qr)$ is the spherical Bessel function.

If harmonic oscillator wave functions are used for the single particle wave functions, the transition density can be written (Pe 70)

$$F^{LSJ,T}(r) = \sum_{N=N_a}^{N_b} C_N^{LSJ} \alpha^{N+3} r^N e^{-\alpha^2 r^2} \tag{14}$$

where $N_a = (l + l')_{min}$

$$N_b = (l + l' + 2n + 2n' - 4)_{max}$$

and where α is the harmonic oscillator strength parameter, l, l' and n, n' are the quantum numbers of the contributing harmonic oscillator wave functions U_{nl}, $U_{n'l'}$.

The quantities C_N^{LSJ} are sums of products of Clebsch-Gordan coefficients and coefficients of fractional parentage. Since the shell model configurations for the 6.05 and 6.92 MeV states of ^{16}O are quite complicated, the coefficients

C_N^{LSJ} were not constructed from the available nuclear wave functions. Instead a least squares fit of equation (13) to the available electron scattering data was used to determine the C_N^{LSJ} .

Three forms of the radial dependence of the interaction were used in the calculations. The Kallio-Kolltveit (K-K) (Ka 64) interaction

$$V = 0 \qquad r < 1.025 \text{ f}$$
$$= V_0 \, e^{-mr} \qquad r \geq 1.025 \text{ f},$$

the Yakawa interaction with a 1 f range,

$$V = V_0 \frac{e^{-\alpha r}}{\alpha r} ,$$

and the Kuo-Brown (K-B) (Ku 66) interaction derived from the long range part of the Hamada-Johnston (Ha 62) potential.

4.5 Optical Parameters

Two sets of optical potentials spanning the energy region of this experiment were available. The potentials of Cameron were of the form

$$V(r) = V_C(r) - V_R \, f(x_R) - iW \, f(x_I) - iW_1 \, e^{-x_I^2}$$
$$+ (V_{SO} + iW_{SO}) \frac{4}{r} \frac{d}{dr} f(x_{SO}) \, \vec{s} \cdot \vec{l}$$

where $V_C = ZZ'e^2/r \qquad r \geq R_C$

$$= \frac{ZZ'e^2}{2R_C}\left(3 - \frac{r^2}{R_C^2}\right) \qquad r < R_C$$

and $f(x_i) = (1 + e^{x_i})^{-1} \qquad i = R, I, I', SO$

$$x_i = (r - r_i A^{1/3})/a_i \qquad i = R, I, I', SO$$

where r_i are the radius parameters and a_i are diffuseness parameters. These parameters are listed in Table 4.1.

This potential contains a Gaussian surface imaginary term while the DWM codes assume a derivative Woods-Saxon form:

$$4W_D \frac{d}{dx_D}(1 + e^{x_D})^{-1} \; ; \; x_D = (r - r_I A^{1/3})/a_D \; .$$

It was assumed that the derivative of the Woods-Saxon potential had the same strength and width at half maximum as the Gaussian potential; thus $W_1 = W_D$; and $a_D = 0.472a_I$. These potentials were used in most of the calculations because the fits were made to data at bombarding energies closest to those of this experiment.

The other optical potentials were those of Snelgrove (Sn 68) which were of the form

$$V(r) = V_C - V_R f(x_R) - i(W_S - 4W_D \frac{d}{dx_I}) f(x_I)$$
$$+ V_{SO}\left(\frac{\hbar}{m_\pi C}\right)^2 \frac{1}{r}\frac{d}{dr} f(x_R)\,(\vec{I}\cdot\vec{\sigma})$$

where $V_C(r)$ and $f(x)$ are as defined above. The fits obtained with these parameters were within 10% of those obtained with Cameron's, hence were used mainly as a consistancy check throughout this work.

Table 4.1 Optical Parameters

Optical parameters of Cameron (Ca 67)

E_p	V_R	W	W_D	V_{SO}
	(MeV)	(MeV)	(MeV)	(MeV)
23.4	47.25	0.0	7.06	4.09
24.5	44.51	0.0	6.83	5.41
27.3	48.43	0.0	7.28	5.63
30.1	47.50	0.0	8.35	6.82
34.1	47.02	2.31	6.52	6.44
36.8	46.37	0.28	8.55	7.98
39.7	46.58	2.25	7.65	7.32
43.1	44.67	3.15	6.32	6.20

The geometrical parameters are:

r_R = 1.142 F r_I = 1.268 F r_{SO} = 1.114 F

a_R = 0.726 F a_I = 0.676 F a_{SO} = 0.585 F

a_D = 0.463 F r_c = 1.25 F

Snelgrove average optical parameters are (Sn 68)

V_R	W	W_D	V_{SO}
(MeV)	(MeV)	(MeV)	(MeV)
46.8	0.80	6.20	7.0

Table 4.1 cont.

The geometrical parameters are:

$r_R = r_{SO} = 1.12$ F $\quad r_I = 1.35$ F $\quad r_c = 1.15$ F

$a_R = a_{SO} = 0.60$ F $\quad a_I = 0.48$ F

5. COMPARISON OF DATA TO THEORY

5.1 Collective Model

The calculations for the 3^- state at 6.13 MeV, shown in Figure 5.1, exhibit the correct phase and general shape, but do not agree in detail with the data. At all energies the fits tend to fall off more rapidly than the data between 50° and 100°. A shoulder predicted by the theory from 85° to 110° is not observed.

The calculations for the 2^+ state at 6.92 MeV were also in general agreement with the data. The slope of the forward angle differential cross section was too large at all energies, but was better at higher bombarding energies. The calculations reproduced the position and relative magnitude of the second maximum but tended to drop off more sharply than the data.

The calculations for the 1^- state at 7.12 MeV displayed much more structure than the data. The first and second minimum as well as the second and third maximum predicted by the theory were not observed.

5.2 Microscopic Model

The coefficients C_N^{LSJ} of equation (14) were determined for all states by a least squares fit of the electron scattering form factor defined by equation (13) to the data of Bergstrom et al (Be 70) and Crannel (Cr 66). For the 7.12

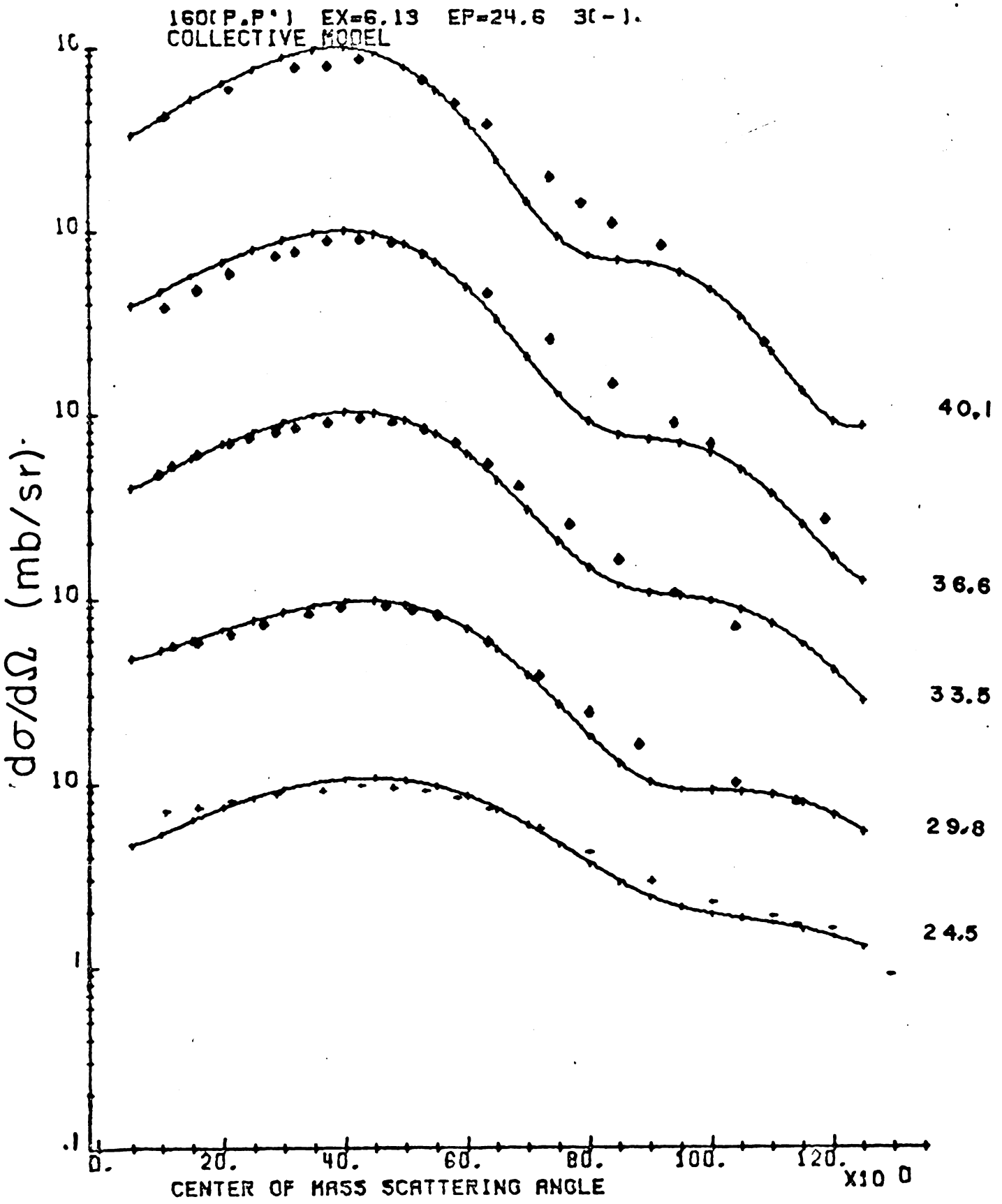

Figure 5.1 DWM calculations for the 6.13 MeV state. Normalizations were extracted from the integrated cross sections.

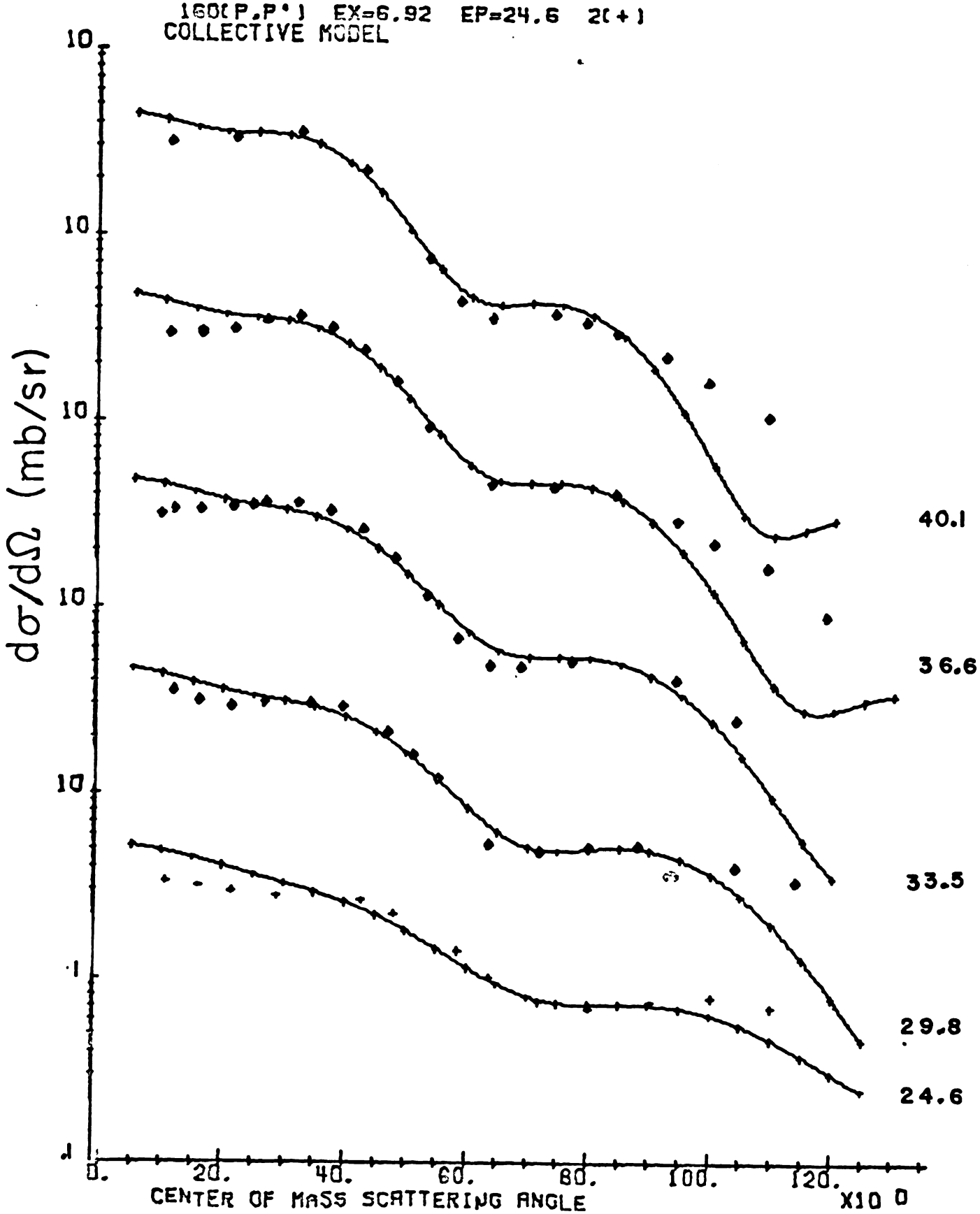

Figure 5.2 DWM calculations for the 6.92 MeV state. Normalizations were extracted from the integrated cross sections.

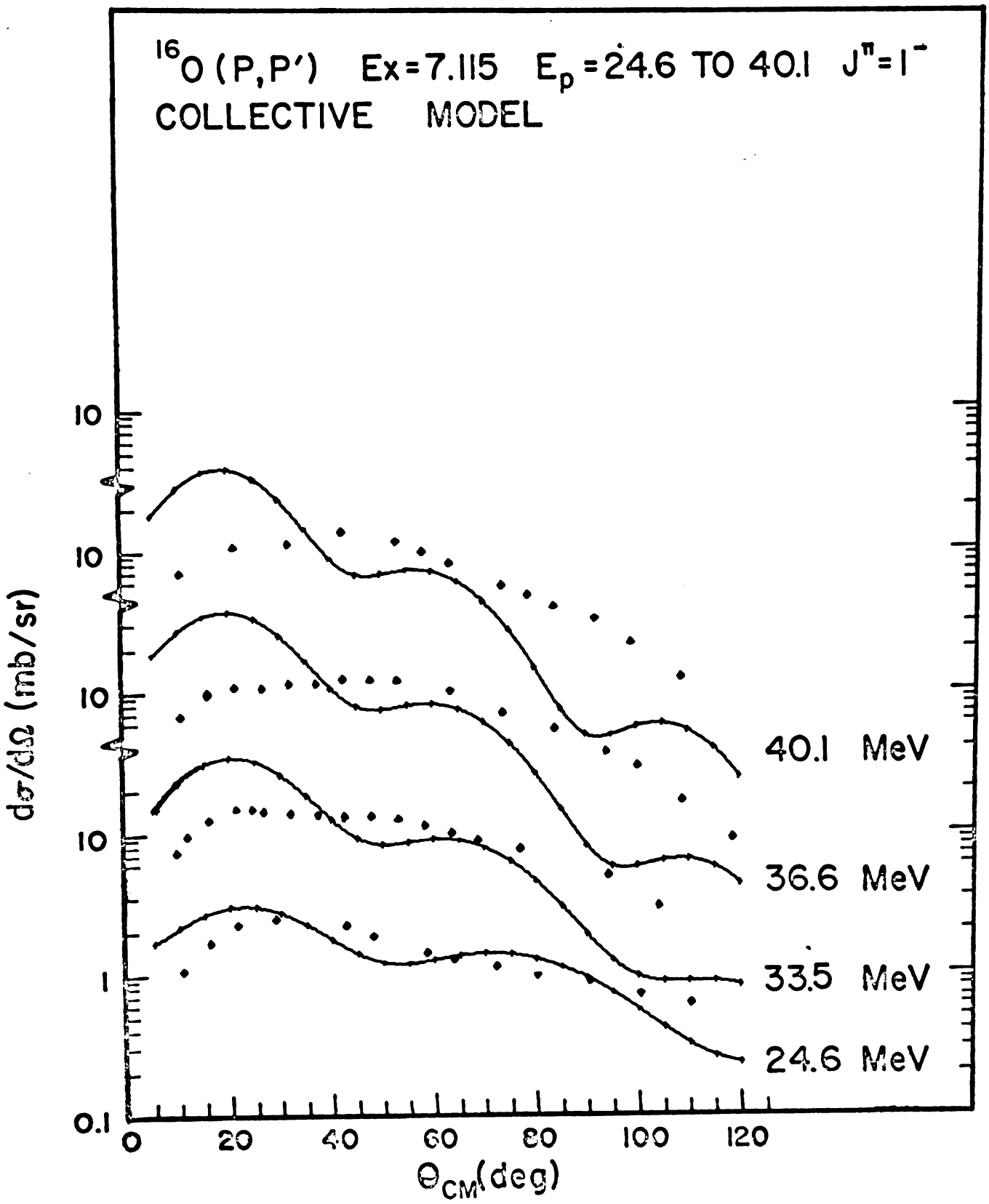

Figure 5.3 DWM calculations for the 7.12 MeV state. Normalizations were extracted from the integrated cross sections.

Table 5.1

Deformation parameters β_L extracted from collective model fits at five bombarding energies.

Excitation Energy MeV	24.6 MeV	29.8 MeV	33.5 MeV	36.6 MeV	40.1 MeV	E.M.
6.13	0.66±0.05	0.57±0.04	0.58±0.03	0.58±0.03	0.56±0.03	0.52*
6.92	0.27±0.01	0.25±0.01	0.26±0.01	0.26±0.01	0.26±0.01	0.25*
7.12	0.26±0.01	----	0.20±0.01	0.20±0.01	0.20±0.01	0.0035*

Errors quoted are the statistical errors added in quadrature with the discrepency found by using different sets of optical parameters.

*Deformations were extracted from electromagnetic transitors assuming uniform charge distribution with the Fermi equivalent r.M.S. radius (El 61).

MeV state, the C_N^{LSJ} were constructed from the wave functions of Gillet and Vinh Mau (Gi 64). Since these wave functions for the 6.13 MeV state were used by Austin et al (Au 70), these calculations were not repeated.

The inelastic electron scattering data illustrated in Figure 5.4 for the 6.13 MeV state covers the entire range of momentum transfers spanned by proton inelastic scattering, providing a good test of this method.

The explicit transition densities $F^{LSJ,T}$ obtained from the fitting procedure were:

$$F^{000,0} = (1.47\ \alpha^3 - .922\ \alpha^5\ r^2)\ e^{-\alpha^2 r^2}$$

$$F^{303,0} = (-0.537\ \alpha^4 r + 1.89\ \alpha^6 r^3 - 0.111\ \alpha^8 r^5)\ e^{-\alpha^2 r^2}$$

$$F^{202,0} = (-1.41\ \alpha^5 r^2 + .900\ \alpha^7 r^4)\ e^{-\alpha^2 r^2}$$

$$F^{101,0} = (3.87\ \alpha^4 r - 1.57\ \alpha^6 r^3)\ e^{-\alpha^2 r^2}$$

The chi-square searches were undertaken with the hope that the coefficients C_N would converge to values which reflect the shell model configurations from which the states are to be constructed. This was not found to be the case. The coefficients of the terms in the transition density were not uniquely determined by the fitting procedure. A wide range of parameters were found to give approximately the same values of X^2. One finds that the more parameters one allows to enter into the expansion, the better the fit that is obtained.

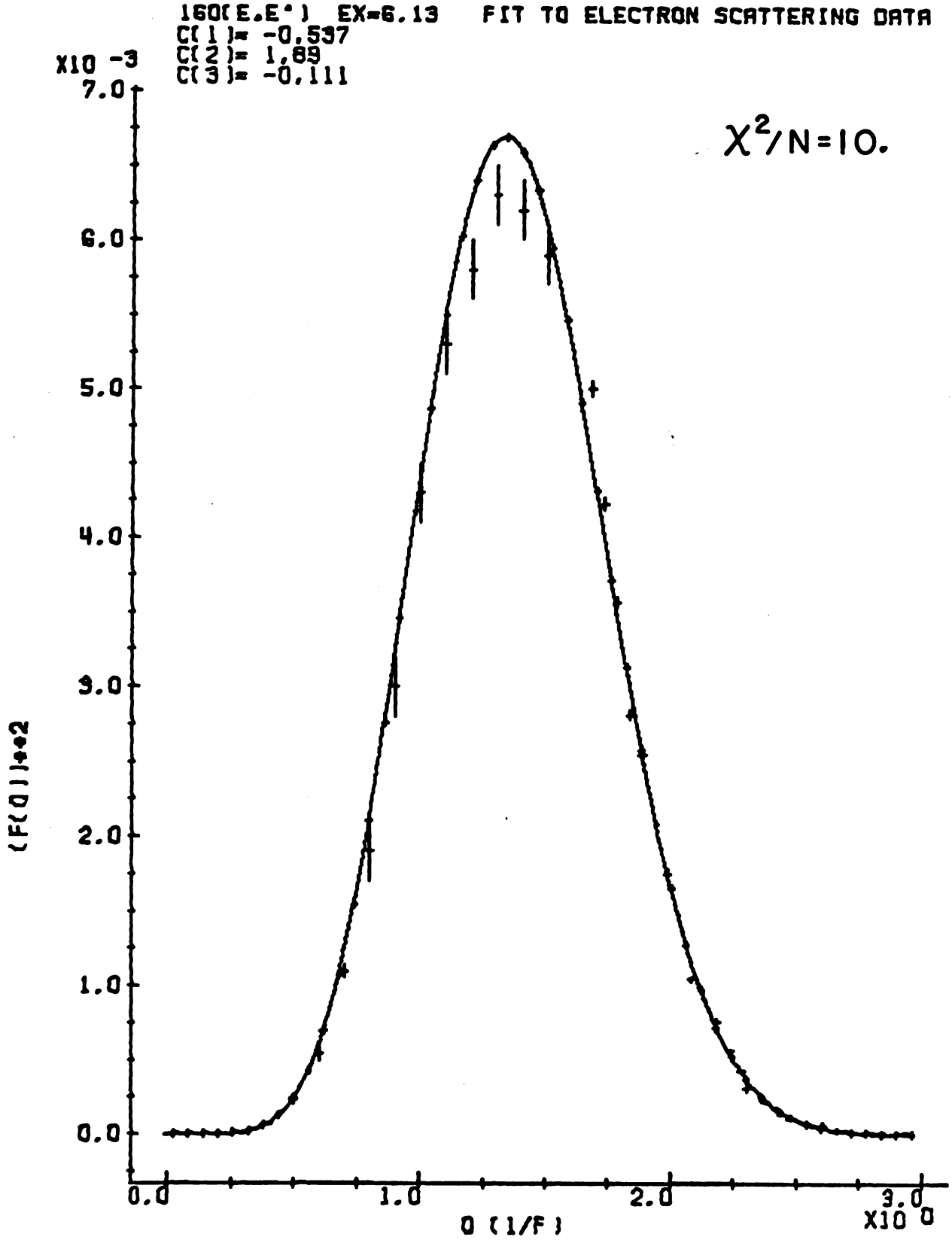

Figure 5.4 Electron scattering form factor using the transition density extracted from the least squares fit.

On the basis of this experience, no structure information can be extracted from the fits. The expansion in terms of harmonic oscillator wave functions is to be viewed as a convenient form because it provides coefficients which can be input directly into available form factor codes.

5.3 Comparison of Microscopic Fits to the Data

The calculations for the first excited 0^+ state at 6.05 MeV were very poor at lower energies but improved significantly as the energy increased. This improvement was due to a slight increase in the structure exhibited by the calculations and a rather large decrease in the structure of the experimental angular distribution.

The rather large discrepancy at forward angles is particularly disappointing because the electron scattering data shown in Figure 5.5 covered the corresponding momentum transfer range. The underestimate of the second maximum is not a serious problem for two reasons: first because the electron scattering data did not exist for the corresponding momentum transfers requiring extrapolation of the transition density. Secondly, the shape of the angular distribution in this region is very sensitive to the point at which the form factor crosses zero (Figure 5.8). By forcing the form factor to cross zero 0.4 fermi closer to nuclear center, the second maximum could be reproduced at all energies.

Inclusion of the exchange contribution increased the forward angle cross section by approximately a factor of 2.5

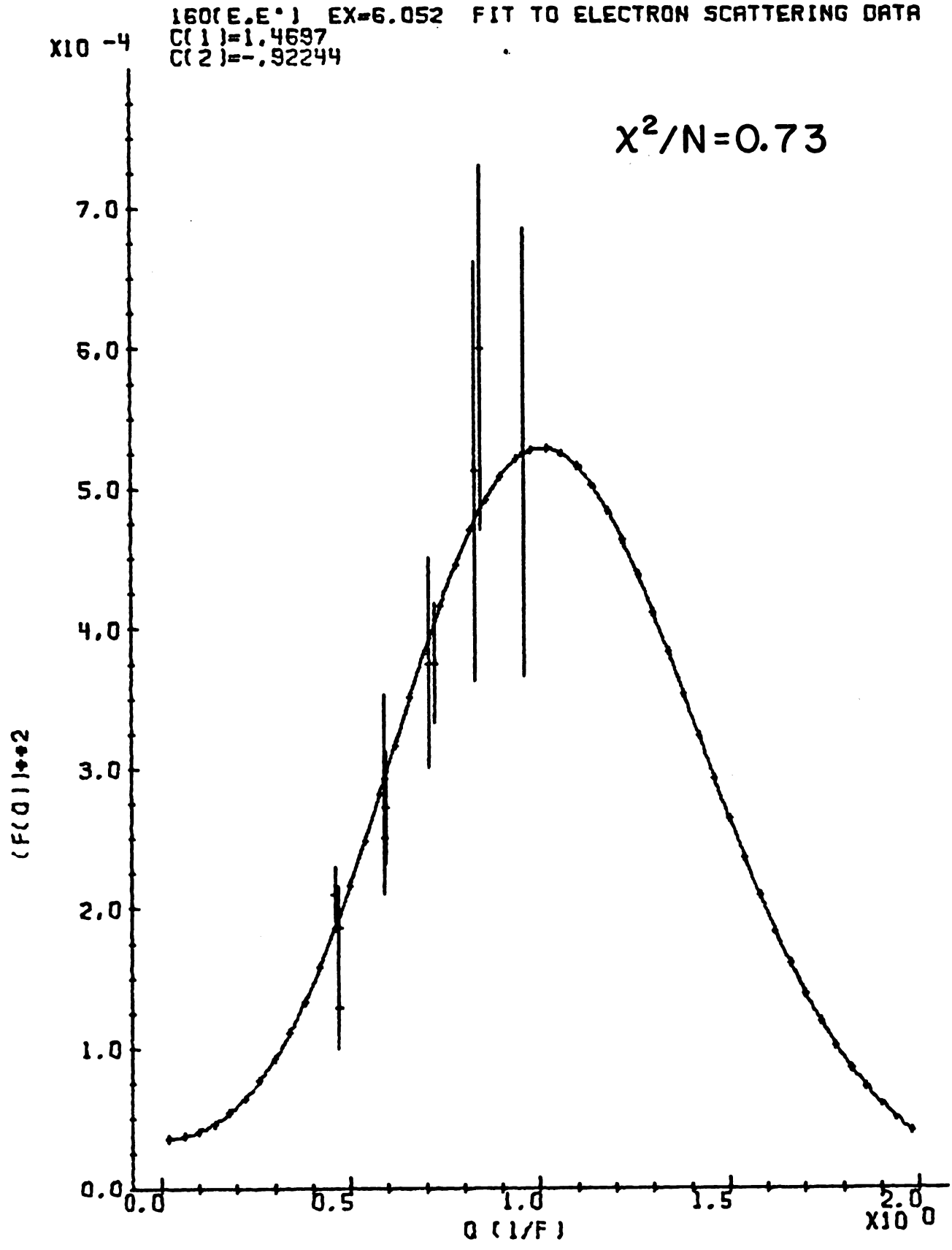

Figure 5.5 Electron scattering form factor using the transition density extracted from the least squares fit.

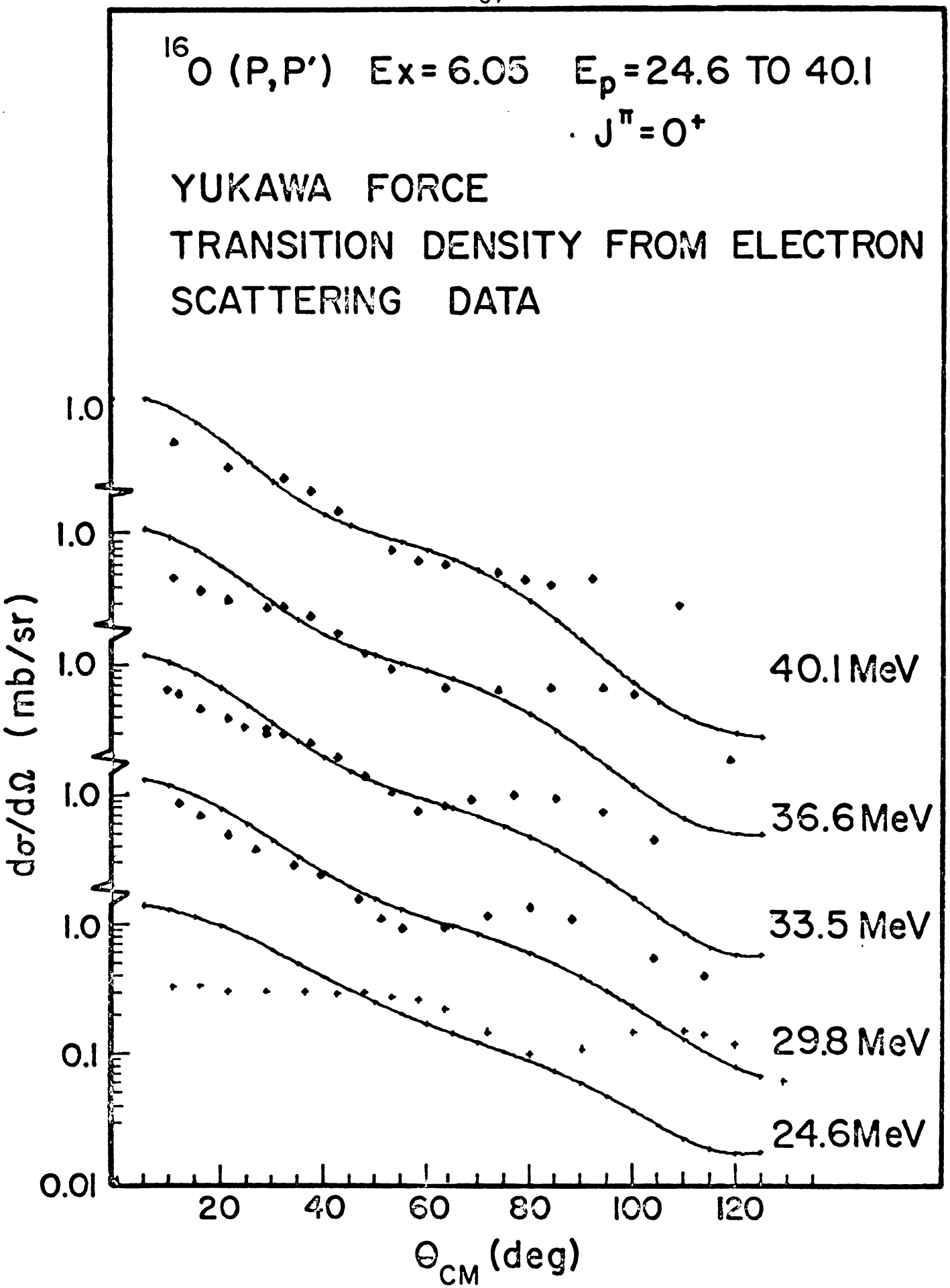

Figure 5.6 DWM microscopic calculations using a 1f range Yukawa interaction. The strengths were extracted from the integrated cross sections.

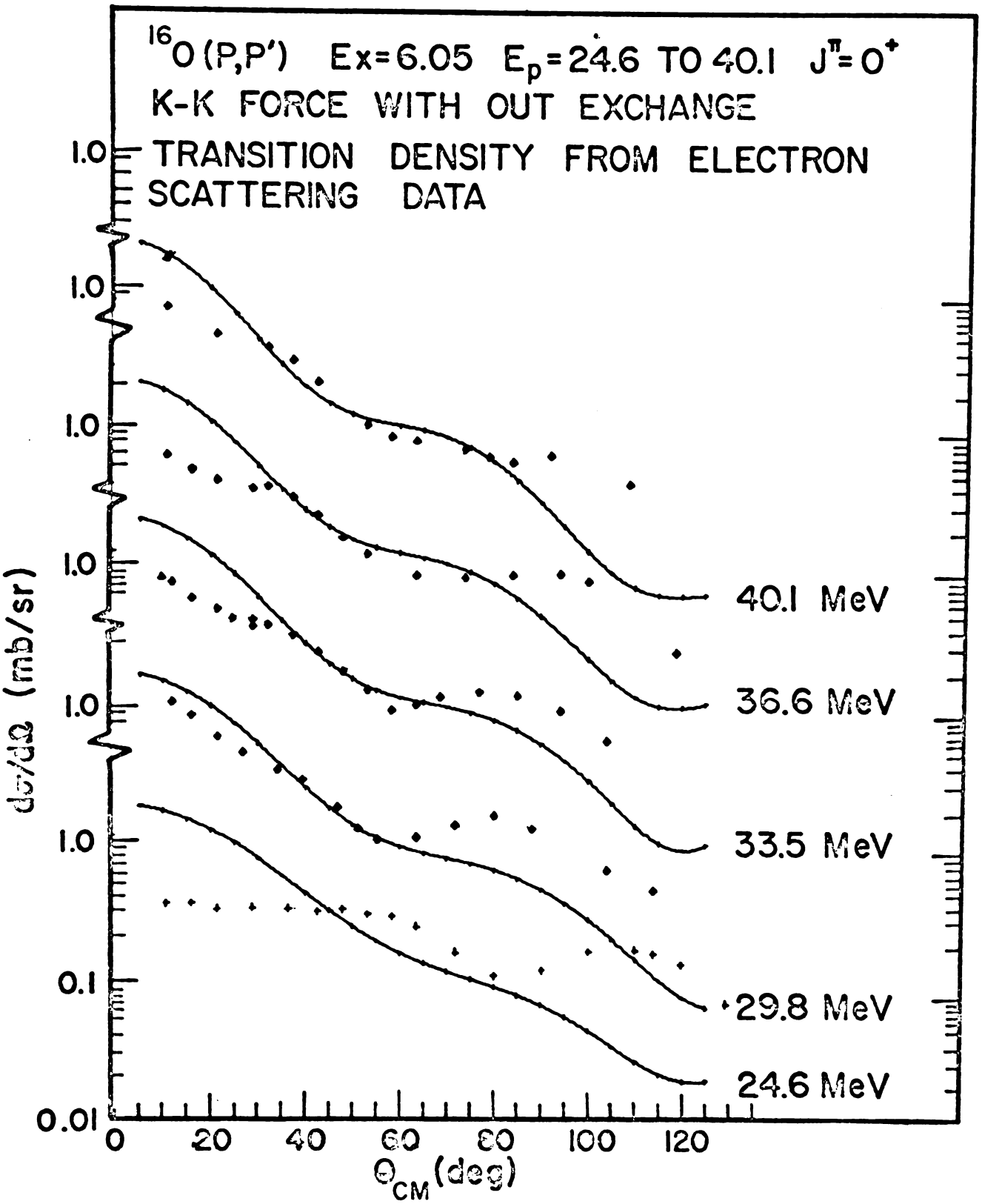

Figure 5.7 DWM microscopic calculations using the long range part of the K-K interaction.

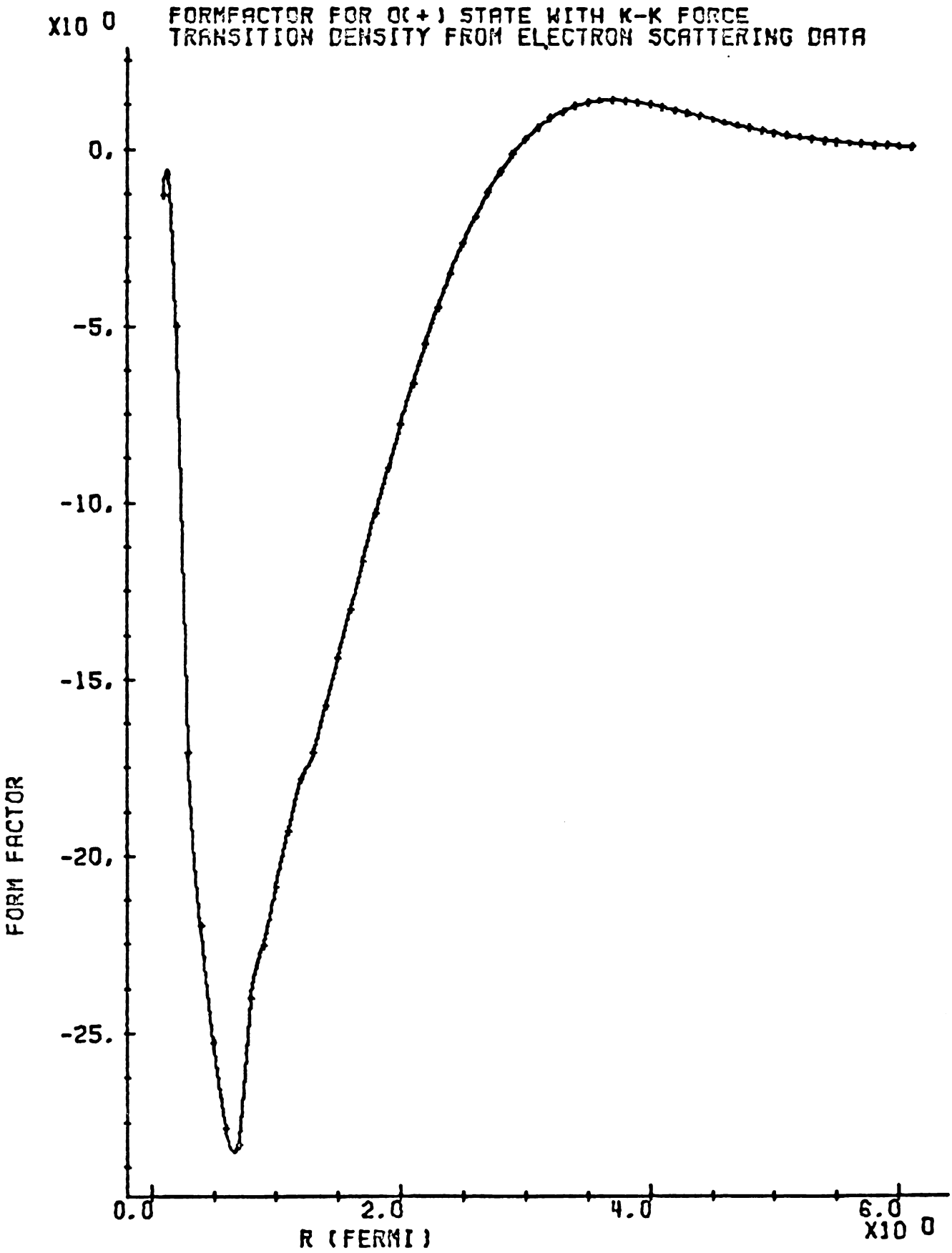

Figure 5.8 The form factor for the 6.05 MeV state without including exchange.

and the total cross section by a factor of 3. The second maximum between 60° and 80° was enhanced slightly.

The fits obtained using the K-B and K-K force were identical in shape with the K-B being approximately 28% smaller.

The Yukawa potential was also very similar in shape to that of the K-K and K-B, but slightly less forward peaked and thus in somewhat better agreement with the data. The strength of the effective interaction was extracted by normalizing the integrated cross section of the DWM calculation to that of the data. The meaning of this strength is somewhat clouded by the quality of the fit. These strengths are presented in Table 5.2.

5.4 The 6.13 MeV State

The calculations with the K-K, K-B, and Yukawa forces with the exchange contribution included, were all very similar. The K-K and K-B interactions predicted identical shapes with the K-B force about 35% smaller in magnitude. The Yukawa fell off slightly more rapidly with angle, thus providing the best fit.

The calculated cross sections reproduced the data out to about 50°. From 50° to 70° the calculations with the exchange contribution included overestimated the cross section. This overestimate reached approximately 45% by 70°. Calculations neglecting the exchange contribution, when

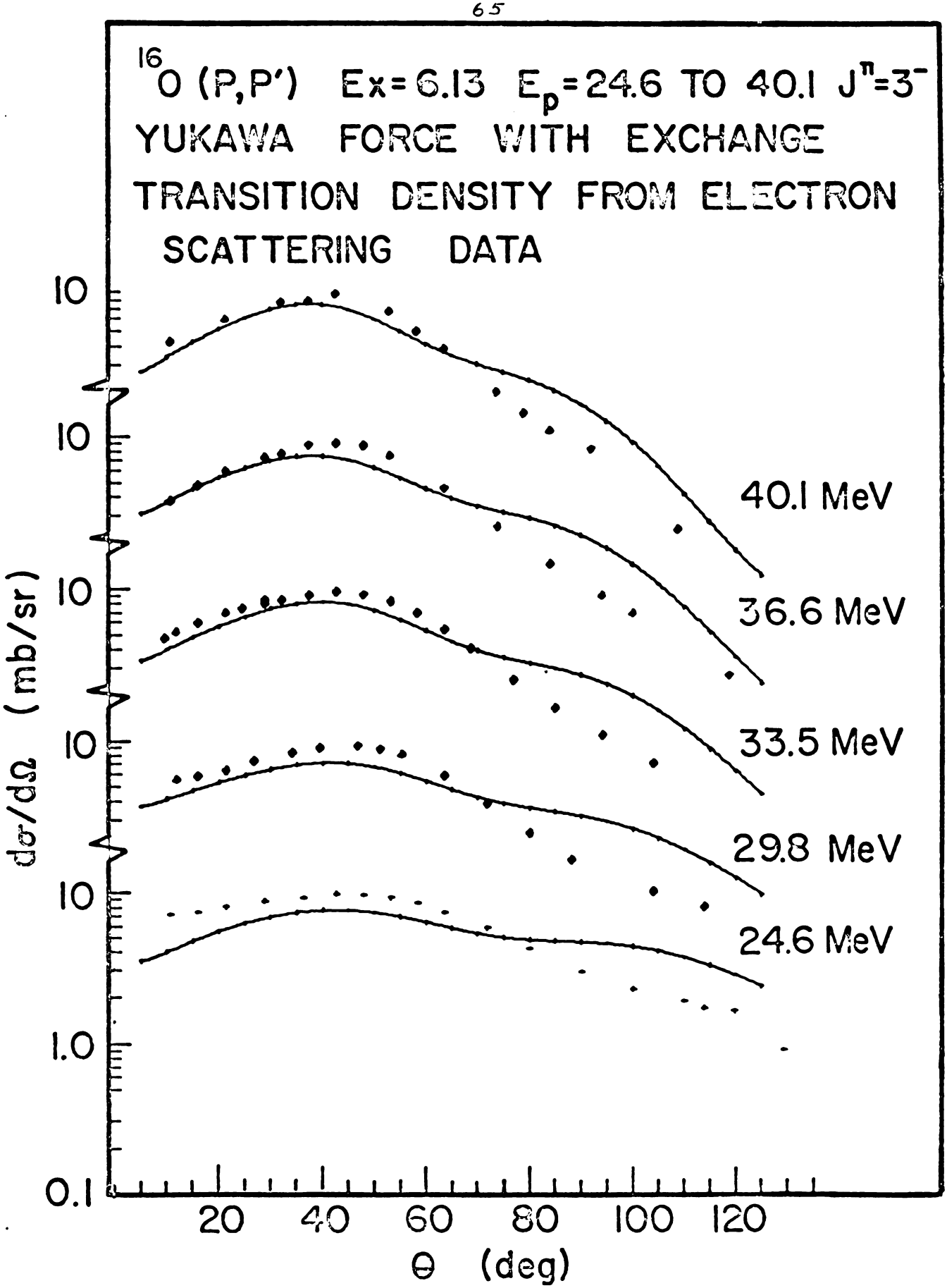

Figure 5.9 DWM calculations using a 1f Yukawa interaction. The strengths were extracted from the integrated cross sections.

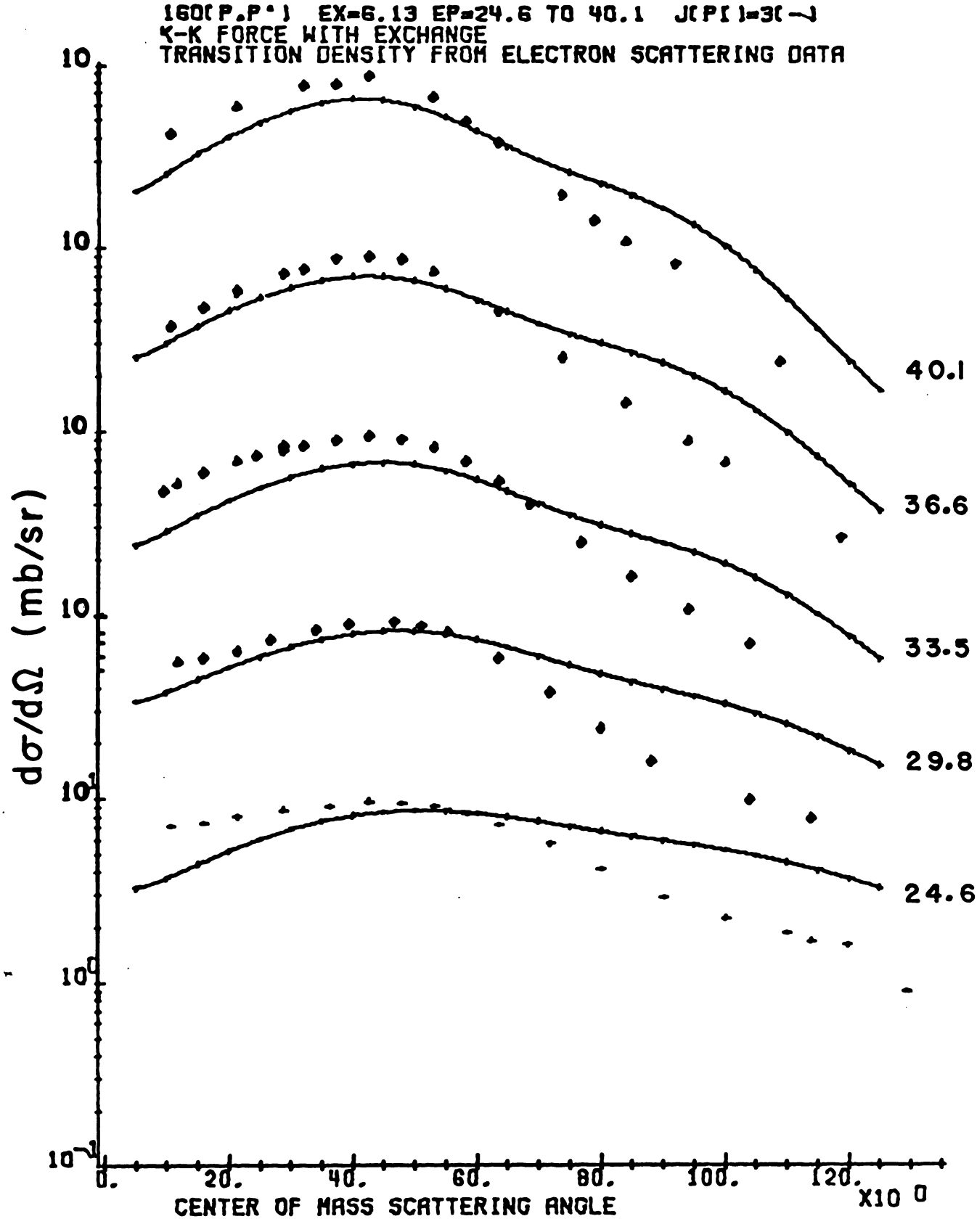

Figure 5.10 DWM calculations using the long range part of the K-K interaction.

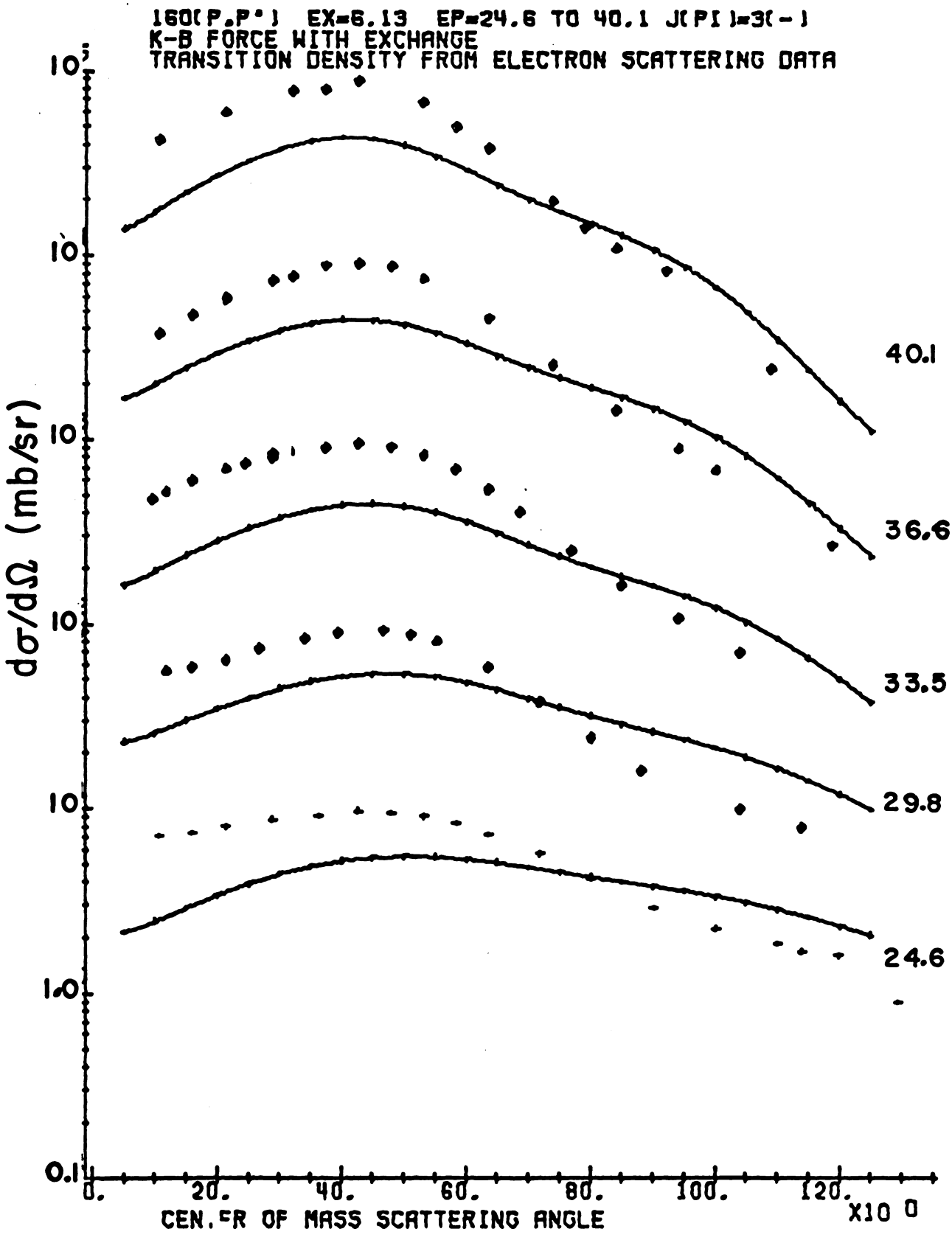

Figure 5.11 DWM calculations using the K-B interaction.

normalized to the data at 40°, underestimate the data by approximately 20% from 50 to 75°. This implies that the approximate method for including exchange tends to exaggerate its affect in this region.

Beyond 75° all calculations overestimate the cross section. This overestimate is attributed to the fact that the electron scattering data in the corresponding momentum transfer region did not resolve the 2^+ and 1^- states from the 3^-. The transition density extracted from the fits includes contributions from these states and is expected to overestimate the 3^- cross section.

5.5 The 6.92 MeV State

The Yukawa and K-K interactions, as in the case of the 6.13 and 6.05 MeV states gave very similar fits. Both forces overestimate the forward angle cross section and reach their first minima and maxima about 10° early. The exchange contribution again overestimates the large angle cross sections. These calculations are illustrated in Figure 5.13 and 5.14. Figure 5.12 shows the fit to the electron scattering data.

The strengths extracted for the Yukawa interaction are listed in Table 5.2.

5.6 The 7.115 MeV State

The electron scattering data for this state, as is evidenced by the fit in Figure 5.15 did not cover a

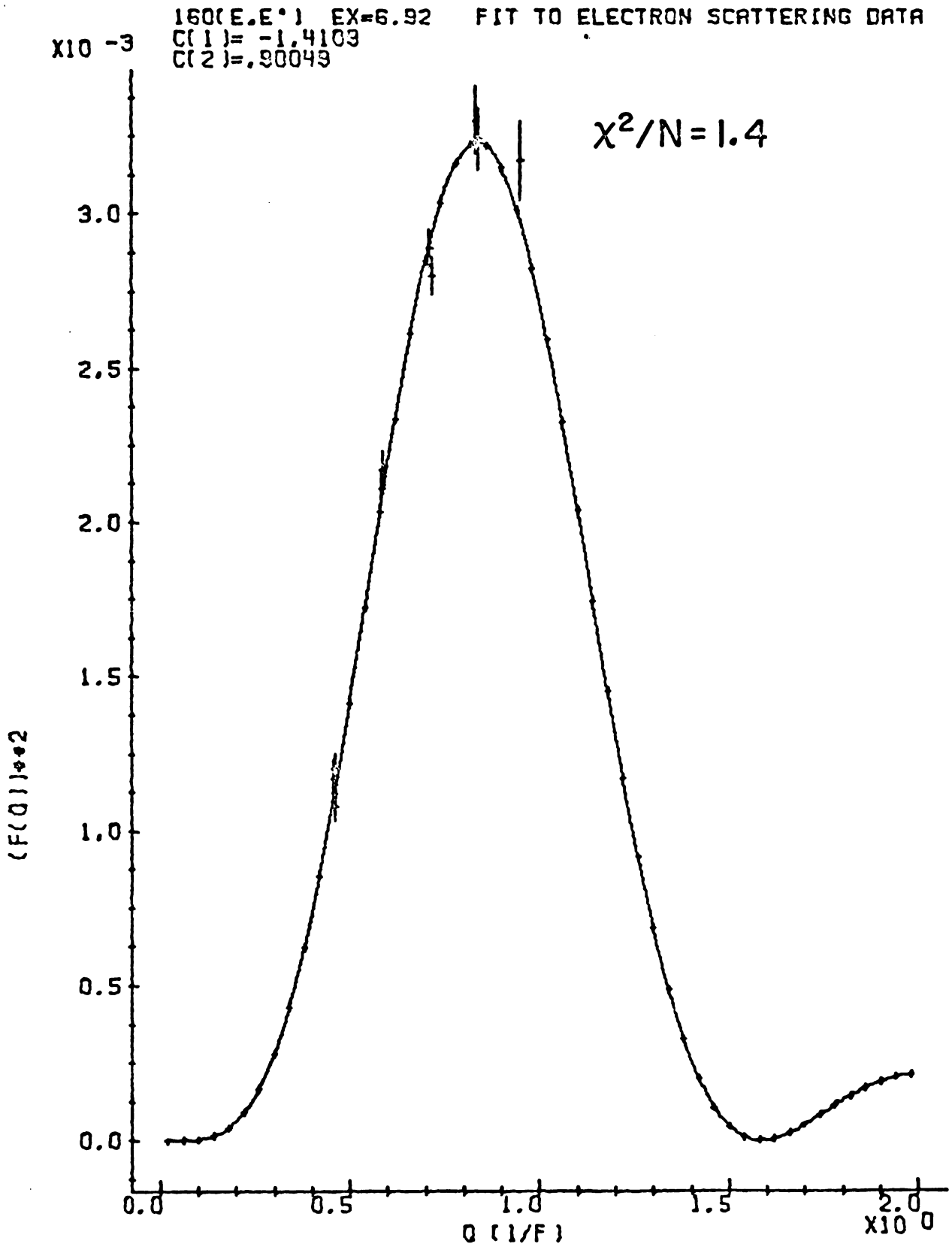

Figure 5.12 Electron scattering form factor using the transition density extracted from the least squares fit.

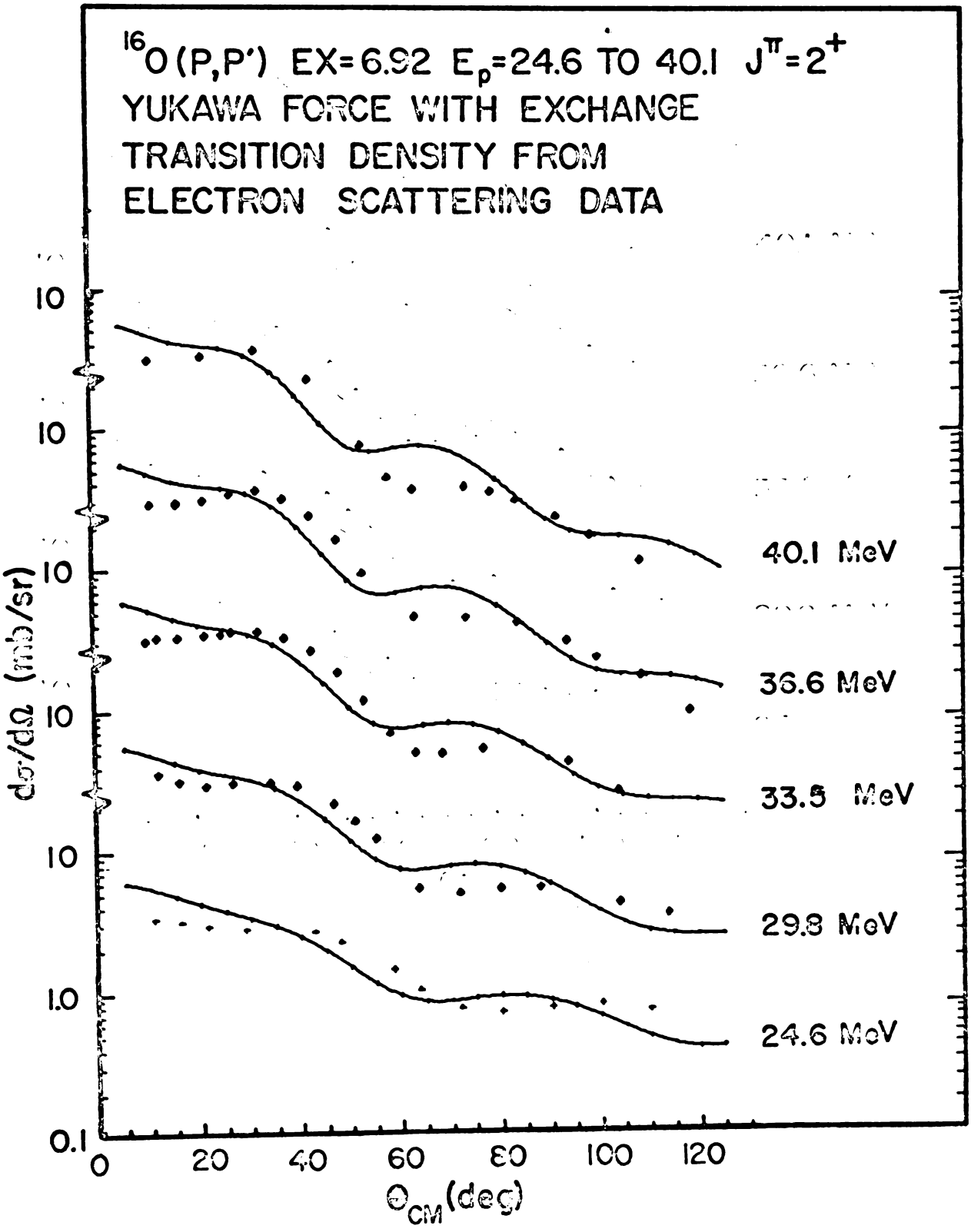

Figure 5.13 DWM calculations using a 1f range Yukawa interaction. The strengths were extracted from the integrated cross sections.

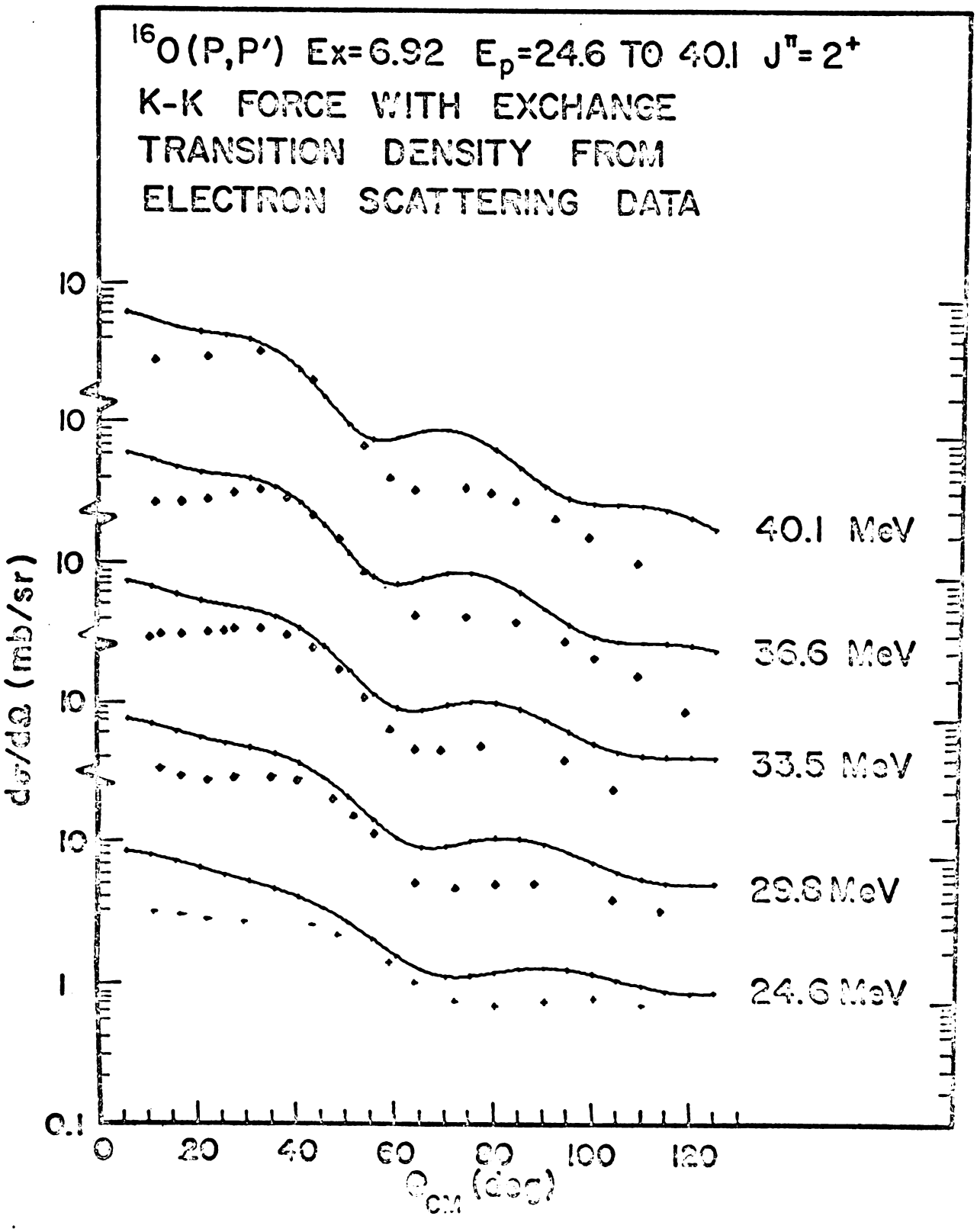

Figure 5.14 DWM calculations using the long range part of the K-K interaction.

Table 5.2

Values of V_{00} in MeV obtained from the microscopic calculations using the Yukawa interaction.

State Energy MeV	24.6 MeV	29.8 MeV	33.6 MeV	36.6 MeV	40.1 MeV
6.05	35.0±2.5	37.0±2.6	32.0±2.2	32.0±1.6	33.0±1.6
6.13	66.0±5.0	59.0±3.0	66.0±3.0	59.0±3.0	59.0±3.0
6.92	48.0±3.0	46.0±2.0	46.0±2.0	47.0±2.0	45.0±2.0
7.12	26.8±1.5	----	21.6±1.1	21.6±1.1	21.6±1.1

Errors listed are the statistical errors added in quadrature with the fluctuations found by using different optical parameters.

sufficiently large range of momentum transfers to adequately define the overall normalization of the transition density.

The calculations using the K-K force with this transition density overestimated the cross section by a factor of 5. The experimental shape, as expected, was not reproduced for momentum transfers larger than those covered by the electron scattering data.

The transition density constructed from the wave functions of Gillet and Vinh Mau did a good job in reproducing the angular distribution out to 80° with the K-K force being slightly better than the Yukawa. Beyond 80° the fits fall off much more rapidly than the data.

The strength of the Yukawa interaction was extracted as before. In this case both the (LSJ) = (101) and (111) terms were summed and thus the strength of V_{00} and V_{10} are included. The contribution of the spin flip term is of the order of 2%, permitting the extracted strength to be identified as V_{00}. The values are listed in Table 5.2.

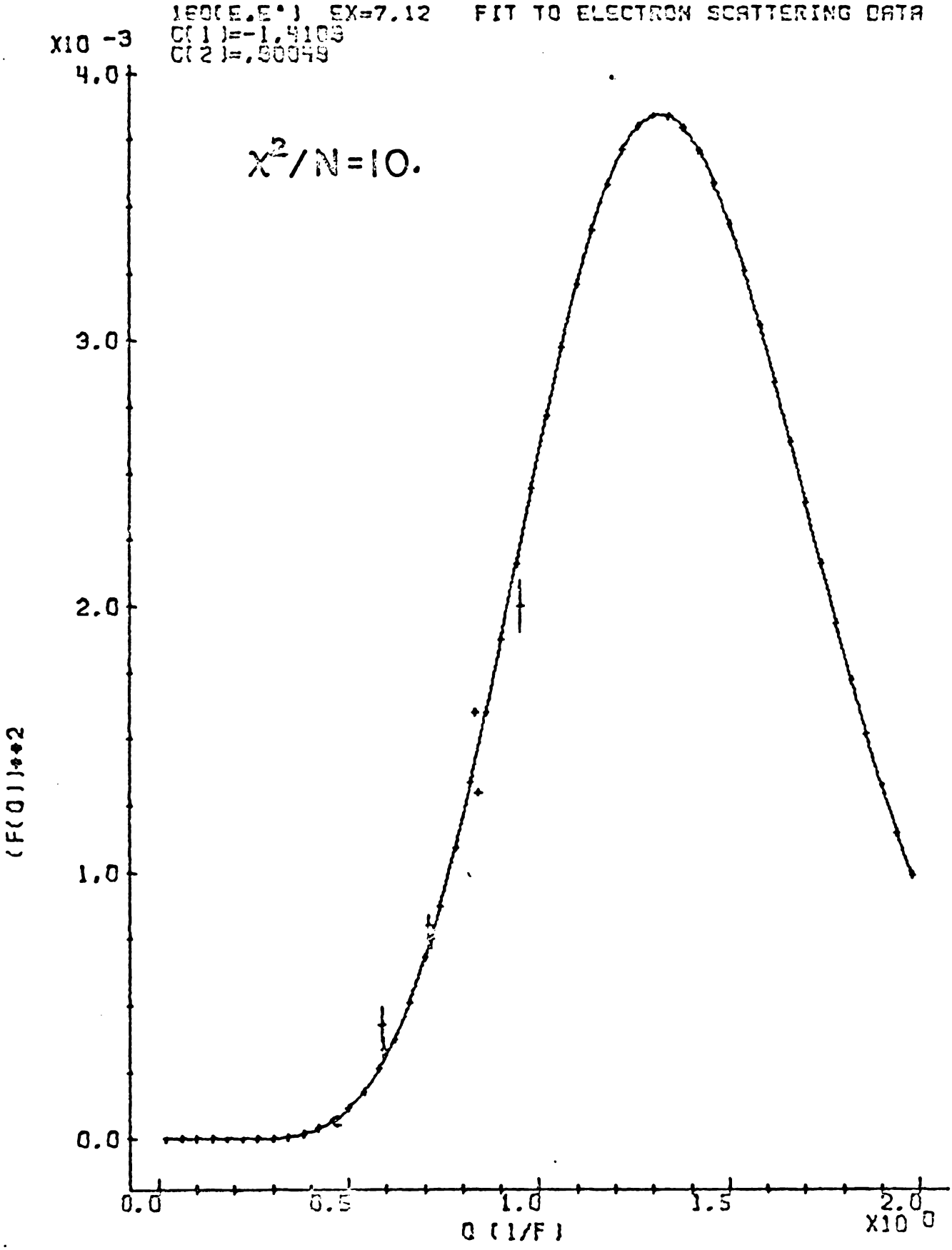

Figure 5.15 Electron scattering form factor calculated from the transition density extracted from the least squares fit.

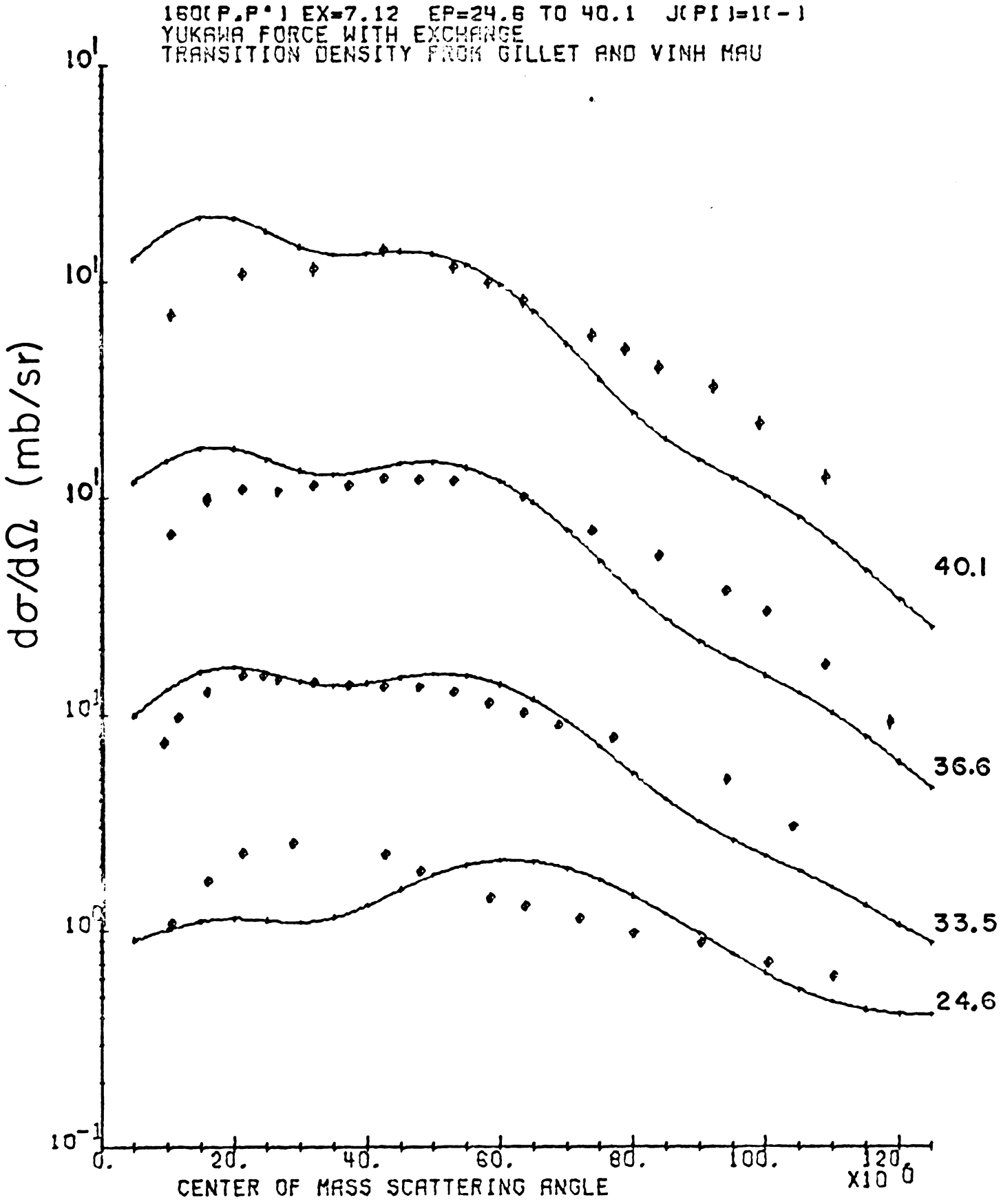

Figure 5.16 DWM calculations using a 1f range Yukawa interaction. The strengths were extracted from the integrated cross sections.

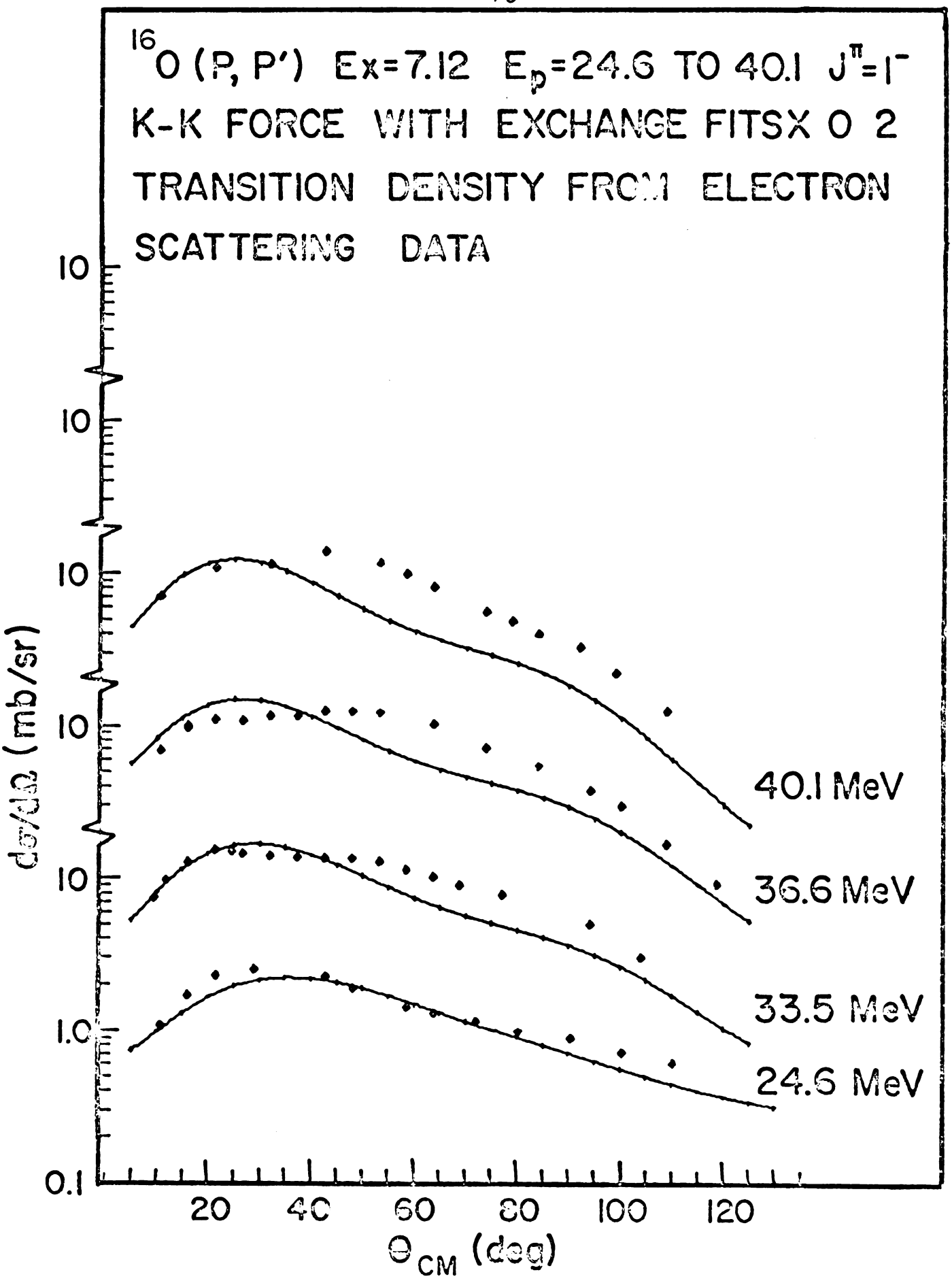

Figure 5.17 DWM calculations using the long range part of the K-K interaction.

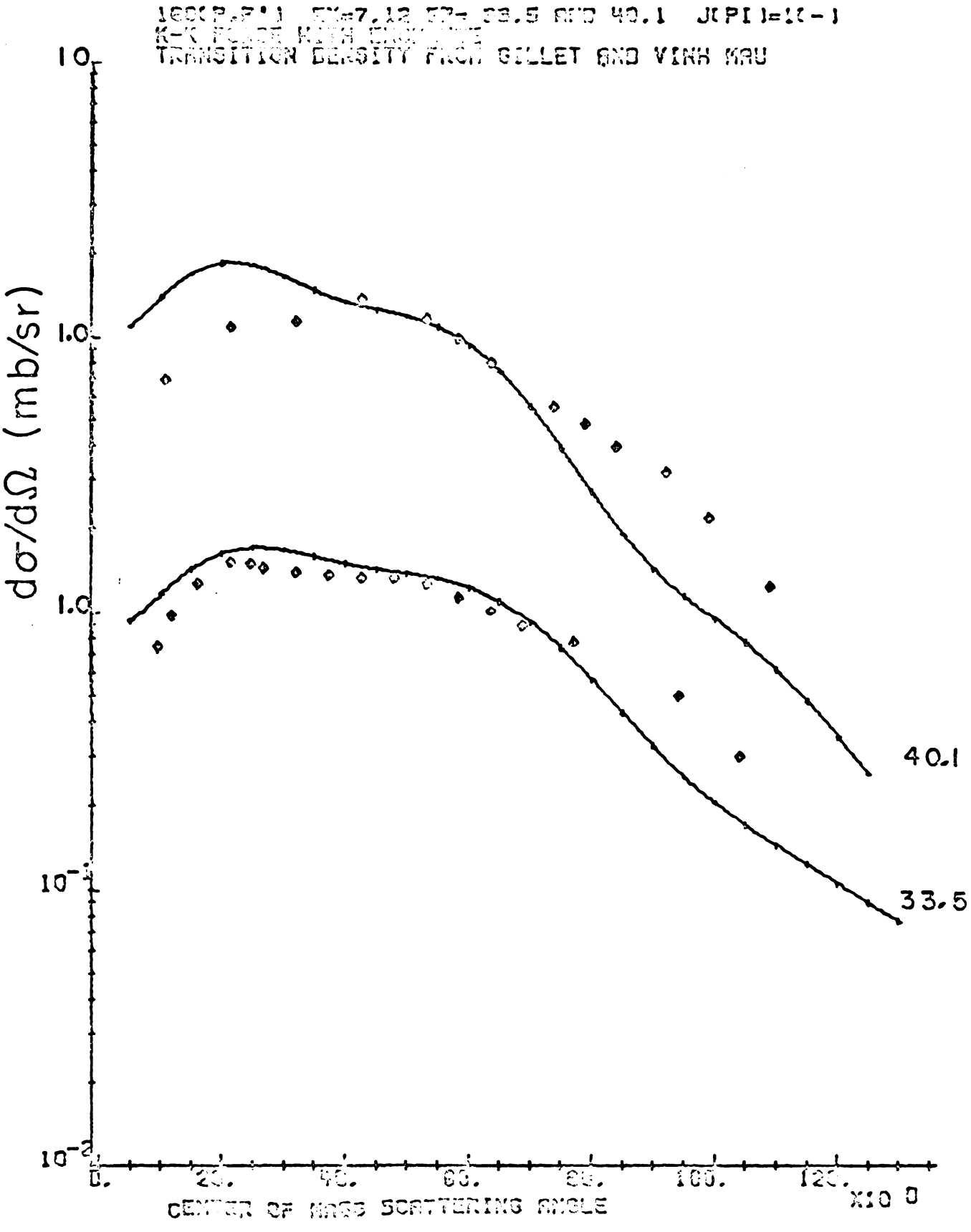

Figure 5.18 DWM calculations using the long range part of the K-K interaction.

6. SUMMARY OF RESULTS AND CONCLUSIONS

6.1 Results

The deformation parameters, β, extracted from the collective model are tabulated in Table 5.1. These values exhibit no energy dependence from 30 to 40 MeV. The large differences at 24.6 MeV are attributed to the difficulty in fitting the elastic scattering for the exit channel. The deformations extracted from the partial transition width data of Alexander and Allen (Al 65) for the 6.13 MeV state to ground state transition and of Evers et al (Ev 68) for the 6.92 and 7.12 MeV states to ground state transitions are compared to the present values. The radius of an equivalent uniform charge distribution (El 61), $R = 1.35\ A^{1/3}$, was used. The agreement is very good for the 6.13 and 6.92 MeV states. The 7.12 MeV state is expected to show poor agreement because the isospin selection rules prohibit electromagnetic dipole transitions in N = Z nuclei (Tr 52). Since the shape of the differential cross section calculated using collective model were in poor agreement with the data, the deformation extracted for this state is of questionable value.

The strengths of the central part of the real Yukawa interaction are tabulated in Table 5.2. The validity of these strengths for the 6.05 and 6.92 MeV states is questionable due to the poor overall fits.

The three interactions used in these calculations provide the same shapes for the angular distributions. The magnitude of the K-K was in good agreement with the data while the K-B was about 30% low. The Yukawa, when normalized to the data was almost indistinguishable from the K-K. On the basis of overall magnitude, this study indicates that the K-K interaction provides the best description. No conclusion, however, can be drawn from the predicted shapes.

6.2 Conclusions

From the analysis of the data presented, it appears that the transition density obtained from electron inelastic scattering provides a description of the nuclear structure adequate for calculating cross sections with realistic nucleon - nucleon interactions. The success in reproducing the general features of the angular distribution of the 3^- with the K-K interaction encourages further development of this approach where good electron scattering data are available. One can now require the electron scattering form factors to predict the proton inelastic scattering, eliminating ambiguities which might otherwise occur.

APPENDIX A

Tabulation of $^{16}O(p,p')\ ^{16}O^*$ Differential Cross Sections

The following pages contain listings of the laboratory and center of mass differential cross sections with the corresponding statistical and total errors for the inelastic scattering of protons by ^{16}O. A discussion of the errors is found in Chapter 2.

16O(P,P')16O

EP= 24.63 EX= 6.05

C.M. ANGLE (DEG)	SIGMA C.M. (MB/SR)	LAB ANGLE (DEG)	SIGMA LAB (MB/SR)	STAT. ERROR (%)	TOTAL ERROR (%)
10.64	3.269E-01	9.90	3.768E-01	2.7	4.0
16.00	3.314E-01	14.90	3.809E-01	2.3	3.6
21.36	2.992E-01	19.90	3.426E-01	2.9	4.3
28.84	3.039E-01	26.90	3.456E-01	2.5	3.8
36.29	2.985E-01	33.90	3.364E-01	3.1	4.5
42.65	2.867E-01	39.90	3.201E-01	3.0	4.3
47.92	2.942E-01	44.90	3.258E-01	2.9	4.2
53.18	2.733E-01	49.90	2.998E-01	2.5	3.8
58.40	2.623E-01	54.90	2.848E-01	2.7	4.0
63.61	2.218E-01	59.90	2.383E-01	3.1	4.4
71.87	1.460E-01	67.90	1.539E-01	3.5	4.7
80.05	9.951E-02	75.90	1.029E-01	3.3	4.5
90.17	1.092E-01	85.90	1.101E-01	3.4	4.7
100.16	1.476E-01	95.90	1.449E-01	2.7	4.0
110.02	1.511E-01	105.90	1.446E-01	3.0	4.2
113.92	1.416E-01	109.90	1.342E-01	3.5	4.8
119.75	1.190E-01	115.90	1.111E-01	3.2	4.5
129.36	6.226E-02	125.90	5.681E-02	4.0	5.2

16O(P,P')16O

EP= 29.81 EX= 6.05

C.M. ANGLE (DEG)	SIGMA C.M. (MB/SR)	LAB ANGLE (DEG)	SIGMA LAB (MB/SR)	STAT. ERROR (%)	TOTAL ERROR (%)
11.69	8.615E-01	10.90	9.893E-01	1.7	2.9
15.97	6.966E-01	14.90	7.981E-01	2.1	3.4
21.32	4.915E-01	19.90	5.611E-01	1.5	2.6
26.66	3.798E-01	24.90	4.315E-01	2.7	3.9
34.11	2.880E-01	31.90	3.245E-01	2.9	4.1
39.41	2.440E-01	36.90	2.730E-01	3.0	4.2
46.80	1.558E-01	43.90	1.724E-01	3.3	4.4
51.00	1.109E-01	47.90	1.218E-01	3.9	5.0
55.19	9.121E-02	51.90	9.944E-02	3.5	4.6
63.51	9.346E-02	59.90	1.002E-01	3.0	4.2
71.77	1.158E-01	67.90	1.219E-01	3.3	4.5
79.95	1.354E-01	75.90	1.399E-01	2.6	3.7
88.05	1.092E-01	83.90	1.106E-01	2.9	4.0
104.01	5.442E-02	99.90	5.292E-02	4.1	5.2
113.82	3.946E-02	109.90	3.743E-02	4.1	5.2

16S(P,P')16O

EP= 33.48 EX= 6.05

C.M. ANGLE (DEG)	SIGMA C.M. (MB/SR)	LAB ANGLE (DEG)	SIGMA LAB (MB/SR)	STAT. ERROR (%)	TOTAL ERROR (%)
9.54	6.518E-01	8.90	7.430E-01	3.1	4.3
11.68	6.012E-01	10.90	6.893E-01	2.1	3.2
15.96	4.654E-01	14.90	5.324E-01	3.0	4.1
21.31	3.876E-01	19.90	4.418E-01	1.9	2.9
24.51	3.338E-01	22.90	3.795E-01	2.6	3.7
28.77	3.273E-01	26.90	3.705E-01	2.1	3.1
28.77	2.963E-01	26.90	3.354E-01	4.1	5.1
31.96	2.984E-01	29.90	3.366E-01	2.8	3.8
37.26	2.539E-01	34.90	2.845E-01	2.7	3.7
42.55	1.950E-01	39.90	2.169E-01	2.3	3.2
47.82	1.405E-01	44.90	1.551E-01	3.0	4.0
53.06	1.057E-01	49.90	1.155E-01	2.9	3.9
58.28	7.557E-02	54.90	8.182E-02	3.4	4.3
63.47	8.241E-02	59.90	8.830E-02	2.8	3.8
68.64	9.235E-02	64.90	9.788E-02	3.1	4.1
76.85	1.006E-01	72.90	1.046E-01	2.8	3.7
84.98	9.455E-02	80.90	9.647E-02	3.1	4.0
94.03	7.434E-02	89.90	7.416E-02	3.6	4.6
103.96	4.543E-02	99.90	4.420E-02	4.1	5.0

16O(P,P')16O

EP= 36.66 EX= 6.05

C.M. ANGLE (DEG)	SIGMA C.M. (MB/SR)	LAB ANGLE (DEG)	SIGMA LAB (MB/SR)	STAT. ERROR (%)	TOTAL ERROR (%)
10.61	4.732E-01	9.90	5.422E-01	1.8	3.1
15.95	3.817E-01	14.90	4.363E-01	2.7	4.0
15.95	3.699E-01	14.90	4.228E-01	2.4	3.6
21.30	3.193E-01	19.90	3.643E-01	2.8	4.1
21.30	3.176E-01	19.90	3.617E-01	2.4	3.7
28.76	2.765E-01	26.90	3.128E-01	3.4	4.6
31.95	2.852E-01	29.90	3.215E-01	2.7	3.9
37.25	2.406E-01	34.90	2.694E-01	2.9	4.2
42.53	1.774E-01	39.90	1.972E-01	3.0	4.2
47.80	1.244E-01	44.90	1.372E-01	3.3	4.5
53.04	9.455E-02	49.90	1.033E-01	3.0	4.1
63.45	6.704E-02	59.90	7.130E-02	3.3	4.4
73.75	6.503E-02	69.90	6.811E-02	3.4	4.5
83.94	6.661E-02	79.90	6.812E-02	3.3	4.3
94.00	6.782E-02	89.90	6.766E-02	3.5	4.5
99.98	6.071E-02	95.90	5.966E-02	3.7	4.8
118.61	1.896E-02	114.90	1.790E-02	5.7	6.7

160(P,P')168

EP= 40.07 EX= 6.05

C.M. ANGLE (DEG)	SIGMA C.M. (MB/SR)	LAB ANGLE (DEG)	SIGMA LAB (MB/SR)	STAT. ERROR (%)	TOTAL ERROR (%)
10.60	5.216E-01	9.90	5.973E-01	1.9	6.5
21.29	3.356E-01	19.90	3.819E-01	2.4	6.9
31.93	2.745E-01	29.90	3.093E-01	2.2	6.6
37.23	2.196E-01	34.90	2.460E-01	2.0	6.3
42.52	1.548E-01	39.90	1.720E-01	3.3	7.7
53.02	7.705E-02	49.90	8.415E-02	3.1	7.3
58.24	6.420E-02	54.90	6.945E-02	3.5	7.6
63.43	6.000E-02	59.90	6.423E-02	3.3	7.4
73.73	5.175E-02	69.90	5.419E-02	3.3	7.4
78.83	4.584E-02	74.90	4.744E-02	4.0	8.2
83.91	4.181E-02	79.90	4.275E-02	3.3	7.4
91.97	4.689E-02	87.90	4.701E-02	3.9	8.0
108.83	2.929E-02	104.90	2.816E-02	5.4	9.5

160(P,P')168

EP= 24.63 EX= 6.13

C.M. ANGLE (DEG)	SIGMA C.M. (MB/SR)	LAB ANGLE (DEG)	SIGMA LAB (MB/SR)	STAT. ERROR (%)	TOTAL ERROR (%)
10.64	7.186E+00	9.90	8.285E+00	0.5	2.1
16.00	7.528E+00	14.90	8.657E+00	0.5	2.1
21.36	8.130E+00	19.90	9.313E+00	0.5	2.2
28.84	8.861E+00	26.90	1.008E+01	0.4	2.1
36.29	9.301E+00	33.90	1.049E+01	0.5	2.3
42.65	9.876E+00	39.90	1.103E+01	0.5	2.2
47.93	9.622E+00	44.90	1.066E+01	0.5	2.2
53.18	9.215E+00	49.90	1.011E+01	0.4	2.0
58.41	8.449E+00	54.90	9.176E+00	0.5	2.1
63.61	7.338E+00	59.90	7.883E+00	0.5	2.2
71.88	5.782E+00	67.90	6.098E+00	0.5	2.1
80.06	4.250E+00	75.90	4.395E+00	0.5	1.9
90.18	2.970E+00	85.90	2.993E+00	0.7	2.1
100.17	2.274E+00	95.90	2.232E+00	0.7	2.1
110.03	1.893E+00	105.90	1.811E+00	0.8	2.2
113.93	1.704E+00	109.90	1.614E+00	1.0	2.4
119.76	1.628E+00	115.90	1.519E+00	0.9	2.2
129.37	8.903E-01	125.90	8.122E-01	1.0	2.4

160(P,P')160

EP= 29.81 EX= 6.13

C.M. ANGLE (DEG)	SIGMA C.M. (MB/SR)	LAB ANGLE (DEG)	SIGMA LAB (MB/SR)	STAT. ERROR (%)	TOTAL ERROR (%)
11.69	5.597E+00	10.90	6.429E+00	0.7	2.1
15.98	5.889E+00	14.90	6.749E+00	0.7	2.2
21.32	6.447E+00	19.90	7.361E+00	0.4	1.7
26.66	7.373E+00	24.90	8.379E+00	0.6	2.1
34.11	8.382E+00	31.90	9.447E+00	0.5	2.0
39.41	9.065E+00	36.90	1.015E+01	0.5	1.9
46.80	9.254E+00	43.90	1.024E+01	0.4	1.8
51.01	8.771E+00	47.90	9.638E+00	0.4	1.8
55.19	8.157E+00	51.90	8.894E+00	0.4	1.7
63.52	5.880E+00	59.90	6.307E+00	0.4	1.7
71.78	3.836E+00	67.90	4.040E+00	0.6	1.9
79.96	2.431E+00	75.90	2.512E+00	0.6	1.8
88.06	1.624E+00	83.90	1.645E+00	0.7	2.0
104.02	1.001E+00	99.90	9.735E-01	0.9	2.1
113.83	7.954E-01	109.90	7.545E-01	0.9	2.1

168(P,P')168

EP= 33.48 EX= 6.13

C.M. ANGLE (DEG)	SIGMA C.M. (MB/SR)	LAB ANGLE (DEG)	SIGMA LAB (MB/SR)	STAT. ERROR (%)	TOTAL ERROR (%)
9.54	4.767E+00	8.90	5.472E+00	1.2	2.7
11.68	5.242E+00	10.90	6.011E+00	0.7	2.0
15.96	6.026E+00	14.90	6.895E+00	0.8	2.3
21.31	6.984E+00	19.90	7.962E+00	0.4	1.7
24.51	7.488E+00	22.90	8.515E+00	0.6	1.9
28.77	8.396E+00	26.90	9.507E+00	0.4	1.7
28.77	7.978E+00	26.90	9.034E+00	0.8	2.3
31.96	8.465E+00	29.90	9.552E+00	0.5	1.9
37.27	9.101E+00	34.90	1.020E+01	0.4	1.7
42.55	9.534E+00	39.90	1.061E+01	0.3	1.5
47.82	9.157E+00	44.90	1.010E+01	0.4	1.6
53.06	8.268E+00	49.90	9.042E+00	0.3	1.5
58.28	6.950E+00	54.90	7.526E+00	0.3	1.5
63.48	5.371E+00	59.90	5.755E+00	0.3	1.5
68.65	4.074E+00	64.90	4.318E+00	0.5	1.6
76.85	2.500E+00	72.90	2.601E+00	0.6	1.6
84.98	1.617E+00	80.90	1.650E+00	0.7	1.8
94.03	1.074E+00	89.90	1.071E+00	1.0	2.0
103.97	7.025E-01	99.90	6.833E-01	1.0	2.0

169(P,P')169

EP= 36.66 EX= 6.13

C.M. ANGLE (DEG)	SIGMA C.M. (MB/SR)	LAB ANGLE (DEG)	SIGMA LAB (MB/SR)	STAT. ERROR (%)	TOTAL ERROR (%)
10.61	3.811E+00	9.90	4.368E+00	0.6	2.2
15.96	4.810E+00	14.90	5.499E+00	0.7	2.5
15.96	4.759E+00	14.90	5.441E+00	0.6	2.3
21.30	5.839E+00	19.90	6.651E+00	0.6	2.4
21.30	5.939E+00	19.90	6.765E+00	0.5	2.2
28.76	7.335E+00	26.90	8.299E+00	0.6	2.5
31.95	7.733E+00	29.90	8.718E+00	0.5	2.3
37.25	8.877E+00	34.90	9.943E+00	0.5	2.2
42.53	9.142E+00	39.90	1.016E+01	0.4	2.1
47.80	8.793E+00	44.90	9.701E+00	0.4	2.0
53.04	7.553E+00	49.90	8.254E+00	0.3	1.8
63.45	4.579E+00	59.90	4.905E+00	0.4	1.8
73.76	2.556E+00	69.90	2.677E+00	0.5	1.8
83.94	1.451E+00	79.90	1.484E+00	0.7	1.9
94.00	8.980E-01	89.90	8.958E-01	0.9	2.1
99.98	6.864E-01	95.90	6.745E-01	1.0	2.2
118.62	2.662E-01	114.90	2.499E-01	1.4	2.5

169(P,P')168

EP= 40.07 EX= 6.13

C.M. ANGLE (DEG)	SIGMA C.M. (MB/SR)	LAB ANGLE (DEG)	SIGMA LAB (MB/SR)	STAT. ERROR (%)	TOTAL ERROR (%)
10.60	4.234E+00	9.90	4.849E+00	0.6	5.8
21.29	6.013E+00	19.90	6.844E+00	0.6	5.8
31.94	7.854E+00	29.90	8.849E+00	0.4	5.4
37.24	7.984E+00	34.90	8.937E+00	0.3	5.2
42.52	8.808E+00	39.90	9.788E+00	0.4	5.6
53.02	6.742E+00	49.90	7.364E+00	0.3	5.1
58.24	4.981E+00	54.90	5.388E+00	0.4	5.1
63.43	3.823E+00	59.90	4.093E+00	0.4	5.0
73.73	1.971E+00	69.90	2.064E+00	0.5	5.0
78.84	1.423E+00	74.90	1.473E+00	0.7	5.2
83.92	1.099E+00	79.90	1.123E+00	0.6	5.0
91.98	8.276E-01	87.90	8.297E-01	0.9	5.3
108.84	2.426E-01	104.90	2.332E-01	1.9	6.1

16O(P,P')16O

EP= 24.63 EX= 6.92

C.M. ANGLE (DEG)	SIGMA C.M. (MB/SR)	LAB ANGLE (DEG)	SIGMA LAB (MB/SR)	STAT. ERROR (%)	TOTAL ERROR (%)
10.66	3.401E+00	9.90	3.934E+00	0.9	2.5
16.03	3.229E+00	14.90	3.725E+00	0.6	2.1
21.40	3.002E+00	19.90	3.450E+00	1.0	2.7
28.89	2.831E+00	26.90	3.230E+00	0.9	2.4
42.72	2.696E+00	39.90	3.019E+00	0.9	2.5
48.00	2.272E+00	44.90	2.522E+00	1.0	2.5
58.50	1.442E+00	54.90	1.569E+00	1.6	3.2
63.70	1.034E+00	59.90	1.113E+00	1.5	2.9
71.97	7.508E-01	67.90	7.928E-01	2.0	3.5
80.16	6.907E-01	75.90	7.147E-01	1.9	3.3
90.28	7.451E-01	85.90	7.510E-01	1.7	3.0
100.27	7.830E-01	95.90	7.684E-01	2.1	3.5
110.12	6.998E-01	105.90	6.688E-01	2.0	3.4

16O(P,P')16O

EP= 29.81 EX= 6.92

C.M. ANGLE (DEG)	SIGMA C.M. (MB/SR)	LAB ANGLE (DEG)	SIGMA LAB (MB/SR)	STAT. ERROR (%)	TOTAL ERROR (%)
11.71	3.587E+00	10.90	4.129E+00	0.8	2.2
16.00	3.164E+00	14.90	3.635E+00	1.0	2.4
21.35	2.948E+00	19.90	3.374E+00	0.6	1.9
26.69	3.083E+00	24.90	3.512E+00	0.9	2.3
34.15	3.071E+00	31.90	3.469E+00	0.9	2.2
39.46	2.925E+00	36.90	3.280E+00	0.9	2.2
46.85	2.149E+00	43.90	2.382E+00	0.9	2.1
51.06	1.631E+00	47.90	1.795E+00	1.0	2.3
55.25	1.214E+00	51.90	1.326E+00	0.9	2.2
63.59	5.354E-01	59.90	5.749E-01	1.3	2.4
71.85	4.915E-01	67.90	5.182E-01	1.6	2.8
80.03	5.209E-01	75.90	5.385E-01	1.3	2.5
88.13	5.286E-01	83.90	5.354E-01	1.3	2.5
104.09	4.057E-01	99.90	3.943E-01	1.5	2.6
113.90	3.382E-01	109.90	3.205E-01	1.4	2.5

169(P,P')169

EP= 33.48 EX= 6.92

C.M. ANGLE (DEG)	SIGMA C.M. (MB/SR)	LAB ANGLE (DEG)	SIGMA LAB (MB/SR)	STAT. ERROR (%)	TOTAL ERROR (%)
9.55	3.135E+00	8.90	3.606E+00	1.4	2.9
11.69	3.334E+00	10.90	3.832E+00	0.9	2.1
15.98	3.329E+00	14.90	3.817E+00	1.1	2.5
21.33	3.441E+00	19.90	3.930E+00	0.6	1.8
24.53	3.525E+00	22.90	4.016E+00	0.8	2.0
26.67	3.653E+00	24.90	4.159E+00	1.3	2.7
31.99	3.614E+00	29.90	4.085E+00	0.8	2.0
37.30	3.281E+00	34.90	3.685E+00	0.7	1.9
42.59	2.626E+00	39.90	2.927E+00	0.6	1.7
47.87	1.832E+00	44.90	2.024E+00	0.8	1.9
53.11	1.160E+00	49.90	1.270E+00	0.9	1.9
58.34	6.823E-01	54.90	7.397E-01	1.1	2.1
63.53	4.923E-01	59.90	5.281E-01	1.2	2.1
68.70	4.829E-01	64.90	5.123E-01	1.4	2.4
76.91	5.196E-01	72.90	5.409E-01	1.2	2.2
94.10	4.115E-01	89.90	4.104E-01	1.5	2.5
104.03	2.527E-01	99.90	2.457E-01	1.7	2.7

169(P,P')169

EP= 36.66 EX= 6.92

C.M. ANGLE (DEG)	SIGMA C.M. (MB/SR)	LAB ANGLE (DEG)	SIGMA LAB (MB/SR)	STAT. ERROR (%)	TOTAL ERROR (%)
10.62	2.967E+00	9.90	3.407E+00	0.9	2.5
15.97	3.027E+00	14.90	3.466E+00	0.9	2.6
15.97	2.955E+00	14.90	3.384E+00	0.9	2.6
21.32	3.124E+00	19.90	3.564E+00	0.9	2.6
26.65	3.479E+00	24.90	3.951E+00	0.9	2.7
31.98	3.633E+00	29.90	4.103E+00	0.8	2.5
37.28	3.172E+00	34.90	3.558E+00	0.9	2.6
42.57	2.375E+00	39.90	2.645E+00	1.0	2.6
47.84	1.610E+00	44.90	1.778E+00	1.3	2.9
53.08	9.304E-01	49.90	1.018E+00	1.5	2.9
63.50	4.537E-01	59.90	4.864E-01	2.2	3.4
73.31	4.392E-01	69.90	4.603E-01	2.5	3.9
84.00	4.020E-01	79.90	4.112E-01	2.5	3.8
94.06	2.925E-01	89.90	2.917E-01	2.6	3.8
100.04	2.227E-01	95.90	2.188E-01	3.4	4.6
108.92	1.648E-01	104.90	1.583E-01	3.1	4.3
118.67	9.124E-02	114.90	8.555E-02	4.8	5.9

169(P,P')169

EP= 40.07 EX= 6.92

C.M. ANGLE (DEG)	SIGMA C.M. (MB/SR)	LAB ANGLE (DEG)	SIGMA LAB (MB/SR)	STAT. ERROR (%)	TOTAL ERROR (%)
10.61	3.150E+00	9.90	3.614E+00	0.7	5.6
21.31	3.326E+00	19.90	3.792E+00	0.7	5.7
31.96	3.601E+00	29.90	4.063E+00	0.7	5.7
42.55	2.239E+00	39.90	2.491E+00	0.8	5.7
53.06	7.491E-01	49.90	8.191E-01	1.5	6.2
58.28	4.410E-01	54.90	4.775E-01	1.7	6.2
63.47	3.584E-01	59.90	3.841E-01	2.2	6.7
73.78	3.750E-01	69.90	3.929E-01	1.9	6.4
78.89	3.398E-01	74.90	3.518E-01	2.3	6.8
83.97	2.976E-01	79.90	3.044E-01	2.2	6.6
92.03	2.235E-01	87.90	2.241E-01	3.0	7.3
99.01	1.635E-01	94.90	1.611E-01	2.9	7.2
108.39	1.064E-01	104.90	1.022E-01	3.6	7.8

169(P,P')169

EP= 24.63 EX= 7.12

C.M. ANGLE (DEG)	SIGMA C.M. (MB/SR)	LAB ANGLE (DEG)	SIGMA LAB (MB/SR)	STAT. ERROR (%)	TOTAL ERROR (%)
10.66	1.080E+00	9.90	1.251E+00	1.7	3.2
16.04	1.707E+00	14.90	1.971E+00	0.9	2.3
21.40	2.286E+00	19.90	2.629E+00	1.2	2.8
28.90	2.528E+00	26.90	2.887E+00	0.9	2.5
42.74	2.255E+00	39.90	2.527E+00	1.0	2.5
48.02	1.883E+00	44.90	2.091E+00	1.1	2.5
58.52	1.426E+00	54.90	1.552E+00	1.6	3.2
63.72	1.293E+00	59.90	1.392E+00	1.3	2.8
72.00	1.136E+00	67.90	1.200E+00	1.7	3.1
80.19	9.661E-01	75.90	1.000E+00	1.6	3.1
90.31	8.712E-01	85.90	8.782E-01	1.5	2.9
100.30	7.042E-01	95.90	6.909E-01	2.2	3.6
110.15	6.058E-01	105.90	5.788E-01	2.2	3.6

169(P,P')169

EP= 33.48 EX= 7.12

C.M. ANGLE (DEG)	SIGMA C.M. (MB/SR)	LAB ANGLE (DEG)	SIGMA LAB (MB/SR)	STAT. ERROR (%)	TOTAL ERROR (%)
9.55	7.432E-01	8.90	8.552E-01	2.9	4.1
11.70	9.719E-01	10.90	1.117E+00	1.6	2.7
15.98	1.276E+00	14.90	1.464E+00	1.8	3.0
21.34	1.524E+00	19.90	1.742E+00	0.9	2.0
24.54	1.512E+00	22.90	1.723E+00	1.2	2.4
26.68	1.458E+00	24.90	1.659E+00	2.0	3.3
32.00	1.407E+00	29.90	1.592E+00	1.3	2.4
37.31	1.374E+00	34.90	1.543E+00	1.2	2.3
42.61	1.345E+00	39.90	1.500E+00	0.9	1.9
47.88	1.341E+00	44.90	1.483E+00	1.0	2.0
53.13	1.277E+00	49.90	1.399E+00	0.8	1.9
58.35	1.135E+00	54.90	1.231E+00	0.9	1.9
63.55	1.012E+00	59.90	1.086E+00	0.8	1.8
68.72	8.945E-01	64.90	9.491E-01	1.0	2.0
76.93	7.781E-01	72.90	8.101E-01	1.0	2.0
94.11	4.993E-01	89.90	4.980E-01	1.4	2.4
104.05	3.016E-01	99.90	2.932E-01	1.6	2.5

169(P,P')169

EP= 36.66 EX= 7.12

C.M. ANGLE (DEG)	SIGMA C.M. (MB/SR)	LAB ANGLE (DEG)	SIGMA LAB (MB/SR)	STAT. ERROR (%)	TOTAL ERROR (%)
10.62	6.858E-01	9.90	7.878E-01	1.9	3.3
15.97	1.006E+00	14.90	1.152E+00	1.6	3.1
15.97	9.743E-01	14.90	1.116E+00	1.6	3.0
21.32	1.100E+00	19.90	1.255E+00	1.5	3.0
26.66	1.081E+00	24.90	1.229E+00	1.7	3.2
31.98	1.153E+00	29.90	1.303E+00	1.5	3.0
37.29	1.157E+00	34.90	1.298E+00	1.6	3.1
42.58	1.252E+00	39.90	1.394E+00	1.4	2.9
47.85	1.234E+00	44.90	1.363E+00	1.5	3.0
53.10	1.211E+00	49.90	1.326E+00	1.3	2.7
63.51	1.019E+00	59.90	1.093E+00	1.4	2.8
73.82	7.115E-01	69.90	7.458E-01	2.0	3.4
84.01	5.417E-01	79.90	5.541E-01	2.2	3.5
94.07	3.729E-01	89.90	3.719E-01	2.3	3.5
100.05	2.967E-01	95.90	2.915E-01	2.9	4.2
108.93	1.685E-01	104.90	1.618E-01	3.3	4.4
118.68	9.142E-02	114.90	8.570E-02	5.5	6.5

169(P,P')169

EP= 40.07 EX= 7.12

C.M. ANGLE (DEG)	SIGMA C.M. (MB/SR)	LAB ANGLE (DEG)	SIGMA LAB (MB/SR)	STAT. ERROR (%)	TOTAL ERROR (%)
10.61	7.063E-01	9.90	8.106E-01	1.5	6.1
21.31	1.090E+00	19.90	1.243E+00	1.2	6.0
31.97	1.142E+00	29.90	1.289E+00	1.3	6.0
42.56	1.390E+00	39.90	1.547E+00	1.0	5.8
53.07	1.173E+00	49.90	1.283E+00	1.2	6.0
58.29	9.960E-01	54.90	1.079E+00	1.1	5.7
63.49	8.118E-01	59.90	8.700E-01	1.5	6.1
73.79	5.613E-01	69.90	5.881E-01	1.6	6.1
78.90	4.846E-01	74.90	5.018E-01	1.9	6.5
83.98	4.007E-01	79.90	4.099E-01	1.9	6.3
92.04	3.248E-01	87.90	3.256E-01	2.4	6.9
99.02	2.204E-01	94.90	2.171E-01	2.6	6.9
108.90	1.251E-01	104.90	1.202E-01	3.2	7.5

APPENDIX B

In this appendix a description of the nine different data acquisition routines available in TOOTSIE will be given.

The datum consists of two or three 16-bit numbers in coincidence, labeled X, Y, and Z, presented to the XDS Sigma 7 computer through the general purpose interface. Each event causes an interrupt to occur. The interrupt routine must completely process one event before the computer will accept another. The ADCs, however, can begin processing a second event as soon as the interrupt routine reads and resets them, providing considerable overlap in conversion and processing time.

Each interrupt routine operates in two modes. In SETUP mode data are stored in a two dimensional matrix, allowing nonlinear bands to be selected with polynomial fits defining the lower and upper boundaries of each band. In RUN mode events are compared against tables generated from the fits which define the bands. A spectrum of counts verses channel number is accumulated for each band in the tables.

The interrupt routines can be divided into two classes determined by the identification criterion required in RUN mode. The first class of routines requires only that the function F(X,Y) fall within one of the bands defined in SETUP mode. The second class of routines require each event

to satisfy two identification criteria. The function F(X,Y) must lie within a band and G(X,Z) must lie within a band corresponding to the band in which F(X,Y) was found.

Four of the five routines in the first class differ only by the calculation F(X,Y), performed on the data before it is stored in the matrix and before identification. These routines provide options such as simultaneous magnetic tape recording of the raw data and eight way fan out with routing bits.

The routines are:

1) EDELTAE:

   For this routine F(X,Y) = Y, and the matrix elements in SETUP mode are DATA(F(X,Y),X). In RUN mode F(X,Y) is compared against the tables of bands to identify an event and spectra of counts versus X are accumulated. One use of this routine is in two counter telescope experiments in which energy lost in a thin ΔE counter is plotted as a function total energy.

2) E*DELTAE

   This routine differs from EDELTAE only by the definition F(X,Y) = X*Y. This routine is primarily intended for two counter telescope experiments. The product of ΔE and total energy plotted as a function of total energy is a straight band. This simplifies the process of drawing bands.

3) E*T**2

This routine also differs from the EDELTAE routine by the definition of F(X,Y) = X*(Y-Y_0)**2/N + Y_1, where Y_0, N, and Y_1 are input from the teletype. This routine is used in charged particle time of flight experiments. The function F(X,Y) is directly proportional to the mass of the detected particles.

4) XE/E

This routine defines F(X,Y) = N*X/Y, where N is a normalization factor determined by the number of channels in each spectrum. In SETUP mode the matrix elements are DATA(Y,F(X,Y)). In RUN mode Y is checked against the tables of bands and spectra of counts verses F(X,Y) are acquired. This routine, as discussed in the text, is used with position sensitive detectors in the spectrograph.

5) LIGHT

This routine requires three parameters. In SETUP mode the matrix elements are labeled DATA(F(X,Y),X), where F(X,Y) = Y, and the Z datum is ignored. In Run mode F(X,Y) is checked against the tables and spectra of counts versus Z are generated. This routine

is used for neutron time of flight data. The X and Y signals are used to separate neutrons from gamma rays while the Z signal is flight time.

The four routines in the second classification differ only in the calculations performed on the data before being stored. These routines also provide options such as simultaneous magnetic tape recording of the raw data.

The operation of these routines in SETUP mode is somewhat more complicated than in the previous routines. Two independent sets of bands, corresponding to F(X,Y) and G(X,Z) must be defined and a correspondence between them established. To define the bands for classification of events, the matrix DATA(F(X,Y),X) is stored, ignoring the Z datum. A teletpye command switches over to storing elements DATA(G(X,Z),X), disregarding Y datum. Lists of bands to check in the tables for G(X,Z) for each band in the F(X,Y) tables are entered via the teletype.

In RUN mode the function F(X,Y) is checked against the table of bands until a match if found. The bands in the G(X,Z) tables which correspond to the appropriate band are then checked. If a match is found, the appropriate channel in the counts versus X spectrum corresponding to the band in the G(X,Z) tables is incremented.

The functions F and G for the four routines are given by:

1) EDELTAE&EDELTAE:

F(X,Y) = Y; G(X,Z) = Z

This routine has been used in life time measurements when more than one decay channel was open. A two counter telescope detector arrangement was used to identify the decay product and a time signal was used to determine when the event occurred.

2) E*DELTAE&E*DELTAE:

F(X,Y) = Y; G(X,Z) = X*Z

This routine has been used in three counter telescope, redundant identification experiments. An event must have the correct ΔE in both transmission counters. This reduces the number of accidental events and thus increases the peak to valley ratio.

3) E*T**2&EDELTAE:

F(X,Y) = X*(Y-Y_0)**2/N + Y_1

Y_0, N, Y_1 are input on the teletype.

G(X,Z) = Z

This routine is also used for redundant identification. In this case, an event must have the correct mass and Z^2/m to be counted.

4) E*T**2&E*DELTAE:

$F(X,Y) = X*(Y-Y_0)**2/N + Y_1$

$G(X,Z) = Z$

This routine is also intended for redundant identification using flight time and ΔE information.

A more complete description of these routines and the operation of TOOTSIE is given in Michigan State University Cyclotron Computer Report Number 13.

LIST OF REFERENCES

Al 65 T.K. Alexander and K.W. Allen, Canadian Journal of Physics 43 (1965) 1563

Au 61 N. Austern, Fast Neutron Physics, Vol II, ed. by J.B. Marion and J.L. Fowler (Interscience, New York, 1961)

Au 70 S.A. Austin, P.J. Locard, S.N. Bunker, J.M. Cameron, J.R. Richardson, J.W. Verba, W.T.H. van Oers, (to be published)

Ba 70 D.L. Bayer, Michigan State University Cyclotron Laboratory, Sigma 7 Program description 13

Ba 70 D.L. Bayer and R. Au, Michigan State University Cyclotron Laboratory, Sigma 7 Program description 56

Ba 62 R.H. Bassel et al, The Distorted-Wave Theory of Direct Nuclear Reactions, I: "Zero-Range" Formalism Without Spin Orbit Coupling, and the Code Sally, ORNL-3240

Be 70 J.C. Bergstrom, W. Bertozzi, S. Kowalski, X.K. Maruyama, J.W. Lightbody, S.P. Fevozinsky, and S. Penner, Phys. Rev. Letters 24, (1970) 152

Bl 59 J.S. Blair, Phys. Rev. 115, (1959) 928

Bl 66 H.G. Blosser and A.I. Galonsky, IEEE Trans. on Nuclear Science, NS-B 4 (1966) 466

Bo 64 J. Borysowicz and R.K. Sheline, Phys. Lett. 12 (1964) 219

Br 66 G.E. Brown and A.M. Green, Nuc. Phys. 75 (1966) 401

Bu 57 S.T. Butler, Phys. Rev. 106 (1957) 272

Ca 67 J.M. Cameron, PhD Thesis, University of California (1967)

Ca 64 E.B. Carter, G.E. Mitchell, and R.H. Davis, Phys. Rev. 133 (1964) B1421

Cr 66 H. Crannel, Phys. Rev. 148 (1966) 1107

Cr 65 G.M. Crawley, PhD Thesis, Princeton University, Technical Report PUC - 937 - 1965 - 164, (1965)

Da 68 Guide to the Selection and Use of Position Sensitive Detectors, Nuclear Diodes, ed. by W.W. Daehnick (1969)

Da 58 A.S. Davydov and G.F. Filippov, Nuclear Phys. 8 (1958) 237

El 58 J.P. Elliot, Proc. Roy. Soc. A245 (1958) 128

El 61 L.R.B. Elton, Nuclear Sizes, (Oxford University Press, 1961)

En 67 H.A. Enge and J.E. Spencer, Split Pole Magnetic Spectrograph for Precision Nuclear Spectroscopy, Nuclear Inst. and Methods 49 (1967) 181

Ev 68 D. Evers, G. Flugge, J. Morgenstern, T.W. Retz-Schmidt and S.J. Skorka, Phys. Lett. 27B, (1968) 423

Gi 64 V. Gillet and N. Vinh Mau, Nucl. Phys. 54 (1964) 321

Gr 69 C.R. Gruhn, B.M. Preedom and K. Thompson, Phys. Rev. Lett. 23 (1969) 1175

Ha 62 T. Hamada and I.D. Johnston, Nucl. Phys. 34 (1962) 382

Ka 64 A. Kallio and K. Kolltveit, Nucl. Phys. 53 (1964) 87

Ko 68 J.O. Kopf and P.J. Plauger, American Federation of Information Processing Societies 33 (1968) 1033

Ku 66 T.T.S. Kuo and G.E. Brown, Nucl. Phys. 85 (1966) 40

Ma 67 G.H. Mackenzie, E. Kashy, M.M. Gordon, and H.G. Blosser, IEEE Trans. On Nucl. Sci. NS-14 3 (1967) 450

Ma 68 D.R. Maxson, R.K. Jolly and D.C. Knox, Nucl. Instr. Methods 62 (1968) 276

Na 63 D.M. Brink and G.F. Nash, Nucl. Phys. 40 (1963) 608

Pe 70 F.L. Petrovich, PhD Thesis, Michigan State University (to be published) (1970)

Pr 62 M.A. Preston, "Physics of the Nucleus", Addison-Wesley, Reading, Mass. (1962) 299

Sa 64 G.R. Satchler, Nucl. Phys. 55 (1964) 1

Sa 66 G.R. Satchler, Nucl. Phys. 77 (1966) 481

Sn 68 J.L. Snelgrove, PhD Thesis, Michigan State University (unpublished), (1968)

To 61 W. Tobocman, Theory of Direct Nuclear Reactions, (Oxford University Press, 1961)

Tr 70 G.F. Trentelman, Private Communication

Tr 52 L.E.H. Trainor, Phy. Rev. 85 (1952) 962